

Theoretical modeling and computer simulations of protein adsorption onto soft polymeric layers

D i s s e r t a t i o n

zur Erlangung des akademischen Grades

d o c t o r r e r u m n a t u r a l i u m

(Dr. rer. nat.)

im Fach Physik

eingereicht an der

Mathematisch-Naturwissenschaftlichen Fakultät
der Humboldt-Universität zu Berlin

von

Herr Dipl.-Phys. Cemil Yigit

Präsident der Humboldt-Universität zu Berlin
Prof. Dr. Jan-Hendrik Olbertz

Dekan der Mathematisch-Naturwissenschaftlichen Fakultät
Prof. Dr. Elmar Kulke

Gutachter: 1. Prof. Dr. Joachim Dzubiella
2. Prof. Dr. Jürgen P. Rabe
3. Prof. Dr. Martin Schoen

Tag der mündlichen Prüfung: 23.11.2015

To my family, in memory of my father

*“An expert is a person who has made all the mistakes
that can be made in a very narrow field.”*

– Nils Bohr –

This thesis is based on the following original papers and preprint:

- Paper I: C. Yigit, N. Welsch, M. Ballauff, and J. Dzubiella, “Protein Sorption to Charged Microgels: Characterizing Binding Isotherms and Driving Forces”, *Langmuir*, 2012, 28 (40), pp. 14373–14385
- Paper II: M. Oberle, C. Yigit, S. Angioletti-Uberti, J. Dzubiella, and M. Ballauff, “Competitive Protein Adsorption to Soft Polymeric Layers: Binary Mixtures and Comparison to Theory”, *J. Phys. Chem. B*, 2015, 119 (7), pp. 3250–3258
- Paper III: C. Yigit, J. Heyda, and J. Dzubiella, “Charged Patchy Particle Models in Explicit Salt: Ion Distributions, Electrostatic Potentials, and Effective Interactions”, submitted to *J. Chem. Phys.*
- Paper IV: C. Yigit, J. Heyda, M. Ballauff, and J. Dzubiella, “Like-Charged Protein-Polyelectrolyte Complexation Driven by Charge Patches”, submitted to *J. Chem. Phys.*
- Preprint I: C. Yigit, M. Kanduc, M. Ballauff, and J. Dzubiella, “Interaction of charged patchy protein models with like-charged polyelectrolyte brushes”, in preprint

Not included in this thesis:

- Paper V: S. Yu, X. Xu, C. Yigit, M. van der Giet, W. Zidek, J. Jankowski, J. Dzubiella, and M. Ballauff, “Interaction of Human Serum Albumin with Short Polyelectrolytes: A Study by Calorimetry and Computer Simulation”, submitted to *Soft Matter*

Author's contributions to the joint papers and preprint:

- Paper I: I developed the theoretical model, its numerical implementation and carried out all calculations in the paper. I significantly contributed to the discussion and revision of the paper. Dr. Nicole Welsch conducted the experiments and contributed to the discussion and revision of the paper. This research study was supervised by Professor Ballauff and Professor Dzubiella.
- Paper II: I analytically modeled the binding isotherms of single-type protein adsorption and predicted the competitive protein adsorption. Michael Oberle conducted the experiments. He and I wrote the paper together and contributed equally to the discussion and revision of the paper. Stefano Angioletti-Uberti, Ph.D., contributed to the discussion and revision of the paper. This research study was supervised by Professor Dzubiella and Professor Ballauff.
- Paper III: I constructed the charged patchy particle models. I set up, carried out, and evaluated all computer simulations. I significantly contributed to the discussion and revision of the paper. Jan Heyda, Ph.D., contributed to the discussion and revision of the paper. This research study was supervised by Professor Dzubiella.
- Paper IV: I constructed the models, set up, carried out, and evaluated all computer simulations. I significantly contributed to the discussion and revision of the paper. Jan Heyda, Ph.D., and Professor Ballauff contributed to the discussion and revision of the paper. This research study was supervised by Professor Dzubiella.
- Preprint I: I constructed the models, set up, carried out, and evaluated all computer simulations. I significantly contributed to the discussion and revision of the preprint. Matej Kanduc, Ph.D., and Professor Ballauff contributed to the discussion and revision of the preprint. This research study was supervised by Professor Dzubiella.

Abstract

Protein adsorption is ubiquitous in many biotechnological applications and has become a central research field in soft matter. Understanding the driving forces behind protein adsorption would allow a better control of the adsorption process and the development of biosystems with unprecedented functionality. In this thesis, protein adsorption onto soft polymeric biomaterials and their physical interactions is studied theoretically by using two different and newly developed approaches: 1) continuum binding models based on Langmuir and Boltzmann models in direct comparison to experiments and 2) Langevin dynamics computer simulations to characterize pair interactions on microscopic scales.

In the first part, a novel multi-component cooperative binding model is developed to describe the equilibrium adsorption of proteins onto microgels. The well-defined microgel system consists of a solid polystyrene core and a thermosensitive shell of cross-linked poly N-isopropylacrylamide with acrylic acid as a copolymer to introduce charge. Proteins of interest are lysozyme from chicken egg white, cytochrome c from bovine heart, papain from papaya latex, and ribonuclease A from bovine pancreas. In contrast to the Langmuir model, the application of this approach to experimental adsorption isotherms enables a more quantitative interpretation of the binding affinity in terms of separate physical interactions. It was thus possible to correctly identify the *true* driving force behind the protein adsorption which was found to be mainly of electrostatic origin. A key achievement by the cooperative binding model is the prediction of competitive protein adsorption and desorption onto the microgel that is based on thermodynamic parameters related to single-type protein adsorption without any variable parameters. Comparisons between experimental data of binary protein mixtures and theoretical calculations have shown excellent agreements.

The second part is focused on protein interactions with polyelectrolyte materials to elucidate adsorption processes on a microscopic level. For this purpose, charged patchy particles are constructed and used as protein models while a simple bead-spring model is employed for the polyelectrolyte and polyelectrolyte brush. A central aspect was the determination of the associated free energy, the potential of mean force (PMF), on the complex formation between the two constituents with comparisons to theoretical model developments. In particular the influence of important physical parameters, such as the degree of patchiness, the salinity, and the chain length on the complexation, were systematically investigated. The simulation results evidenced a complex interplay of electrostatic forces and ion release mechanisms to be responsible for the strong attractive interactions observed in the PMFs.

Results from this thesis have provided precious insights into the interactions in protein adsorption processes. This findings may serve as a basis not only for further experiments but also for testing approximative theories.

Key words: protein adsorption, microgels, cooperativity effects, competitive adsorption, Langevin dynamics, like-charged complexation, patchy particles, polyelectrolyte brush

Zusammenfassung

Proteinadsorption ist in vielen biotechnologischen Anwendungen ubiquitär und ein zentrales Forschungsfeld in der Physik der weichen Materie. Das Verstehen der treibenden Kräfte hinter der Proteinadsorption würde zu einer besseren Kontrolle des Adsorptionsprozesses führen und die Entwicklung von Biosystemen mit beispielloser Funktionalität ermöglichen. In der vorliegenden Arbeit wird die Proteinadsorption an weichen polymerartigen Biomaterialien sowie deren physikalische Wechselwirkungen unter Verwendung von zwei unterschiedlichen neu entwickelten Ansätzen theoretisch untersucht: 1) Kontinuums-Bindungsmodelle, basierend auf Langmuir- und Boltzmann-Modellen mit direktem Vergleich zu Experimenten und 2) Langevin-Dynamik Simulationen um Paar-Wechselwirkungen auf mikroskopischen Skalen zu charakterisieren.

Im ersten Teil wird ein neues mehrkomponentiges kooperatives Bindungsmodell entwickelt, um die Gleichgewichts-Adsorption von Proteinen auf Mikrogelen zu beschreiben. Die Mikrogel-Systeme bestehen aus einem festen Polystyrolkern und einer thermosensitiven Schale aus vernetztem Poly-N-Isopropylacrylamid mit Acrylsäure als Copolymer um Ladungen einzuführen. Die untersuchten Proteine waren Lysozym aus Hühnereiweiß, Cytochrom c aus Rinderherz, Papain aus Papaya-Milchsaft und Ribonuklease A aus Rinderpankreas. Im Gegensatz zum Langmuir-Modell ermöglicht die Anwendung dieses Ansatzes an experimentelle Adsorptionsisothermen eine quantitative Interpretation der Bindungsaffinität in Bezug auf separate physikalische Wechselwirkungen. Es war somit möglich, die *wahre* treibende Kraft der Proteinadsorption zu identifizieren, die hauptsächlich elektrostatischen Ursprungs ist. Eine Errungenschaft des kooperativen Bindungsmodells ist die Vorhersage der kompetitiven Proteinadsorption und -desorption auf das Mikrogel, die auf thermodynamischen Parametern der Adsorption von Proteinen einzelner Sorten basiert. Vergleiche zwischen Experimenten mit binären Proteinmischungen und theoretischen Berechnungen zeigten sehr gute Übereinstimmungen.

Der zweite Teil fokussiert auf Protein-Wechselwirkungen mit Polyelektrolyten, um Adsorptionsprozesse auf mikroskopischer Ebene zu erklären. Dafür wurden geladene fleckige Partikel konstruiert und als Proteinmodelle verwendet, während ein einfaches Kugel-Feder-Modell für das Polyelektrolyt und Polyelektrolytbürste benutzt wurde. Ein zentraler Aspekt war die Bestimmung der freien Energie, das Potential der mittleren Kraft (PMF), für die Komplexbildung der beiden Bestandteile mit Vergleichen zur Modellentwicklungen. Insbesondere wurde der Einfluss von wichtigen physikalischen Parametern, wie zum Beispiel der Fleckigkeit, dem Salzgehalt und der Kettenlänge auf die Komplexierung systematisch untersucht. Die Simulationsergebnisse legen ein komplexes Wechselspiel von elektrostatischen Kräften und Ionenfreisetzungsmechanismen dar, die für die starken attraktiven Wechselwirkungen in den PMFs verantwortlich sind.

Die Ergebnisse dieser Arbeit haben wertvolle Einblicke in die Protein-Wechselwirkungen mit polymerartigen Materialien gewährt. Diese Erkenntnisse können als Grundlage für zukünftige Experimente und auch zur Prüfung von approximativen Theorien dienen.

Schlagwörter: Proteinadsorption, Mikrogel, kooperative Effekte, kompetitive Adsorption, Langevin Dynamik, gleich geladenen Komplexe, fleckige Partikel, Polyelektrolytbürste

Contents

1	Introduction	1
2	Objective of this thesis	5
3	Basic principles	7
3.1	Electrostatics	7
3.1.1	Poisson-Boltzmann theory	7
3.1.2	Debye-Hückel potential	10
3.1.3	Donnan equilibrium	11
3.1.4	Counterion condensation	11
3.2	Interactions between molecules	13
3.2.1	Mie potential	13
3.2.2	Derjaguin-Landau-Verwey-Overbeek potential	13
3.2.3	Orientation-averaged pair potential of mean force	14
3.3	Langevin dynamics	15
3.4	Langmuir binding model	17
3.5	Experimental methods	19
3.5.1	Isothermal titration calorimetry	19
3.5.2	Dynamic light scattering	20
3.5.3	Fluorescence spectroscopy	21
4	Theoretical description and prediction of protein adsorption onto charged core-shell microgels	23
4.1	Protein interactions with charged core-shell microgels	23
4.1.1	General model considerations	23
4.1.2	Electrostatics between proteins and CSM particles	25
4.1.3	Free energy of electrostatic transferring	27
4.1.4	Osmotic and elastic deswelling	29
4.1.5	Cooperative binding model	30
4.1.6	Numerical evaluation including volume change	33
4.2	Experimental materials	34
4.3	Experimental and theoretical results of one-component binding	36
4.3.1	CSM deswelling by salt and proteins	36
4.3.2	Characterizing experimental binding isotherms	38
4.3.3	The total binding energy	41
4.3.4	Interpretation of Langmuir and cooperative binding model results . .	42
4.4	Competitive protein adsorption of binary mixtures: comparison between experiment and theory	43

4.5	Concluding remarks	44
5	Simulation of protein adsorption onto soft polymeric biomaterials	47
5.1	Models and methods	47
5.1.1	Charged patchy protein models	47
5.1.2	Polyelectrolyte and polyelectrolyte brush models	48
5.1.3	Simulation method and details	49
5.1.4	Calculating the potential of mean force	51
5.1.5	Ion counting and patch orientation	51
5.2	Simulations of charged patchy proteins	52
5.2.1	Ionic and potential distribution around a single protein	52
5.2.2	Effective interaction between two proteins	57
5.3	Like-charged protein-polyelectrolyte complexation	62
5.3.1	Reference simulations	64
5.3.2	Influence of protein patchiness and salinity on complexation	66
5.3.3	Influence of polyelectrolyte chain length on complexation	70
5.4	Protein uptake by a polyelectrolyte brush	73
5.4.1	Reference simulations	75
5.4.2	Uptake of like-charged patchy proteins	77
5.4.3	Uptake of charge-inversed proteins	83
5.5	Concluding remarks	84
6	Summary and Outlook	85
	Appendix A The Newton-Raphson method	89
	Appendix B Quadrupole moments of charged patchy proteins	91
	Appendix C List of abbreviations	93
	Bibliography	97
	Acknowledgments	113

1 Introduction

Proteins are essential constituents of living cells and jointly responsible for the genesis of life [1, 2]. Their unique three-dimensional structures exhibit special properties and serve versatile functions in virtually all physiological or biological processes [3]. Elucidating the nature of protein interactions – particularly with nanoparticles – is crucial for designing new biomaterials for applications in bioengineering, pharmaceuticals, and food processing [4, 5]. Specifically, nanoparticles with polymeric coatings (depicted in Figure 1.1) have been the object of intense investigations [6]. These kinds of nanomaterials are suited outstandingly for protein immobilization or may serve as protective coatings to prevent protein adsorption with regard to non-fouling surfaces [7–9]. In respect of the former, one promising biomedical example is protein encapsulation into polymeric materials as *drug delivery* systems for a controlled release of therapeutic proteins in the human body [10–12]. Particularly multi-responsive microgels with a core-shell morphology are of great interest because of their biocompatibility, resemblance to biological tissue, and tunable viscoelastic properties [13–20]. The characterization of such systems have shown that protein adsorption onto the microgel is an equilibrium process and, besides, proteins largely retain their native structure [21, 22]. Recent studies have also indicated that adsorption of proteins onto nanoparticles in general is mostly driven by global, nonspecific electrostatic interactions and more local, probably hydrophobic interactions [13, 22–31]. The balance between these two is highly system-specific and can be manipulated by chemical functionalization or copolymerization. For instance, *charged* core-shell microgels can be used to favor or disfavor the adsorption of charged proteins. Their osmotic swelling and storage volume can be tuned by different external stimuli such as pH, temperature change, salt concentration and charge density [14, 15, 30, 32] essentially via the Donnan equilibrium [33]. However, during protein adsorption swelling and Donnan equilibria are typically changing in an interconnected fashion [24, 29–31]. These highly cooperative effects render the interpretation of binding isotherms, and thus the separation and quantification of global electrostatic and local hydrophobic contributions to binding – a difficult task. Binding affinities in these systems also depend on protein load,

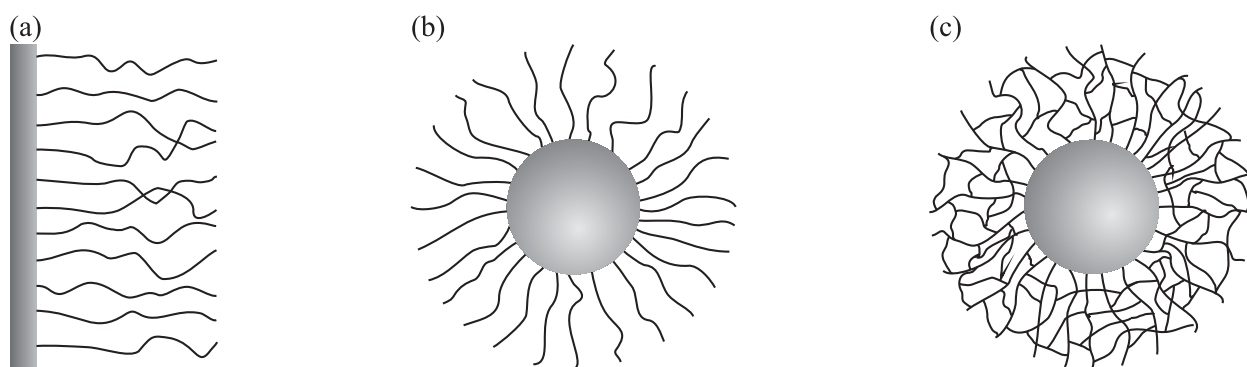


Figure 1.1: Representation of surfaces with polymeric coatings: (a) planar polyelectrolyte brush, (b) spherical polyelectrolyte brush, and (c) core-shell microgel particle.

which presents an additional complication when modeling adsorption isotherms.

The rich chemistry in synthesis enables the covalently anchoring of polyelectrolytes (PE) at one end to a substrate surface of any geometry forming a PE brush as represented in Figure 1.1 (a) and (b) [34]. A seminal study of Wittemann *et al.* [35] investigated the adsorption of bovine serum albumin (BSA) onto a spherical PE brush at different pH and ionic strengths. Their experiments allow the unequivocal conclusion of significant protein uptake into the PE brush at a pH above the isoelectric point (pI) of BSA although both objects are like-charged. While the protein adsorption sharply rises at pH close to the pI, it disappears at high ionic strengths. The researchers concluded from this fact that the ionic strength is the decisive factor for protein adsorption whereas the pH is of secondary importance and determines only the adsorption strength. The desire to understand the mechanisms for attraction or repulsion of proteins by PE brushes presents a complex problem and is still under debate [36]. Only two popular statements for this phenomenon can be found in the literature [35, 37–40]. One explanation from Wittemann *et al.* [35, 38] refers to the effect of counterion release. From this view, the vast majority of monovalent counterions are initially confined within the PE brush. Since negatively charged proteins may possess positively charged patches on their surface, they will serve as multivalent counterions of the PE chains. Thus, once the protein enters into the PE brush, counterions from the PE chains and those of the positive patch will be released. This entropic process drives the protein adsorption and leads to a favorable electrostatic interaction between the positive patch and PE chains. The counterion release effect has been confirmed by Leermakers *et al.*, who have used a two-gradient self-consistent field theory [40]. Another possible explanation proposed by Biesheuvel *et al.* is the charge regulation of amphoteric proteins [37, 39]. In their reasoning, the local pH inside the PE brush differs from the bulk solution. This may happen at conditions with low ionic strengths where the pH is even lower than the pI of the protein. In response to the pH change, a charge reversal of the protein occurs and promotes the adsorption between oppositely charged objects. Their model calculations have only achieved qualitative agreement with experimental data at pH close to the pI and low ionic strengths. Another study by de Vos *et al.* has considered both effects together in a self-consistent field theory, instead of investigating them separately [36]. The authors have found that both effects can indeed justify protein uptake by a like-charged PE brush while in their view the charge regulation is the predominant effect. This thesis also aims to study the mechanisms of protein uptake by a PE brush.

Usually, when dealing with real biological fluids, *e.g.* blood plasma, a large number of heterogeneous proteins rather than single-type proteins are present. Cooperative and/or competitive adsorption onto nanoparticles take place in this kind of biological milieu and influence the adsorption process immensely. For instance, nanoparticles injected into the bloodstream will be immediately covered with proteins and lead to a formation of a *protein corona* as shown in Figure 1.2 [41]. This protein corona will then determine the interaction between the nanoparticles and the host environment [42]. In the late 1960s, Vroman and

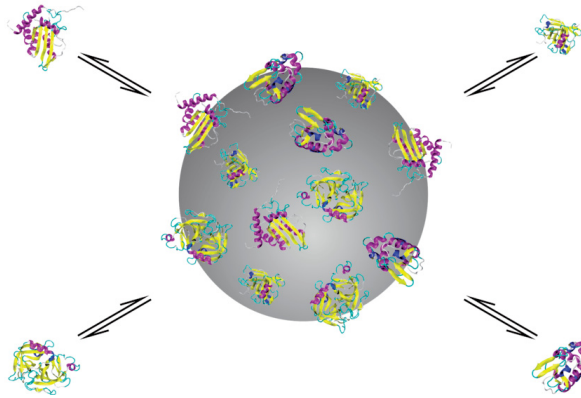


Figure 1.2: A schematic illustration of the protein corona formation around a spherical nanoparticle.

Adams investigated the adsorption of blood plasma proteins at liquid and solid interfaces [43]. They observed a rapid adsorption of fibrinogen proteins at the initial stage while later these first adsorbers were sequentially exchanged by other plasma proteins. This so-called *Vroman effect* [44] relates competitive adsorption and desorption of proteins to their individual concentration, diffusion coefficient, and adsorption affinity. It is generally stated that proteins with high concentration and mobility will adsorb faster but will be replaced by less motile proteins with higher binding affinities to the nanomaterial [45]. The Vroman effect is not restricted only to plasma proteins and can be considered as a general trend for other protein mixtures [46, 47]. Beside many other experiments on competitive protein adsorption [21, 48–51], there is no generalizable multi-component model describing the equilibrium thermodynamics of competitive protein adsorption onto soft polymeric layers. This lack is still challenging and a topic of this thesis.

Understanding the formation of protein-PE complexes is a necessary prerequisite to understand interactions between proteins and nanoparticles with polymer coatings. Numerous experiments [52–59], comprehensive reviews [60, 61], different theoretical approaches [62–69] and computer simulation studies [68, 70–83] have been carried out to uncover the interactions between proteins and PEs. For instance, Hattori *et al.* [54] and Seyrek *et al.* [55] have measured the binding affinity of few PEs to different proteins such as β -lactoglobulin, BSA, insulin, and lysozyme at various pH and ionic strengths. The researchers have found some complexes at a pH where both objects are negatively charged and concluded therefrom the existence of oppositely charged patches on the protein’s surface. This observation has been known as protein adsorption on the wrong side of the pI. De Vries also assumed this binding interpretation and studied the complexation of a PE with whey proteins at their pI by means of Monte Carlo (MC) simulations [79]. His results have revealed a stronger PE binding to α -lactalbumin than to β -lactoglobulin. He also justified these findings by a statistical analysis of the surface charges in which he found a single and large positively charged patch on α -lactalbumin and multiple, but smaller charged, patches on β -lactoglobulin. Hence, patchiness or rather surface charge anisotropies have irrefutable effects on protein-PE complexation. This thesis will also deal with the complex formation between a protein and a

single PE.

Many of the computational and theoretical investigations referenced above have focused on the interaction between a PE and an oppositely charged particle or a planar surface. However, simulations and analytical models of like-charged protein-PE association events are rarely reported in the literature. Very few key publications in this field are from, for instance, Messina and co-workers [76]. They have studied the conformation of a colloid with a long PE (both negatively charged) at different Coulomb couplings in a salt-free environment by means of Langevin dynamics. At strong Coulomb couplings, the PE chain, once adsorbed, is confined on the colloidal surface while at weak Coulomb couplings the PE is still adsorbed, but only partly and looped. More recently, Luque-Caballero *et al.* [83] have employed MC simulations to study PE adsorption onto a like-charged planar surface in the presence of trivalent counterions. The authors have demonstrated a preferential adsorption of the PE onto the planar surface by calculating the free energy between the objects. Their free energy analysis covered the effects of surface charge density, PE charge, ionic strength, and cation size. In contrast, much less is known about the role of charged patchy globular particles whereas their surface is both, repulsive and attractive [84]. This gap is a demanding subject and will be systematically investigated in this thesis.

A better understanding of interactions between proteins and polymer coated nanoparticles would significantly help to elucidate the adsorption process and the potential to develop biospecific nanomaterials. The principal research aim of this thesis is to study and predict protein adsorption onto polymeric materials. Beside ambitious experiments and theoretical modeling, computer simulations are complementary approaches to investigate complex processes in soft matter systems in detail. Especially the natural presence of surface charge anisotropies, counterions, electrolytes and thus the many-body interactions complicates the analytical modeling to a large extent. One possible way to gain insight into the complexation of proteins with polymeric materials can be realized by computing the potential of mean force (PMF) between them. Basically, the PMF can be regarded as the free energy landscape, *e.g.* of two interacting objects that move towards a *separate state* to a *bound state*. Computer simulation techniques such as steered molecular dynamics (SMD) [85] or umbrella sampling (US) [86] are usually employed in this particular research field to compute free energy profiles. For instance, SMD simulations have become an integral part to describe the physical mechanisms in experiments of binding/unbinding of proteins, conformational transition of DNA fragments and other biomolecular processes [85, 87]. Thus, computer simulations facilitate interpretations and may assist to reveal driving forces behind protein adsorption. Nevertheless, the study of adsorption processes is a challenging task and still far from being completed.

2 Objective of this thesis

The purpose of this thesis is to study and rationalize interactions between proteins and soft polymeric layers with the main focus on electrostatic interactions. The particular goals are: 1) modeling of experimental adsorption isotherms to provide an enhanced insight into the driving forces of protein adsorption onto core-shell microgels and 2) systematic computational investigations of the influence of different physical and physiological parameters on the interactions between proteins and polymeric materials for a better understanding of the adsorption process. With this in mind, the present thesis is organized as follows:

Chapter 3 introduces the basic physical principles and experimental methods on which this thesis is based.

In **Chapter 4**, the subjects of Papers I and II are reflected. A new theoretical approach is developed for modeling protein adsorption onto core-shell microgels and soft polymeric layers in general. This binding approach includes cooperative effects and is easily expandable to a multi-component solution of proteins. It also enables a more detailed investigation of the driving forces of protein adsorption. While first the microgel deswelling by salt and proteins is explained, an in-depth analysis and discussion of single-type protein adsorption onto the microgel is presented afterwards. The cooperative binding approach and the standard Langmuir binding model are tested in particular by fitting experimental binding isotherms. Consequences to the interpretation of Langmuir binding models are discussed. A major aspect of this chapter is the competitive adsorption of a binary protein mixture onto the core-shell microgel. Protein adsorption and desorption are predicted from thermodynamic parameters obtained previously from fitting.

Chapter 5 is based on Papers III, IV, and Preprint I, which presents a series of Langevin dynamics simulations of different protein association events. The simulations are carried out in an explicit monovalent ionic solution and implicit solvent. Here, a set of charged patchy particle models are designed and used as protein models. Simple coarse-grained models are also developed for a single polyelectrolyte and a polyelectrolyte brush. The aim of this chapter is to investigate the effective interaction between like-charged proteins, formation of like-charged protein-polyelectrolyte complexes, and the uptake of oppositely and like-charged proteins by a polyelectrolyte brush. A particular focus is set on determining the potential of mean force between these objects depending on the salt concentration, patch number and size, different dipole moments, and polyelectrolyte chain lengths. The potentials of mean force in conjunction with an analysis of the patch orientations, ion condensation and release effects will then give valuable insights into the association events. They may reveal and uncover the driving forces behind the adsorption process. Some of these results are compared with currently available analytical theories.

Finally, **Chapter 6** summarizes this thesis and remarks on possible outlook.

3 Basic principles

This chapter describes theoretical fundamentals and experimental methods related to protein adsorption processes relevant for this thesis. After a recap of some electrostatic aspects and molecular interactions, a brief introduction to Langevin dynamics and to the Langmuir binding model is given. The experimental techniques employed by co-workers for investigating protein adsorption are summarized in the remainder.

3.1 Electrostatics

3.1.1 Poisson-Boltzmann theory

The Poisson-Boltzmann (PB) theory describes electrostatic effects of molecules in solvents with dissolved ions on a mean-field level. For instance, ionic profiles or electrostatic contributions to free energies of association events can be determined from the solution of the PB equation [88]. Its derivation is outlined briefly based on a density functional theory following reference [89].

Consider a system of a molecule with a fixed charge distribution $\rho_f(\mathbf{r})$ and N mobile ions (counterions and coions) with densities $n_{\pm}(\mathbf{r})$ in a solution of volume V and temperature T . If only Coulombic interactions between all particles are assumed the Hamiltonian \mathcal{H} of the entire system is then given by [89]

$$\mathcal{H}(\mathbf{p}, \mathbf{r}) = \sum_{i=1}^N \frac{\mathbf{p}_i^2}{2m_i} + \frac{e^2}{2} \sum_{i=1}^N \sum_{\substack{j=1 \\ i \neq j}}^N \frac{Z_i Z_j}{4\pi\epsilon_0\epsilon_r |\mathbf{r}_i - \mathbf{r}_j|} + \sum_{i=1}^N Z_i e \int_V \frac{\rho_f(\mathbf{r})}{4\pi\epsilon_0\epsilon_r |\mathbf{r}_i - \mathbf{r}|} d^3\mathbf{r}. \quad (3.1)$$

Here, \mathbf{p}_i and m_i are the momentum and mass of the i th ion, e the elementary charge, ϵ_0 the dielectric constant, ϵ_r the relative permittivity of the solvent, and Z_i the charge valency of ion i . Indeed, such a system exhibit a high degree of physical complexity due to interparticle correlations. To be more precise, the calculation of the partition function $\mathcal{Z} = \text{Tr} \{e^{-\beta\mathcal{H}(\mathbf{p}, \mathbf{r})}\}$ of this particular system is very complicated due to the combinatorial interactions in the Hamiltonian. The thermal energy of the system at the temperature T is denoted by $\beta^{-1} = k_B T$ with k_B being the Boltzmann constant. One route to overcome this difficulty while retaining a quantitative description is the use of mean field approaches.

A mean-field approximation (MFA) neglects particle correlations by replacing the N -particle probability distribution $\mathcal{P}_N(\mathbf{r}_1, \dots, \mathbf{r}_N)$ by an approximate distribution that is a product of N identical single-particle probability distributions [89]

$$\mathcal{P}_N(\mathbf{r}_1, \dots, \mathbf{r}_N) \xrightarrow{\text{MFA}} \mathcal{P}(\mathbf{r}_1)\mathcal{P}(\mathbf{r}_2) \cdots \mathcal{P}(\mathbf{r}_N), \quad (3.2)$$

with $\mathcal{P}(\mathbf{r})$ being the single-particle probability distribution, which is associated with the

particle density $n(\mathbf{r})$ via

$$\mathcal{P}(\mathbf{r}) = \frac{n(\mathbf{r})}{\int_V n(\mathbf{r}) d^3\mathbf{r}} = \frac{n(\mathbf{r})}{N}. \quad (3.3)$$

The canonical partition function can then be factorized into an ideal (purely entropic) and an excess contribution [90]. Consequently, the Helmholtz free energy $\beta\mathcal{F} = -\ln[\mathcal{Z}]$ of the system reads

$$\mathcal{F}_{\text{PB}} = \mathcal{F}_{\text{id}} + \mathcal{F}_{\text{ex}}, \quad (3.4)$$

where the subscript PB denotes the Poisson-Boltzmann approximation for the Helmholtz free energy. The Bogoliubov inequality provides an upper bound for the exact Helmholtz free energy, namely $\mathcal{F} \leq \mathcal{F}_{\text{PB}}$ [91]. With the requirements given above, \mathcal{F}_{id} and \mathcal{F}_{ex} can be calculated leading to the PB free energy density functional

$$\mathcal{F}_{\text{PB}}[n_{\pm}(\mathbf{r})] = \int_V \left\{ \frac{1}{\beta} \sum_{i=f,+, -} n_i(\mathbf{r}) \left\{ \ln[n_i(\mathbf{r})\Lambda^3] - 1 \right\} + \left\{ \rho_f(\mathbf{r}) + \frac{e}{2} \sum_{i=+, -} Z_i n_i(\mathbf{r}) \right\} \phi(\mathbf{r}) \right\} d^3\mathbf{r}, \quad (3.5)$$

where Λ is the thermal de Broglie wavelength and $\phi(\mathbf{r})$ is the total electrostatic potential at \mathbf{r} and related to Poisson's equation [90].

The ion density profiles $n_{\pm}(\mathbf{r})$ can be obtained by minimizing $\mathcal{F}_{\text{PB}}[n_{\pm}(\mathbf{r})]$ with respect to $n_{\pm}(\mathbf{r})$ by considering that the ion number $N_{\pm} = \int_V n_{\pm}(\mathbf{r}) d^3\mathbf{r}$ is fixed by varying $n_{\pm}(\mathbf{r})$. This constraint is achieved by adding the Lagrange multiplier $\mu_{\pm} \int_V n_{\pm}(\mathbf{r}) d^3\mathbf{r}$ (chemical potential) to the PB functional [92]. Applying the variational method, the corresponding functional derivative takes the form

$$\frac{\delta \mathcal{F}_{\text{PB}}[n_{\pm}(\mathbf{r})]}{\delta n_{\pm}(\mathbf{r})} = Z_{\pm} e \phi(\mathbf{r}) + k_B T \ln[n_{\pm}(\mathbf{r})\Lambda^3] - \mu_{\pm} \stackrel{!}{=} 0, \quad (3.6)$$

and yields to the equilibrium density profiles

$$n_{\pm}(\mathbf{r}) = n_{\pm}^0 e^{-Z_{\pm} e \beta \phi(\mathbf{r})}. \quad (3.7)$$

The constant $n_{\pm}^0 = \Lambda^{-3} e^{\beta \mu_{\pm}}$ is the particle density at $\phi(\mathbf{r}) = 0$. Thus, the ion density profile at a given position \mathbf{r} are proportional to a Boltzmann factor that describes an exponential weighting between the electrostatic potential energy $Z_{\pm} e \phi(\mathbf{r})$ and the thermal energy $k_B T$. Combining the Boltzmann distribution of the ions with Poisson's equation leads to the well-known PB equation [89]

$$\nabla^2 \phi(\mathbf{r}) = -\frac{4\pi}{\epsilon_0 \epsilon_r} \left\{ \sum_{i=+, -} Z_i e n_i^0 e^{-Z_i e \beta \phi(\mathbf{r})} + \rho_f(\mathbf{r}) \right\}. \quad (3.8)$$

The PB equation (3.8) represents a partial differential equation of the second order. It can be solved analytically only for a few cases where usually the fixed charge distribution of the molecule $\rho_f(\mathbf{r})$ is incorporated into Dirichlet or Neumann boundary conditions such that

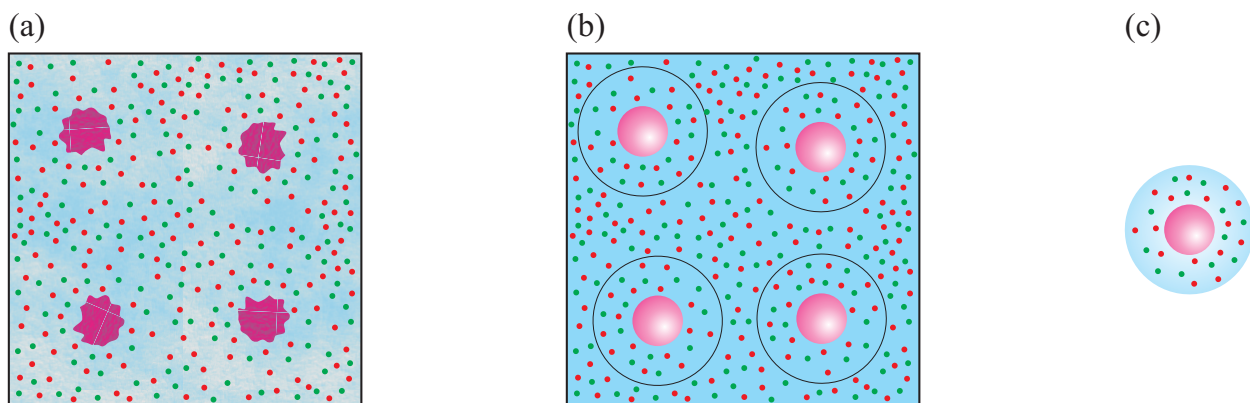


Figure 3.1: A sketch of the PB cell model. The biomolecular solution (a) is subdivided into cells (b) which contain a molecule, counterions and salt ions. Since the individual cells are electrically neutral, correlations between the molecules are repealed. The complex system then reduces to an one-body problem (c).

$\rho_f \equiv 0$ [89] in the domain of interest.

Cell model and electric double layer

If symmetries are present in the molecular solution then the so-called cell model within the PB theory can be applied to facilitate the analytical calculus [89]. In this model each molecule is centered in a cell together with its mobile counterions to ensure electroneutrality and possibly salt ions as depicted in Figure 3.1 [89]. The cell shape reflects the molecules geometry and, therefore, simplifies the analytical treatment of the PB equation with respect to this specific geometry and appropriate boundary conditions as well. The physical prerequisites demand that the electric field vanishes on the cell boundary (Gauss' law) and is fixed on the molecular surface. Consequently the cells do not interact with each other and lead thus to a decoupling of the correlations between the molecules. When doing so, the molecular solution is then approximated by an effective one-body model [89].

The charged molecular surface gives rise to an attraction of counterions and a repulsion of coions leading to a region of two different phases that is referred to as the electrical double layer [93]. In the simplest theoretical treatment, counterions adsorb directly on the molecular surface and compensate it [94]. The ensuing layer is called the Helmholtz layer whose thickness is determined by the finite size of the counterion [94]. However, the thermal motion of the ions cause a drifting from the molecule's surface leading to a diffuse layer as proposed by Gouy and Chapman [94]. The distribution of the charged ions in the diffuse layer obey Boltzmann statistics which is why the electrostatic potential decreases exponentially from the molecular surface [94]. Although the Gouy-Chapman model constitutes an improvement of the Helmholtz model, however, the physical applicability is limited because of its assumptions. It describes the ions as point charges that freely approach the molecular surface which is not possible in reality. Later, Stern combines the Helmholtz layer with the Gouy-Chapman diffuse layer and hence accounts for ionic sizes [93]. The arising layer close to the molecular surface is called the Stern layer [93]. Furthermore, only Coulombic interactions in the diffuse layer and a constant dielectric permittivity throughout

the double layer are assumed [93].

Limitations of the PB theory

The approximations made in this theory have only a certain range of validity and, consequently, it breaks down at some point. First, it is not possible to elaborate ion-ion correlations or other ion specific effects by the PB theory because only an averaged potential is assumed to account for all ionic interactions. Second, the finite size of the ions and other atomic properties are neglected. Third, the ions are modeled as point charges and are only distinguished by their valence. Fourth, the polarizability of the aqueous solution is not considered and it is treated as a dielectric constant with a relative permeability (primitive model). Given these limitations of the PB theory, it describes ionic effects to molecules in solutions with monovalent electrolytes surprisingly adequate [89]. However, it deviates considerably for asymmetric or multivalent electrolytes [89]. In the latter case, the disparity to the predictions from the PB theory is due to the strong Coulomb coupling between molecules and multivalent counterions and the fact that correlations between discrete multivalent charges become relevant [95, 96]. In systems with monovalent ions the Coulomb coupling is weak [96] and *errors* introduced by the approximations leads to opposite effects and cancel each other out [93]. This is why mean-field theories are applicable. For instance, if the finite size of the ion is considered the ion concentration on the molecule's surface will be lower and consequently the surface potential will increase. However, solvent molecules in the electric field of molecules are less free in their orientation than in the bulk and, therefore, the relative permeability is smaller in the vicinity of the molecular surface giving rise to a lower surface potential. These two examples show that mutual effects may balance each other under certain conditions.

In this work, solutions are considered that contain only monovalent electrolytes and concentrations allowing to compare with the PB theory.

3.1.2 Debye-Hückel potential

The radial electrostatic potential $\phi(r)$ surrounding a charged molecule in an implicit solvent with Boltzmann-distributed monovalent salt $c_{\pm}(r)$ reads [97]

$$\nabla^2 \phi(r) = \frac{8\pi e c_s}{\epsilon_0 \epsilon_r} \sinh[e\beta \phi(r)], \quad (3.9)$$

at salt bulk concentration c_s . By using the approximation $e\beta \phi(r) \ll 1$ and rescaling the electrostatic potential $\Phi(r) \equiv e\beta \phi(r)$ the PB equation can be linearized to yield the linearized PB (LPB) equation

$$\nabla^2 \Phi(r) = \kappa^2 \Phi(r), \quad (3.10)$$

where $\kappa = \sqrt{8\pi \lambda_B c_s}$ is the inverse Debye screening and $\lambda_B = \frac{e^2}{4\pi \epsilon_0 \epsilon_r k_B T}$ is the Bjerrum length. The LPB is essentially equivalent to Debye-Hückel (DH) theory [97]. For simple

homogeneously charged spheres the solution is [98]

$$\Phi_{\text{DH}}(r) = Z\lambda_B \cdot \frac{e^{\kappa R}}{1 + \kappa R} \cdot \frac{e^{-\kappa r}}{r}, \quad (3.11)$$

with Z and R being the sphere net charge valence and radius, respectively. The corresponding ion density profiles are $c_{\pm}(r) = c_s \{1 \mp \Phi_{\text{DH}}(r)\}$.

3.1.3 Donnan equilibrium

Suppose that a charged microgel particle with a permeable boundary is placed in an aqueous solution with a concentration c_s of monovalent salt ions ($Z_{\pm} = \pm 1$). In such a situation, the boundary acts as a selective barrier and hinders counterions from diffusing away while coions remain in the bulk. The resulting unequal distribution of ions causes an electrostatic potential difference between the inside and the outside of the charged microgel and establishes a Donnan equilibrium. The so-called Donnan potential can then be derived by the electroneutrality constraint on the microgel via

$$c_s e^{-\Phi_D(y)} - c_s e^{\Phi_D(y)} + Z_M c_M = 0, \quad (3.12)$$

and, therefore, leading to [33]

$$\Phi_D(y) = \ln \left[y + \sqrt{y^2 + 1} \right] \quad \text{with} \quad y = \frac{Z_M c_M}{c_s}. \quad (3.13)$$

$\Phi_D(y)$ is the dimensionless Donnan potential scaled by the factor $e\beta$ while y denotes the charge ratio between the microgel and the charge densities in the bulk. Z_M and c_M are the charge valency and concentration of the microgel. The diffusion of the ions also induces an osmotic pressure in equilibrium. For ideal solutions (ideal gas limit), the osmotic pressure of the ions p_{ion} can be determined by the difference of ionic concentrations from the inside and the outside of the microgel by [33]

$$\begin{aligned} \beta p_{ion}(y) &= c_s e^{-\Phi_D(y)} + c_s e^{\Phi_D(y)} - 2c_s \\ &= 2c_s \{ \cosh[\Phi_D(y)] - 1 \}. \end{aligned} \quad (3.14)$$

3.1.4 Counterion condensation

The concept of counterion condensation goes back to the mean-field 'Onsager-Manning-Oosawa' theories [99–102] that predict counterion condensation on highly charged rod-like molecules, *i.e.*, a fraction of the neutralizing counterions are tightly bound within a critical radial distance from the polyelectrolyte backbone while the remaining, screening ones are diluted away in the bulk. Whether at all and to what extent counterion condensation for

monovalent systems takes place is then described by the so-called Manning parameter

$$\Gamma = \frac{\lambda_B}{b}, \quad (3.15)$$

where b is the averaged distance between charged monomers. According to Onsager-Manning-Oosawa theory, counterion condensation occurs if $\Gamma > 1$, *i.e.*, the Manning parameter exceeds unity. The theory predicts in the limit of vanishing salt that a fraction of $f_{con} = 1 - \frac{1}{\Gamma}$ of counterions is condensed on the polyelectrolyte in a highly dense state. For a fully charged polyelectrolyte with N_{mon} monomers, that implies that on average $f_{con} \cdot N_{mon}$ charges on the polyelectrolyte are neutralized by bound counterions.

Record and Lohman utilized this fact to explain salt concentration dependencies of the binding affinities $w_b(c_s)$ of charged ligand – nucleic acid associations and predicted, under some assumptions, that [103]

$$\beta w_b(c_s) \propto \tilde{N} \ln[c_s], \quad (3.16)$$

where \tilde{N} reflects the number of strongly bound (and high density) ions released from the polyelectrolyte chains upon complexation. Note that in their formulation the number \tilde{N} includes both, condensed counterions $f_{con} \cdot N_{mon}$ as well as the number of screening ions within the dense DH double layer around the polyelectrolyte. The physics behind Eq. (3.16) is simply understood by the fact that \tilde{N} ions are released into bulk with a much lower salt concentrations upon complexation, leading to substantial gain in translational entropy of the ions. Note that a clear distinction between condensed ions and densely bound screening ions is not always strictly possible at finite salt concentrations [104] and flexible chains. The approach of Record and Lohman describes semi-quantitatively the complexation of pairs of short, highly charged polyelectrolyte chains, where ions are indeed confined in a well-defined fashion [103].

Henzler *et al.* introduced a similar counterion condensation/release concept to rationalize the interaction between charged globular proteins and like-charged polyelectrolyte brushes [105]. They considered that N_- counterions on a highly charged positive patch on the protein and N_+ counterions on the negative polyelectrolyte are strongly localized for large separation distances between the molecules. Upon association, a certain number ΔN_- and ΔN_+ of ions will be released. The change of the free energy for this process has then be argued to be [105]

$$\begin{aligned} \beta w_b(c_s) &\sim \beta w_{patch} + \beta w_{PE} \\ &= \Delta N_- \ln \left[\frac{c_s}{c_{patch}} \right] + \Delta N_+ \ln \left[\frac{c_s}{c_{PE}} \right], \end{aligned} \quad (3.17)$$

where c_{patch} is the concentration of ions accumulated on the positive protein patch and c_{PE} is the concentration of condensed ions in the vicinity of the polyelectrolyte. Here, a ' \sim '-symbol in Eq. (3.17) is intentionally used to express that this contribution is only anticipated to describe the leading order electrostatic contribution, not at all the total binding free energy of association. Recall that this contribution is of purely entropic origin.

3.2 Interactions between molecules

All physical and biological phenomena appearing in biomolecular solutions originate from the interaction between pairs of atoms or molecules. Because different classical and quantum mechanical effects contribute to attractive and repulsive interactions, a determination of an exact interaction potential for real systems is virtually impossible. However, from a simulation and experimental point of view, semi-empirical potentials with few adjustable physical parameters that imitate the interaction are useful to make qualitative statements about the system’s behavior. In the following sections, the interaction potentials employed in this thesis are briefly described.

3.2.1 Mie potential

The reader will find in the literature various types of pair potentials which are proposed to describe interactions between noncovalently bound atoms or molecules. The widely considered intermolecular potentials are, for example, the Buckingham [106] or the Mie [107, 108] potential that only differ in the functional form of the repulsive term from each other while the attraction is described by a van der Waals (vdW) force [109]. The Mie potential uses an inverse power term for the repulsion whereas the Buckingham potential incorporates an exponential type because of the exponential dependence of electron wave functions in quantum mechanics [110]. It is actually justifiable to represent the repulsive term by an exponential function, however, the Buckingham potential turns over at short separations. The exponential becomes a constant while the attractive term converges toward minus infinity. This can lead to unphysical bindings in simulations if molecules are too close. Moreover, when considering mixtures or different atoms there are no mixing rules available for the Buckingham potential and contemporaneous the computational cost is higher as compared to the Mie potential. It is therefore reasonable to restrict to the Mie potential (MP) which has the general form

$$U_{\text{MP}}(r) = \frac{n}{n-k} \left(\frac{n}{k}\right)^{\frac{k}{n-k}} \cdot \epsilon^* \cdot \left[\left(\frac{\sigma^*}{r}\right)^n - \left(\frac{\sigma^*}{r}\right)^k \right], \quad (3.18)$$

where the exponents $n > k$ distinguish between the repulsion and the attraction. ϵ^* is the depth of the potential well and σ^* is referred to as the van der Waals radius while r is the separation between two nonbonding atoms or molecules. An advantage of the Mie potential is the free choice of exponents to easily specify the hardness and softness of the interaction. For instance, a special case of the Mie potential with exponents $n = 12$ and $k = 6$ yields the well-known Lennard-Jones potential that gives realistic intermolecular potential [111].

3.2.2 Derjaguin-Landau-Verwey-Overbeek potential

The traditional Derjaguin-Landau-Verwey-Overbeek (DLVO) interaction between a pair of charged spherical particles assumes additivity of non-electrostatic and electrostatic contri-

butions and, therefore, is given by

$$U_{\text{DLVO}}(r) = U_{\text{MP}}(r) + U_{\text{el}}(r). \quad (3.19)$$

In the DLVO theory, the van der Waals interactions are usually expressed by the Hamaker theory. Though, in this thesis the previously introduced Mie potential U_{MP} is used to account for the attractive van der Waals and repulsive Pauli contributions. The electrostatic energy βU_{el} between two spherical molecules having charges $Q_i = Z_i e$ and radius R in monovalent ionic solution of screening length κ^{-1} and at separation r is essentially given by the solution of the LPB equation [112–114] and reads

$$U_{\text{el}}(r) = Z_1 Z_2 \lambda_B \left(\frac{\exp[\kappa R]}{1 + \kappa R} \right)^2 \frac{\exp[-\kappa r]}{r}, \quad (3.20)$$

where Z_1 and Z_2 usually play the role of effective charges [97]. The particle charge is often renormalized with respect to its intrinsic values due to various shortcomings of the DLVO theory, such as the neglect of nonlinear correlation effects and ion-specific local interaction effects on the particle surface's Stern layer. Strictly speaking, Eq. (3.20) only holds in this form in the regime $\kappa R \gg 1$, *i.e.*, for large and smooth particles at high salt concentrations. Therefore, the theory is used typically only for fitting the long-ranged part of the electrostatic interaction with renormalized charges [97].

3.2.3 Orientation-averaged pair potential of mean force

To extend the standard DLVO approach for charged spherical particles towards charge heterogeneity, an orientation-averaged potential of mean force proposed by Phillies [115] and Bratko *et al.* [116] is employed. It describes the screened electrostatic interactions between two molecules up to the dipolar contribution in the DH approximation. The relevant equations for a homogeneous dielectric medium are [115, 116]

$$U_{Q_i \mu_j}(r, \theta_j) = -\frac{Q_i \mu_j \cos[\theta_j]}{4\pi\epsilon_0\epsilon_r r^2} S_1(r) \quad (3.21)$$

for the monopole-dipole interaction, and

$$U_{\mu_i \mu_j}(r, \theta_i, \theta_j, \varphi) = -\frac{\mu_i \mu_j \{2S_2(r) \cos[\theta_i] \cos[\theta_j] - S_3(r) \sin[\theta_i] \sin[\theta_j] \cos[\varphi]\}}{4\pi\epsilon_0\epsilon_r r^3} \quad (3.22)$$

for the dipole-dipole interaction. The corresponding electrostatic screening functions are

$$S_1(r) = \frac{3e^{-\kappa(r-2R)} \{1 + \kappa r\}}{\{1 + \kappa R\} \{3 + 3\kappa R + (\kappa R)^2\}}, \quad (3.23)$$

$$S_2(r) = \frac{9e^{-\kappa(r-2R)} \{2 + 2\kappa r + (\kappa r)^2\}}{\{3 + 3\kappa R + (\kappa R)^2\}^2}, \quad (3.24)$$

and

$$S_3(r) = \frac{9e^{-\kappa(r-2R)}\{1 + \kappa r\}}{\{3 + 3\kappa R + (\kappa R)^2\}^2}, \quad (3.25)$$

respectively. The orientation-averaged pair potential of mean force (OAPP) is then given by

$$U_{\text{OAPP}}(r) = U_{\text{MP}}(r) + U_{el}(r) - k_B T \ln \left[\frac{\int e^{-\beta U(r, \theta_i, \theta_j, \varphi)} d\Omega}{\int d\Omega} \right] \quad (3.26)$$

with the total energy function

$$U(r, \theta_i, \theta_j, \varphi) = U_{Q_i \mu_j}(r, \theta_j) + U_{Q_j \mu_i}(r, \theta_i) + U_{\mu_i \mu_j}(r, \theta_i, \theta_j, \varphi), \quad (3.27)$$

and the configurational integrals

$$\int d\Omega = \int_{\theta_i=0}^{\pi} \int_{\theta_j=0}^{\pi} \int_{\varphi=0}^{2\pi} \sin[\theta_i] \sin[\theta_j] d\theta_i d\theta_j d\varphi, \quad (3.28)$$

where θ_i denotes the angle between the dipole orientation of the molecule i and r the separation between the molecules. Equation (3.26) is numerically integrated to obtain the angle-averaged potential of mean force.

3.3 Langevin dynamics

Immersing a molecule in a solvent, one is challenged with a many-body system that exhibits many degrees of freedom and interactions with solvent molecules. The permanent collisions with the solvent molecules cause a random walk of the molecule (also termed as Brownian motion) and give rise to an irregular trajectory [117]. Langevin dynamics is a way to model this motion and starts from Newton's second law of motion

$$m \frac{dv}{dt} = F, \quad (3.29)$$

where F is the acting force on the molecule from the solvent and v its velocity. For simplicity, the one-dimensional case of the dynamics is treated since the three-dimensional case is the same. Langevin ascribed the impacts from the solvent to stochastic processes and introduced friction and noise as extra forces [118]. The force F thus has two contributions: a frictional force $F_{vis} = -m\xi v$ proportional to the velocity v while ξ is the friction constant and a random force $\mathring{F}(t)$ independent of the molecules motion [118]. If the motion of the molecule is influenced by an external force $F_{ext} = -\nabla U$, the Langevin equation reads

$$m \frac{dv}{dt} = -m\xi v + F_{ext} + \mathring{F}(t). \quad (3.30)$$

The random force has to satisfy certain stochastic conditions [117]:

i. the time average vanishes

$$\langle \dot{F}(t) \rangle = 0, \quad (3.31)$$

ii. and no correlations over time

$$\langle \dot{F}_i(t) \cdot \dot{F}_j(t') \rangle = 2m\xi k_B T \delta(t - t') \delta_{ij}. \quad (3.32)$$

Treatment of long-ranged forces

Because simulations of soft matter systems are usually realized with periodic boundary conditions in order to reproduce an infinite system, special care has to be taken when dealing with long-ranged interactions [119]. For instance, the natural presence of charges in such systems gives rise to electrostatic interactions through the Coulomb potential which decays with $\frac{1}{r}$ and thus is long-ranged [119].

As an illustrative example, consider a cubic simulation box with side lengths L that contains N particles with charges q_i located at \mathbf{r}_i . The periodicity of the system is ensured by replicating the unit cell box in all spatial directions. It is further assumed that the system is electrically neutral as defined by [119]

$$\sum_{i=1}^N q_i = 0. \quad (3.33)$$

Since charges interact via the Coulomb potential, the electrostatic energy of the system is given by [119]

$$U_{Coul} = \frac{1}{2} \sum_{i=1}^N q_i \Phi(\mathbf{r}_i), \quad (3.34)$$

with

$$\Phi(\mathbf{r}_i) = \sum_{j \neq i}^N \sum_{\mathbf{n}}' \frac{q_j}{|\mathbf{r}_{ij} + \mathbf{n}L|}, \quad (3.35)$$

being the electrostatic potential of particle i at \mathbf{r}_i while the prime denotes summation over all periodic images \mathbf{n} . The sum in Eq. (3.35) converges very slowly and is also conditionally convergent [119]. A method to handle this problem is realized by the Ewald summation [119]. The basic idea of the Ewald summation is to split a single divergent sum into two converging sums which in this case leads to a separation of the charge density into a direct sum in the real space and a reciprocal sum in the Fourier space as shown in Figure 3.2. The discrete charges in the real space are screened by an opposite charge cloud that has a Gaussian shape [119]. Thereby, the interactions become short-ranged and thus can be computed in the real space. To balance this induced Gaussian charge cloud, a second Gaussian charge cloud with the same sign and magnitude as the original distribution for each point charge is added. Since this distribution is periodic, it is represented by a rapidly converging Fourier series [119].

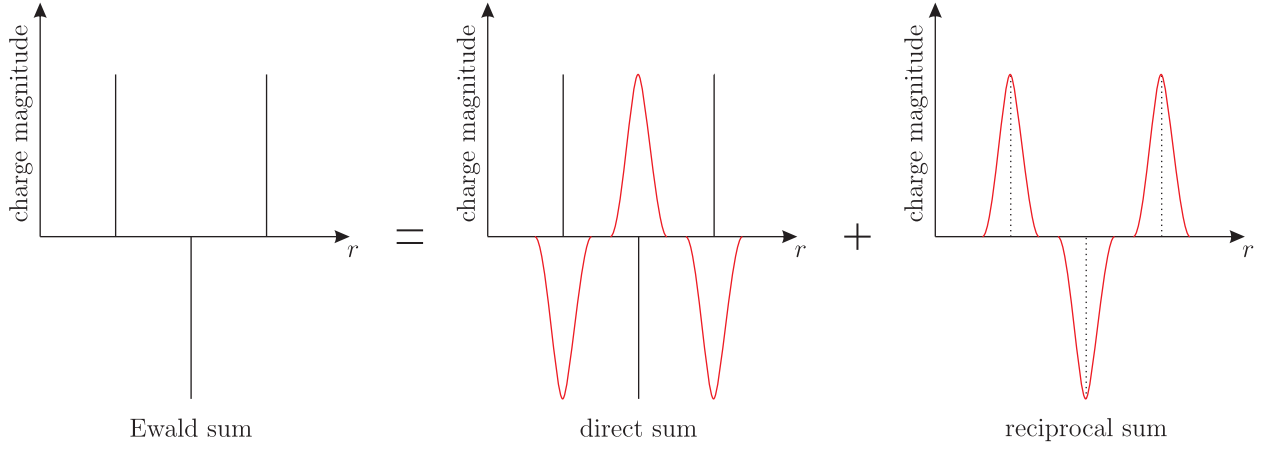


Figure 3.2: A schematic representation of the Ewald summation. The charge density is separated into a direct sum (real space) and reciprocal sum (Fourier space).

For a detailed derivation of the Fourier part the reader is referred here to reference [119].

3.4 Langmuir binding model

The Langmuir binding model describes phenomenologically the adsorption isotherm of molecules to adsorbents dependent on the molecule's concentration at a certain temperature [120]. A statistical thermodynamics derivation is demonstrated below to emphasize the physical significance of the configurational volume for an adsorbed molecule.

The Langmuir model distinguishes between molecules in an ideal gas phase to be mobile and adsorbed molecules on localized sites and referred to as the adsorbed phase hereinafter. The basic assumptions made for the adsorbed phase are [121]:

- i. Adsorbing molecules adsorb in an immobile state.
- ii. There are no interactions between adsorbate molecules on adjacent binding sites.
- iii. Each binding site is energetically equivalent and can accommodate only a single molecule.

The canonical partition function for the adsorbed phase (*ads*) where the adsorbent possesses N_S binding sites on which N_P molecules adsorb with an adsorption energy of $-N_P \mathcal{E}_{ads}$ is given by [120, 122, 123]

$$\mathcal{Z}_{ads} = \zeta^{N_P} \cdot e^{-\beta(-N_P \mathcal{E}_{ads})} \cdot \frac{N_S!}{N_P! \{N_S - N_P\}!}. \quad (3.36)$$

ζ specifies the partition sum of a single molecule in the bound state while the last term describes the degeneracy and represents the combinatorial ways to arrange N_P indistinguishable molecules on N_S binding sites [120]. Accordingly, the Helmholtz free energy for the adsorbed phase is

$$\beta \mathcal{F}_{ads} = -\ln \left[\zeta^{N_P} \cdot e^{\beta N_P \mathcal{E}_{ads}} \cdot \frac{N_S!}{N_P! \{N_S - N_P\}!} \right], \quad (3.37)$$

and by applying Stirling's formula for large factorials [120], that is,

$$\ln[n!] \approx n \ln[x] - n$$

gives

$$\beta \mathcal{F}_{ads} = - \left\{ N_P \ln \left[\frac{\nu_0}{\Lambda^3} \right] + \beta N_P \mathcal{E}_{ads} + N_S \ln[N_S] - N_P \ln[N_P] - \{N_S - N_P\} \ln[N_S - N_P] \right\}, \quad (3.38)$$

where ζ is substituted by $\frac{\nu_0}{\Lambda^3}$ with ν_0 being the *standard volume* which describes the effective configurational volume in a single binding site. The effective constant ν_0 includes also restrictions on vibrational and orientational degrees of freedom in addition to translational constraints. The Helmholtz free energy of the remaining molecules in the ideal gas phase (*gas*) is given by [90]

$$\beta \mathcal{F}_{gas} = \{N_T - N_P\} \left\{ \ln \left[\frac{N_T - N_P}{V} \Lambda^3 \right] - 1 \right\}, \quad (3.39)$$

with N_T being the total number of the molecules in the volume V . In thermodynamic equilibrium, the chemical potentials of the ideal gas phase and the adsorbed phase are equal [123]

$$\mu_{ads} = \mu_{gas}. \quad (3.40)$$

The chemical potentials for the different phases are obtained from Eqs. (3.38) and (3.39) by differentiating the Helmholtz free energy with respect to the adsorbed molecules N_P . Equalization yields

$$-\beta \mathcal{E}_{ads} - \ln \left[\frac{\Theta}{\{1 - \Theta\} \frac{\nu_0}{\Lambda^3}} \right] = -\ln[\Lambda^3 \cdot c_b], \quad (3.41)$$

where $\Theta = \frac{N_P}{N_S}$ denotes the fraction of bound molecules and $c_b = \frac{N_T - N_P}{V}$ the unbound molecule concentration. If the pressure is constant, the adsorption energy \mathcal{E}_{ads} corresponds to the Gibbs free energy ΔG_0 of adsorption. Upon rearrangement

$$K = e^{-\beta \Delta G_0} \nu_0 = \frac{\Theta}{\{1 - \Theta\} c_b}, \quad (3.42)$$

is obtained with K being the equilibrium constant or sometimes referred to as the binding constant or affinity. Thus, the Gibbs binding free energy

$$\beta \Delta G_0 = -\ln \left[\frac{K}{\nu_0} \right], \quad (3.43)$$

depends on the exact nature of the standard volume ν_0 in the bound state and is typically not known, an often overlooked fact in literature [124]. While for quantitative estimates precise knowledge of its value is necessary, a standard volume $\nu_0 = 1 \text{ L/mol}$ is used in this thesis, which is reasonable for molecular binding where spatial fluctuations are on a nanometer

length scale.

3.5 Experimental methods

One subject of this thesis deals with the theoretical modeling of experimental data from protein adsorption experiments. For that reason, this section gives an overview of relevant experimental methods used by the experimenters to study protein adsorption.

3.5.1 Isothermal titration calorimetry

Isothermal titration calorimetry (ITC) provides a reliable method to characterize the binding interaction between molecules in biological and physicochemical systems. Thermodynamically related parameters of the binding process such as the heat of binding ΔH_{ITC} , stoichiometry N_P , binding constant K , Gibbs free energy ΔG_0 , and entropy changes ΔS can be determined directly in a single experiment.

An ITC apparatus consists of two identical and highly thermally conductive cells which are embedded in an adiabatic chamber [125]. One of the cells is used as a reference cell containing only the buffering agent while the other serves as the sample cell in which the absorbent is placed in the same buffer. Initially, the cells are heated with a constant power wherein sensitive thermocouple circuits detect the temperature differences in the cells and, if necessary, regulates the heating of the sample cell by a feedback mechanism, depending on the temperature in the reference cell. During the titration, precise concentrations of binding substances are injected through a syringe into the sample cell. Depending on whether the associated reaction is exothermic or endothermic heat exchange takes place with the surroundings in the sample cell. Thereby, the time-dependent power supply of the heating mechanism of the sample cell is measured which is needed to maintain the same temperature as in the reference cell. The obtained experimental raw data show a series of spikes wherein each spike represents an injection process reflecting the induced temperature change and the re-setting of the temperature of the sample cell by the feedback coupler. The time integral of the spikes gives the heat Q that is released or absorbed during the titration.

Since binding events are accompanied by a heat exchange, the total heat is given by [125, 126]

$$Q(N) = \Delta H_{\text{ITC}} c_a V_{\text{tot}} N_P, \quad (3.44)$$

where c_a is the concentration of the absorbent in the solution and V_{tot} the total titration volume. Introducing the molar ratio $x = \frac{c_b^{\text{tot}}}{c_a}$ with c_b^{tot} being the total concentration of the binding substance yields

$$Q(x) = \Delta H_{\text{ITC}} c_a V_{\text{tot}} N_P(x). \quad (3.45)$$

It is convenient to fit the incremental heat $Q'(x) = \frac{\partial Q(x)}{\partial x}$ normalized to the molar concen-

tration of the binding substance

$$\frac{Q'(x)}{c^{tot}V_{tot}} = \frac{\Delta H_{ITC}N'_P(x)}{x}. \quad (3.46)$$

Experimental binding isotherms are usually often described with the Langmuir binding model, that is, Eq. (3.42). The concentration of the binding substance c_b in the Langmuir binding model can be expressed by the total concentration of the binding substance in the sample minus the bound concentration of the binding substance, by $c_b = c_b^{tot} - N_P\Theta c_a$. If it is assumed that ΔH_{ITC} , N_P , and K are concentration independent, solving Eq. (3.42) for Θ gives the total heat

$$Q(x) = \frac{\Delta H_{ITC}c_aV_{tot}N_P}{2} \left\{ \chi - \sqrt{\chi^2 - \frac{4x}{N}} \right\} \quad \text{with} \quad \chi = 1 + \frac{x}{N_P} + \frac{1}{KN_Pc_a}. \quad (3.47)$$

The fitting of $\frac{Q'(x)}{c^{tot}V_{tot}}$ to the experimental data then yields the unknown constants ΔH_{ITC} , N_P , and K . Typically a sigmoidal-like curve is obtained for $Q'(x)$, where ΔH_{ITC} describes the plateau for the first injections (small x), N_P the inflection point, and K the sharpness of the transition at $x \simeq N_P$. For large binding constants K and small x , almost all of the molecules immediately get adsorbed and for large x , typically $N_P(x)$ saturates and $Q'(x) \propto N'_P(x) = 0$. Thus, fitting to Langmuir isotherms is most sensitive to intermediate values of the molar ratio x , in the pre-saturation regime, near the inflection point of $Q'(x)$.

3.5.2 Dynamic light scattering

A suitable method for particle size determination in (diluted) solutions is offered by dynamic light scattering (DLS) [127]. Light scattering experiments have the great advantage that they are carried out in or in some cases close to thermodynamic equilibrium [128]. Onsager's regression hypothesis [129]

“... the average regression of fluctuations will obey the same laws as the corresponding macroscopic irreversible processes”

allows to calculate, for instance, transport coefficients from equilibrium fluctuations.

In a conventional DLS instrument, a sample cuvette containing the suspended particles and the solvent molecules is illuminated by a laser light through a lens to focus directly the light beam to the cuvette center. The particles that cross the laser beam scatter the light in all spatial directions. The scattered light is then collimated through another lens and recorded by a photon detector which is positioned at a known angle α with respect to the laser beam. The thermally induced collisions between the particles and the solvent molecules cause Brownian motion. This movement leads to a Doppler shift of the scattered light and, therefore, to fluctuations of the scattered intensity over time. Thus, the scattered light may interfere constructively or destructively. The rate of the intensity fluctuations provide

knowledge about how fast the particles move in the solution and thus about their size. The intensity fluctuations of small particles are fast and slow for large particles.

Experimentally, a correlator device compares the detected intensity I of the scattering light at time t to intensities at different short time delays τ . In this manner, the normalized second order autocorrelation function of the scattered intensity can be determined by [130]

$$g^{(2)}(\tau) = \frac{\langle I(t)I(t+\tau) \rangle}{\langle I(t) \rangle^2}, \quad (3.48)$$

where the angle braces denotes averaging over t . The Siegert relation [127] connects the second order autocorrelation function with the first order autocorrelation function by

$$g^{(2)}(\tau) = 1 + \Upsilon [g^{(1)}(\tau)]^2. \quad (3.49)$$

Here, $0 < \Upsilon < 1$ is a constant and depends on the experimental setup. For monodisperse solutions and non-interacting particles, that is, for infinite dilute solutions, the first order autocorrelation function decay exponentially [131]

$$g^{(1)}(\tau) = e^{-\frac{q_w^2 \langle \Delta \mathbf{r}(\tau)^2 \rangle}{6}}, \quad (3.50)$$

where $\langle \Delta \mathbf{r}(\tau)^2 \rangle$ is the mean square displacement of the particles at τ and q_w the magnitude of the scattering wave vector as defined as

$$q_w = \frac{4\pi m_1}{\lambda_w} \sin \left[\frac{\alpha}{2} \right], \quad (3.51)$$

with λ_w being the wavelength of laser source, and m_1 is the refractive index of the sample. Particles that follow Brownian motion $\langle \Delta \mathbf{r}(\tau)^2 \rangle = 6D\tau$ [132] where D denotes the diffusion coefficient of the particle in the solution. Thus, the second order autocorrelation function reduces to

$$g^{(2)}(\tau) = 1 + \Upsilon \left[e^{-q_w^2 D \tau} \right]^2. \quad (3.52)$$

Using the Stokes-Einstein equation [132]

$$D = \frac{k_B T}{6\pi\eta_{vis}R}, \quad (3.53)$$

the radius R of the particle can then be obtained from the diffusion coefficient if the viscosity η_{vis} of the solution is known. Note, radii measured by DLS represents a hydrodynamic radius referring to a spherical and non-interacting particle.

3.5.3 Fluorescence spectroscopy

The determination of molecule concentrations in adsorbents is often carried out on the basis of fluorescence spectroscopy, especially in multi-component systems [21]. The fluorescence

process arises when a substance adsorbs photons and stimulates electrons to a higher energy state. The excited energy state is unstable why electrons return to their ground state after a transient time. As a result, energy is emitted in form of photons but at slightly longer wavelengths than the excitation light. Because of this minimal difference the fluorescent light is outshined by the light source and can be isolated by filters in the beam path. An essential quality characteristic of fluorescence is the quantum yield, which describes the ratio of emitted and adsorbed photons. Any substance that can fluoresce is referred to as fluorophore or fluorescent dye and is designed to respond to specific stimulus. A fluorophore can be a part of a big molecule or a discrete small molecule which have distinct excitation and emission spectra. According to the Beer-Lambert law, the fluorescence intensity is linearly proportional to the fluorophore concentration in the dilute regime while at high concentrations a non-linear behavior is present [133]. The latter effect is caused by the fact that upon increasing molecule concentration the probability increases simultaneously that excited molecules interact with each other or with solvent molecules and lose energy or even stops the fluorescence process [134]. This phenomenon is known as fluorescence quenching. For instance, the method of fluorescence quenching can also employed to investigate the exchange of fluorescein isothiocyanate (FITC) labeled molecules by absorbents in the presence of other unlabeled molecules (competitive adsorption) [21].

4 Theoretical description and prediction of protein adsorption onto charged core-shell microgels

The subject of this chapter is to introduce a novel binding model for protein-microgel associations. Thereby, experimental binding isotherms and volume transitions are analyzed in detail and compared to theoretical calculations. The competitive binding of a binary protein mixture onto microgels is predicted by the model and compared to recent experimental results.

4.1 Protein interactions with charged core-shell microgels

In this section, we present a simple and predictive theoretical approach to elucidate single and competitive protein adsorption onto oppositely charged core-shell microgels (CSM). Contrary to the Langmuir binding model, electrostatic cooperativity and osmotic ion effects are taken into account. The model can also be readily extended to a multi-component system of proteins. We further demonstrate that an extended version of the Langmuir binding model can be derived formally from a more general model based on certain assumptions.

4.1.1 General model considerations

The molecular modeling of proteins and CSM particles in aqueous solutions can be described on different levels of theoretical complexity. For our purposes, a minimal model for the CSM, protein, and the solvent is presented which covers their essential physical properties.

The charged core-shell microgel model

The core-shell microgel¹ is considered to be a perfect sphere with radius R_M including a solid core with radius R_{cr} as depicted in Figure 4.1. Hence, the resulting net volume of the CSM is given by $V_M = \frac{4\pi}{3} \{R_M^3 - R_{cr}^3\}$. The total number of charged monomers within the CSM is determined to $N_M \simeq 4.9 \cdot 10^5$ by potentiometric measurements. The network monomers are assumed to be homogeneously distributed inside the CSM as found by small-angle scattering [135]. The mean CSM charge density is expressed by $Z_M c_M = \frac{Z_M N_M}{V_M}$ with Z_M and c_M being the monomer charge valency and charged monomer concentration. Due to the fact that the experimental pH value of the solution is $\simeq 7.2$ and, therefore, much larger than the pK_a value of $\simeq 4.6$ of polyacrylic acid, we deal with weakly charged CSMs with a charge fraction

¹A detailed description of the synthetic procedure can be found in Section 4.2 or in reference [22].

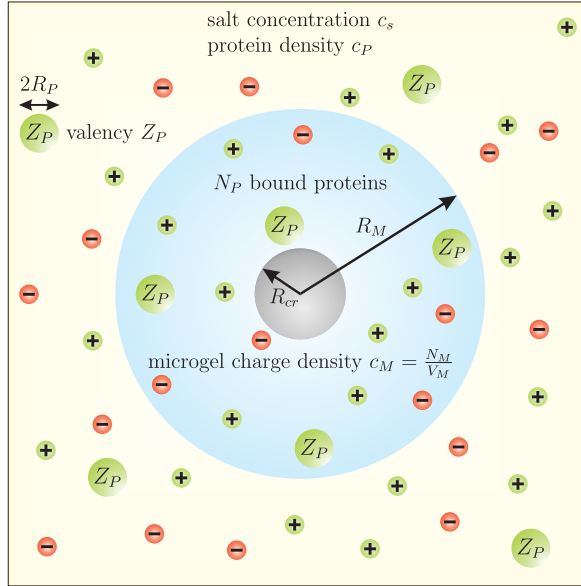


Figure 4.1: An illustrative sketch for one CSM particle in a solution containing proteins and salt ions with bulk concentrations c_P and c_s , respectively. The microgel is modeled as a sphere with radius R_M including a hard core with radius R_{cr} . The mean charge density of the CSM is $c_M = \frac{N_M}{V_M}$, where N_M denotes the number of charged monomers and V_M is the CSM's net volume. The proteins have radius R_P and valency Z_P while the salt ions are monovalent. N_P denotes the number of bound proteins inside the CSM.

of approximately $\frac{1}{10}$. We can therefore assume with reasonable certainty that $Z_M = -1$ in the following. The salt ions are monovalent with bulk concentrations $c_+ = c_- = c_s$, where the indices $+$ and $-$ refer to the cations and anions, respectively. The Bjerrum length λ_B of the system is 7.1 \AA , while the electrostatic Debye-Hückel screening length in the bulk region is on a nanometer scale for salt concentrations considered in the experiments. Moreover, we estimate a mean separation of about 2.2 nm between two charged monomers on the same polymer chain within the CSM, which is considerably larger than λ_B . Thus, charge regulation effects by counterion (Manning) condensation, release or inhomogeneity effects can be neglected [99, 136–138]. We further estimate the charged monomer concentration of the CSM to be $c_M \simeq 40 \text{ mM}$ to 100 mM , depending on the swelling state.

The protein and solvent model

The proteins are modeled as hard spheres with an effective diameter $\sigma_P = 2R_P$ having a monopolar moment of charge valency Z_P . Higher-order multipole contributions or effects arising from charged patches are neglected. No dispersion or other attractive non-electrostatic interactions between the proteins are considered. The proteins in the bulk region have a concentration of c_P , while the proteins inside the CSM are assumed to be homogeneously distributed [22]. Protein aggregation within the CSM is unlikely as at full load the system is still below the solubility threshold of a bulk system at comparable pH and electrolyte concentration [139]. The number of bound proteins inside the CSM is denoted by N_P giving rise to an internal protein packing fraction of $\eta = \frac{N_P \pi \sigma_P^3}{6V_M}$. Finally, the aqueous buffer and the CSM are modeled as a continuum background with dielectric, elastic, and osmotic properties as detailed in the following sections.

4.1.2 Electrostatics between proteins and CSM particles

The existence of electric charges in soft materials inevitably leads to long-range electrostatic interactions and ultimately affects the stability (or instability) of the systems. It is therefore crucial to take electrostatic effects into account for modeling protein adsorption on CSM particles. Thus, we make use of the Poisson-Boltzmann cell model to determine electrostatics of protein-CSM associations. While numerical solutions have often been employed [137, 140–147], for weak perturbations the linearized form can be treated analytically [37, 148].

The CSM with the volume V_M is partitioned into N_P spherical cells of radius R_c with volume V_c that satisfies

$$R_c = \sqrt[3]{\frac{3V_c}{4\pi}} = \sqrt[3]{\frac{3V_M}{4\pi N_P}} \propto \frac{1}{\sqrt[3]{N_P}}. \quad (4.1)$$

Each cell contains a protein and is in contact with a salt reservoir of concentration c_s . Since the CSM is a cross-linked network of polymers, a fixed number of charged network monomers $N_m = \frac{N_M}{N_P}$ is also present in each cell. Thus, a mean charged monomer concentration of $c_M = \frac{N_m}{V_c} = \frac{N_M}{V_M}$ is found in one cell. The requirement of electroneutrality for each cell leads to

$$c_s e^{-\Phi_D(y)} - c_s e^{\Phi_D(y)} + \frac{Z_M N_M + Z_P N_P}{V_M} = 0, \quad (4.2)$$

where we neglected the infinitesimally small protein concentration outside of the microgel. For high protein load, R_c becomes comparable to R_P and the cell volume needs to be corrected by the protein volume in principle. However, for our systems at highest protein load $\left(\frac{R_P}{R_c}\right)^3 \lesssim 0.1$, the correction is negligible for small and intermediate protein loads. As we will see in Section 4.3.1, the CSM volume V_M itself depends on the salt concentration c_s or on the protein load, that is, the molar ratio x which is why y depends on x . For the sake of clarity, we define $\Phi_D \equiv \Phi_D(y(x))$ hereinafter to consider this effect. The solution of Eq. (4.2) is the modified Donnan potential Φ_D and reads

$$\Phi_D = \ln \left[y + \sqrt{y^2 + 1} \right] \quad \text{with} \quad y = \frac{Z_M N_M + Z_P N_P}{2V_M c_s}. \quad (4.3)$$

The modified Donnan potential describes the difference in the mean electrostatic potential with respect to the bulk reference state where we set $\phi = 0$. As the protein concentration in the bulk is typically vanishingly small, electroneutrality dictates $c_+ = c_- = c_s$ to a very good approximation.

Focusing on proteins inside the CSM we assume that the cross-linked network of the CSM is flexible and fluid-like and the N_m charged monomers behave like mobile counterions to the protein. The PB equation in spherical coordinates is then

$$\frac{1}{r} \frac{\partial^2}{\partial r^2} (r \Phi(r)) = -4\pi \lambda_B \left\{ Z_M c_m e^{-Z_m \Phi_1(r)} - c_s e^{\Phi_1(r) + \Phi_D} + c_s e^{-\Phi_1(r) - \Phi_D} \right\}. \quad (4.4)$$

Here, the total electrostatic potential $\Phi(r) = \Phi_1(r) + \Phi_D$ consists of the constant mean

Donnan potential Φ_D and a perturbation $\Phi_1(r)$ induced by the protein. If the network monomers are assumed to be just a fixed, homogeneous background, they would not couple to the field and $c_m e^{-Z_M \Phi_1(r)}$ would need to be replaced by the fixed concentration c_M . The constant c_m is defined by conservation of the number of monomer charges in the cell via

$$N_m = c_m \int_{V_c} e^{-Z_M \Phi_1(r)} d^3r. \quad (4.5)$$

Moreover, it holds that the average potential equals the Donnan potential

$$\Phi_D = \frac{1}{V_c} \int_{V_c} \Phi(r) d^3r. \quad (4.6)$$

When the electrostatic potential $\Phi(r)$ is on the order of unity, we can linearize the exponentials in Eq. (4.4) with respect to $\Phi_1(r)$ to obtain a simplified analytical expression for the linearized PB (LPB) equation

$$\frac{1}{r} \frac{\partial^2}{\partial r^2} (r \Phi(r)) = 4\pi \lambda_B \frac{Z_P N_P}{V_M} + \kappa_{in}^2 \{ \Phi(r) - \Phi_D \}. \quad (4.7)$$

Here, we have identified the internal (CSM) charge density

$$- \frac{Z_P N_P}{V_M} = Z_M c_M + c_s e^{-\Phi_D} - c_s e^{\Phi_D} \quad (4.8)$$

from conditions (4.5) and (4.6) and $\kappa_{in} = \sqrt{4\pi \lambda_B c_{in}}$, the internal inverse screening length with $c_{in} = c_s e^{-\Phi_D} + c_s e^{\Phi_D} + c_M$ being the internal concentration. The LPB equation can be solved with the boundary conditions

$$\left. \frac{\partial \Phi'(r)}{\partial r} \right|_{r=R_P} = \frac{Z_P \lambda_B}{R_P^2}, \quad (4.9)$$

$$\left. \frac{\partial \Phi'(r)}{\partial r} \right|_{r=R_c} = 0. \quad (4.10)$$

The first boundary condition (4.9) states that the electric field on the protein surface is determined by its charge and size, while the second boundary condition (4.10) ensures a vanishing electric field at the outer boundary of the cell. The general solution for the total electrostatic potential $\Phi(r)$ takes the form (see also references [37, 148])

$$\begin{aligned} \Phi(r) &= \Phi_D + \Phi_1(r) \\ &= \Phi_D - \frac{Z_P N_P}{V_M c_{in}} + C_1 \frac{e^{-\kappa_{in} r}}{r} + C_2 \frac{e^{\kappa_{in} r}}{r}, \end{aligned} \quad (4.11)$$

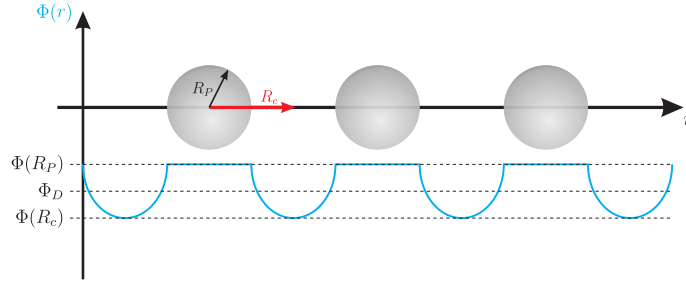


Figure 4.2: A schematic sketch of the total electrostatic potential $\Phi(r)$ in the PB cell model. The proteins (gray spheres) with a monopolar moment Z_P and radius R_P are placed in the cell center of radius R_c . The potential on the protein surface is given by $\Phi(R_P)$ while $\Phi(R_c)$ is the potential at the cell boundary. Φ_D is the mean Donnan potential.

in which for the constants C_1 and C_2

$$C_1 = \frac{Z_P \lambda_B e^{\kappa_{in} R_P}}{1 + \kappa_{in} R_P} \left\{ 1 - e^{-2\kappa_{in}(R_c - R_P)} \frac{\{\kappa_{in} R_P - 1\} \{\kappa_{in} R_c - 1\}}{\{\kappa_{in} R_P + 1\} \{\kappa_{in} R_c + 1\}} \right\}^{-1}, \quad (4.12)$$

$$C_2 = \frac{Z_P \lambda_B}{1 + \kappa_{in} R_P} \left\{ e^{\kappa_{in}(2R_c - R_P)} \frac{\{\kappa_{in} R_c - 1\}}{\{\kappa_{in} R_c + 1\}} - e^{\kappa_{in} R_P} \frac{\{\kappa_{in} R_P - 1\}}{\{\kappa_{in} R_P + 1\}} \right\}^{-1}, \quad (4.13)$$

are obtained. In the limit of large cell sizes ($R_c \rightarrow \infty$ or $N_P \rightarrow 0$) it follows that $C_2 \rightarrow 0$ and $C_1 \rightarrow \frac{Z_P \lambda_B e^{\kappa_{in} R_P}}{1 + \kappa_{in} R_P}$. Hence, the LPB solution simplifies to

$$\Phi(r) = \Phi_D - \frac{Z_P N_P}{V_M c_{in}} + \frac{Z_P \lambda_B}{1 + \kappa_{in} R_P} \frac{e^{-\kappa_{in}(r - R_P)}}{r}. \quad (4.14)$$

A sketch of the total electrostatic potential $\Phi(r)$ within the cell model is presented in Figure 4.2. Clearly, for a small protein load the potential at the cell boundary is $\Phi(R_c) \simeq \Phi_D - \frac{Z_P N_P}{V_M c_{in}}$ and on the protein surface is $\Phi(R_P) \simeq \Phi_D - \frac{Z_P N_P}{V_M c_{in}} + \frac{Z_P \lambda_B}{R_P \{1 + \kappa_{in} R_P\}}$, while Φ_D is the mean Donnan potential. For moderately high salt concentrations $c_s \lesssim c_M$, it follows that $\Phi_D \gtrsim 1$, and the internal salt concentration can be well represented by $c_{in} \simeq 2c_M$, as the coion concentration ($\propto e^{-|\Phi_D|}$) in the CSM becomes negligibly small. Analogously, for the dilute protein solution in the bulk region we find Eq. (3.11) to be valid.

4.1.3 Free energy of electrostatic transferring

The Gibbs free energy (or chemical potential) of transferring a protein with radius R_P and valency Z_P from bulk with salt concentration c_s and zero potential to a charged region within the CSM with a mean Donnan potential Φ_D and a monomer charge concentration c_M can be determined by the difference of work of charging the protein against the surface potential $\Phi(R_P)$

$$\beta \Delta G_{el} = \int_0^{Z_P} \left\{ \Phi(R_P) - \Phi_{DH}(R_P) \right\} dZ_P. \quad (4.15)$$

In the limiting case of low salt concentration and protein load, we obtain the leading order contributions

$$\beta\Delta G_{el} = Z_P\Phi_D - \frac{Z_P^2 N_P}{2c_M V_M} - \frac{Z_P^2 \lambda_B}{2R_P} \left\{ \frac{\kappa_M R_P}{1 + \kappa_M R_P} - \frac{\kappa R_P}{1 + \kappa R_P} \right\}. \quad (4.16)$$

We did not explicitly integrate over Z_P in the second term in Eq. (4.14) since it is a constant background contribution and, therefore, not immediately involved in the charging process of the particle. It is noteworthy that we obtain the same functional form for ΔG_{el} if the monomer charges are not assumed to be mobile, albeit with a $\sqrt{2}$ smaller internal inverse screening length $\sqrt{4\pi\lambda_B c_M}$ and a factor of 2 in front of the second term.

By a one-to-one comparison of the leading order expression in Eq. (4.16) to the result from employing the full expression of Eq. (4.7), we find that the error in ΔG_{el} is less than one $k_B T$ over the whole range of molar ratios and salt concentrations considered in this thesis or rather in the experiments. By detailed inspection of the behavior of (4.11) we observe that the reason of the accuracy is a fortuitous cancellation of errors of higher order terms at large N_P . This fact may shed some doubt on the general applicability of the simplified Eq. (4.16) but note that our parameters (protein valency, salt concentrations, monomer charge densities, etc.) are typical and accessible for a wide variety of experimental systems. However, in general the PB approach is expected to break down for very high protein valencies and small proteins, when $|\Phi_1| \gg 1$, and strong Coulomb correlations play a role [132].

The free energy in Eq. (4.16) considers only ionic contributions to solvation of a fixed lattice of proteins, that is, it neglects the electrostatic contributions from the interaction between the proteins, the energy penalty of overlapping double layers. However, in the fluid-like CSM protein matrix it is reasonable to assume that proteins can wiggle or move around and are not rigidly fixed to lattice positions. Due to such fluctuations the average surface potential will actually be higher than given in Eq. (4.14). In order to estimate the interaction contribution we look at the expansion of the excess chemical potential in terms of virial coefficients, *i.e.*, in first order

$$\beta\mu = \frac{2B_2}{V_c} \quad \text{with} \quad B_2 = -\frac{1}{2} \int \left\{ e^{-\beta W(r)} - 1 \right\} d^3r. \quad (4.17)$$

$W(r)$ is the potential that describes protein-protein interaction and consists of a hard-sphere component (hs) and a DH potential

$$W(r) = W_{hs} + \frac{Z_P^2 \lambda_B}{1 + \kappa R_P} \frac{e^{-\kappa(r-R_P)}}{r}. \quad (4.18)$$

By using the condition (4.6) and linearizing the exponent in the defining equation for B_2 yields in

$$\beta\mu = \beta\mu_{HS} + \frac{Z_P^2 N_P}{2c_M V_M}, \quad (4.19)$$

where the chemical potential is separated into a hard-sphere and an electrostatic part. Thus, in leading order the electrostatic protein-protein interaction contribution exactly cancels the second term in Eq. (4.16) and the final result for the electrostatic transfer free energy is obtained

$$\boxed{\beta\Delta G_{el} = Z_P\Phi_D - \frac{Z_P^2\lambda_B}{2R_P} \left\{ \frac{\kappa_M R_P}{1 + \kappa_M R_P} - \frac{\kappa R_P}{1 + \kappa R_P} \right\}}. \quad (4.20)$$

The first term in Eq. (4.20) is purely entropic and describes the electrostatic transfer energy of a protein with charge Z_P from a bulk solution at zero potential to a region at potential Φ_D . It is attractive if the CSM and protein have opposite net charges and otherwise repulsive. The second term in Eq. (4.20) expresses the difference in the Born solvation free energies in a medium of concentrations c_s and c_M [90]. If $c_M > c_s$ it has an attractive (otherwise repulsive) contribution to ΔG_{el} . The inhomogeneities that are introduced by the cell model assumption as depicted in Figure 4.2 cancel out in the linearized theory if protein fluctuations are allowed and the simple form of (4.20) holds then.

4.1.4 Osmotic and elastic deswelling

The interplay of osmotic and elastic forces defines the equilibrium size of the CSM. In more detail, the osmotic pressure causes the CSM to swell, while the elastic pressure counterbalance this expansion due to the configurational entropy of polymer chains. A thermodynamic equilibrium is achieved when the total pressure vanishes [33, 137, 149–152]

$$p = p_{osm} + p_{elas} = 0. \quad (4.21)$$

The osmotic term comprises contributions from the ions and the solvent. The latter is usually expressed by a de Gennes-like scaling law of type $\propto V_M^{-a}$. The exponent a characterizes the thermodynamic quality of mixing polymer and solvent. For good solvent conditions and neutral polymers a typically scales with $\frac{9}{4}$ [150, 153]. However, when considering charged polymers corrections have to be taken into account [151]. In the experiments, the exponent of $\frac{9}{4}$ is likely to remain valid since pNiPAm is a weakly charged polymer [150, 152, 154].

The ionic osmotic pressure is dominated by the ideal gas pressure of ions within the CSM as given by Eq. (3.14). This is counterbalanced by the elastic pressure p_{elas} . The elastic pressure is connected with the shear modulus G_M and scales with $\propto V_M^{-b}$ where $b = \frac{1}{3}$. This is also confirmed by various experiments [150, 152, 154–157]. Using the scaling concepts above, we find for the total pressure

$$\begin{aligned} p &= C_3 V_M^a + C_4 V_M^b + p_{ion} \\ &= C_3 V_M^a \left[1 - \left(\frac{V_M}{V_0} \right)^{a-b} \right] + p_{ion}, \end{aligned} \quad (4.22)$$

where C_3 and C_4 are volume-independent constants. V_0 is the equilibrium volume of the

CSM when the ionic pressure vanishes ($p_{ion} = 0$), *e.g.* at high salt concentrations. The bulk modulus K_M of the CSM in this state is defined by

$$\beta K_M(V_0) = -V_M \left. \frac{\partial \beta p}{\partial V_M} \right|_{T, V_0} = \frac{23}{12} \frac{C_3}{V_0^a}. \quad (4.23)$$

Equation (4.22) can be fitted to different salt concentrations (without proteins) to determine C_3 and V_0 and thereby the bulk modulus $K_M(V_0)$.

The estimation of the osmotic contribution in the presence of proteins is more complex. For instance, the net charge of the CSM will be reduced by the adsorbed proteins and simultaneously inhomogeneities will be induced due to the micro-configurations of the proteins. Although these phenomena can not be exactly described by Eq. (3.14), they can be approximated and incorporated in Eq. (4.22) in a naive form. In the cell model, the ionic pressure is determined by the ionic concentration at the cell boundary because the electrostatic pressure vanishes on the surface [37, 39, 140, 142, 148, 158]. Therefore, it holds

$$p_{ion}^P \simeq c_s e^{\Phi(R_c)} + c_s e^{-\Phi(R_c)} - 2c_s. \quad (4.24)$$

Linearizing of p_{ion}^P with respect to $\Phi_1(r)$ results in $2c_s \Phi_1(R_c) \sinh[\Phi_D]$ and p_{ion} in Eq. (4.22) can be replaced by p_{ion}^P

$$p_{ion}^P \simeq p_{ion} + 2c_s \Phi_1(R_c) \sinh[\Phi_D], \quad (4.25)$$

which recovers $p_{ion}^P \simeq p_{ion}$ in the limit for vanishing protein concentration. Note that this expression does not consider fluctuations of the protein positions, which is likely to be an important effect to consider in future studies. Estimation of other protein-induced contributions to the pressure from local effects on the elasticity, such as cross-linking by local binding [159], conformational restraints of the polymer network, or possible contributions from the protein osmotic pressure is challenging due to the lack of precise knowledge of the nature of the bound state and is out of scope of this thesis.

4.1.5 Cooperative binding model

The modeling of protein uptake into CSM has been done often by using the standard Langmuir isotherm [120, 122], in particular when evaluating protein adsorption as measured by ITC [22, 23, 25–27, 160]. In the standard Langmuir approach, protein association with single, independent binding sites is assumed. Electrostatic cooperativity effects and volume changes of the CSM during protein adsorption are neglected. Additionally, the term binding of proteins onto soft polymeric layers and microgels is not as clearly defined. The system may remain in a fluid-like state where proteins are still mobile on average, albeit slower than in bulk [17, 161]. Consequently, the stoichiometry and binding affinities to binding sites in the CSM obtained from Langmuir fitting are not so easy to interpret.

As a matter of fact, cooperativity effects arise due to the change of the net charge of the

CSM when proteins are adsorbed and thereby affects the overall electrostatics of the system. Such an effect has been appreciated in the Guoy-Chapman-Stern theory for the binding of charged ligands to charged surfaces [162–164]. As a consequence, the binding affinity K in the Langmuir binding model can not be regarded as a *real* constant. It is therefore more appropriate to express the binding affinity by a protein-specific intrinsic adsorption energy ΔG_0 and an electrostatic energy contribution dependent on the molar ratio x and thus on the protein load. In our cooperative binding (CB) model, the proteins adsorbed by the CSM are not condensed to fixed lattice positions. They are able to move freely under the constraint that their translational freedom is confined by packing. Therefore, we account for excluded volume interactions [30, 37, 39, 158] between proteins inside the CSM as well. Thus, saturation of the CSM takes place due to packing.

It is convenient to formulate the corresponding equations for multi-component mixtures, since the one-component case ($i = 1$) is a limiting case. We begin to write the Boltzmann-like equation for our model

$$\frac{N_{P,i}}{V_M} = \zeta_{P,i} c_{P,i} e^{-\beta(\Delta G_{0,i} + \Delta G_{el,i} + \mu_i)} \quad \text{with} \quad i \in \{1, \dots, \mathcal{M}\}. \quad (4.26)$$

\mathcal{M} is the set of considered proteins in the mixture. Equation (4.26) represents a system of \mathcal{M} nonlinear equations with \mathcal{M} unknowns. $\zeta_{P,i}$ is the partition function of the protein i in the bound state which may have orientational or vibrational constraints of the protein's degrees of freedom within the CSM, *e.g.* by partial sliding on the pNiPAm polymer chains [165]. $c_{P,i}$ is the concentration of the i th protein in bulk. At this point we have to have a closer look at the total binding energy $\Delta G_{tot} = \Delta G_{0,i} + \Delta G_{el,i} + \mu_i$ additionally:

- **Intrinsic free energy ΔG_0**

The intrinsic binding free energy $\Delta G_{0,i}$ for individual proteins contains salt-independent and specific local interactions such as hydrophobic effects or hydration forces. However, in the sense of weak intrinsic interactions so that proteins inside the CSM remain mobile. The intrinsic binding energy is determined by fitting experimental adsorption isotherms and thus represents a protein/CSM-specific number, which can be tabulated for further approaches or applications.

- **Electrostatic energy ΔG_{el}**

We assume that the electrostatic energy $\Delta G_{el,i}$ is well described by Eq. (4.20). Therefore, Eq. (4.20) is expanded to multi-components by

$$\beta \Delta G_{el,i} = Z_{P,i} \Phi_D - \frac{Z_{P,i}^2 \lambda_B}{2R_{P,i}} \left\{ \frac{\kappa_M R_{P,i}}{1 + \kappa_M R_{P,i}} - \frac{\kappa R_{P,i}}{1 + \kappa R_{P,i}} \right\} \quad (4.27)$$

with the expanded Donnan potential

$$\Phi_D = \ln[y + \sqrt{y^2 + 1}] \quad \text{with} \quad y = \frac{Z_M N_M + \sum_{i \in \mathcal{M}} Z_{P,i} N_{P,i}}{2V_M c_s}. \quad (4.28)$$

- **Excess chemical potential of hard-sphere packing μ**

μ_i describes the configurational chemical potential and for one-component systems it is given by the Carnahan-Starling potential [132]

$$\beta\mu_i = \frac{8\eta - 9\eta^2 + 3\eta^3}{\{1 - \eta\}^3}. \quad (4.29)$$

The generalization to multi-component² systems is not analytically easy to achieve [166]. However, in the low density limit as considered here, that is, for small protein packing, μ_i can be expressed in terms of the second virial coefficient B_2^{ij}

$$\beta\mu_i = 2 \sum_{j \in \mathcal{M}} \frac{B_2^{ij} N_j}{V_M}. \quad (4.30)$$

This expression can comprise mixtures with an arbitrary number of components. Since the salinity within the CSM network is quite high, the proteins are modeled as additive hard spheres, disregarding their electrostatic repulsion. Hence, the corresponding second virial coefficient for two interacting proteins i and j is given by

$$B_2^{ij} = \frac{2\pi}{3} \left\{ \frac{\sigma_i + \sigma_j}{2} \right\}^3. \quad (4.31)$$

B_2 can be measured directly in solution by scattering experiments or it can be calculated from structural data [167]. The excluded volume of the CSM network monomers are also considered in our model. We have estimated approximately $3.7 \cdot 10^6$ pNiPAm monomers in one CSM particle and determined an excluded volume of $V_{ex} \simeq 1.1 \cdot 10^6 \text{ nm}^3$, while one pNiPAm monomer has an excluded volume of roughly 0.3 nm^3 . Thus, the pNiPAm volume fraction is between 5% for a unloaded CSM and 12% for the fully loaded CSM at 7 mM salt.

Recall that the free energy contributions $\beta\Delta G_{el,i}$ and $\beta\mu_i$ depend on the CSM volume V_M and thus on x wherefore βG_{tot} is a function of the molar ratio x .

Equivalence between the CB model and an extended version of the Langmuir binding model

Here, we demonstrate that an extended version of the Langmuir binding model can also be derived from our CB model. Considering a one-component system with low protein packing

²It should be noted that an analytical expression for the special case of a binary mixture is well-known, see reference [166].

fractions $\eta \ll 1$, the chemical potential μ_i in Eq. (4.29) may be linearized with respect to η and yields

$$\frac{N_P}{V_M} \simeq \zeta_P c_P e^{-\beta(\Delta G_0 + \Delta G_{el})} \left\{ 1 - \frac{2B_2 N_P}{V_M} \right\}, \quad (4.32)$$

where we have identified the second virial coefficient of hard spheres $B_2 = \frac{2\pi\sigma_P^3}{3}$. Roughly speaking, B_2 physically describes the volume excluded to the centers of the other proteins taken by one protein. By rearranging Eq. (4.32), we get

$$\zeta_P e^{-\beta(\Delta G_0 + \Delta G_{el})} = \frac{N_P}{V_M} \left\{ \left\{ 1 - \frac{2B_2 N_P}{V_M} \right\} c_P \right\}^{-1}. \quad (4.33)$$

By substituting $N_S = \frac{V_M}{2B_2}$ and $\Theta = \frac{N_P}{N_S}$ we obtain an expression for an extended version of the Langmuir binding model of the form (3.42)

$$2B_2 \zeta_P e^{-\beta(\Delta G_0 + \Delta G_{el})} = \frac{\Theta}{\{1 - \Theta\} c_P}. \quad (4.34)$$

Thus, the CB model gives a more general description of the standard Langmuir model if $2B_2 = \nu_0$ and $\zeta_P = 1$. That means, that in the low density limit a bound protein has a configurational freedom (volume) of $2B_2$. However, as discussed above, in the Langmuir-type bound state, the configurations are restricted to an effective configurational volume ν_0 with respect to $2B_2$, such that the partition function $\zeta = \frac{\nu_0}{2B_2}$. Using this definition, we obtain an extended Langmuir binding model (see Section 3.4). Thus, in the approximation of small protein packing $\eta \ll 1$, the CB model and an extension of the Langmuir binding model are formally equivalent and are allowed to be compared. The number of fixed binding sites N_S can then be interpreted as the maximum number of binding sites available for proteins simply due to packing in the available volume V_M .

4.1.6 Numerical evaluation including volume change

In the Langmuir approach the incremental heat $Q'(x)$ in Eq. (3.46) is fitted to the experimental data by scanning through the fit parameters ΔH_{ITC} , K , and N_P until the least square deviation (LSD) to the experimental data is minimized. In the CB model, Eq. (4.26) is solved numerically with respect to N_P by means of a Newton-Raphson³ method and $Q'(x)$ is fitted to the ITC data by minimizing the LSD. Here, the fitting parameters are ΔH_{ITC} and ΔG_0 since all other parameters or inputs are either known from the experiments or in case of the protein radius R_P and net charge Z_P known from literature (see also Table 4.3 in Section 4.3.2 for more details).

One challenge arises because the CSM volume is a function of the molar ratio x . A predictive theory for V_M is out of scope of this thesis. Therefore, we satisfy ourselves by employing experimental DLS data for $R_M(c_s)$ and $R_M(x)$ for one-component protein solutions. We fit

³A more detailed description of the method is given in Appendix A

$V_M(x) = \frac{4\pi}{3} \{R_M(x)^3 - R_{cr}^3\}$ by the empirical function

$$R_M(x) = \frac{R_{\max} - R_{\min}}{2} \left\{ 1 - \tanh \left[\frac{x - x_0}{\Delta} \right] \right\} + R_{\min}, \quad (4.35)$$

with R_{\max} and R_{\min} being the maximum and minimum CSM radius at $x = 0$ and $x \rightarrow \infty$, respectively. The fit parameter x_0 is the location of the inflection point, and Δ the distribution width. In multi-component systems the CSM volume depends on the numbers of bound proteins of the different proteins since adsorption is competitive in this case. This complex change in the CSM volume can also be measured using DLS. However, due to absence of such experimental data we interpolate the volume change based upon one-component DLS data by

$$V_M(N_{P_i}, N_{P_j}) = \frac{V_M(N_{P_i}) \cdot N_{P_i} + V_M(N_{P_j}) \cdot N_{P_j}}{N_{P_i} + N_{P_j}}. \quad (4.36)$$

The indices i and j on N_P point to two different proteins in the solution. From our numerical routine, we can assign calculated values of $N_P(x)$ and $R_M(x)$ to each x so that $V_M(N_{P_1}, N_{P_2})$ is well-defined without further parameters.

4.2 Experimental materials

Proteins

Four cationic proteins were selected for experiments in order to investigate single and competitive protein adsorption onto an oppositely charged core-shell microgel. The proteins lysozyme from *chicken egg white*, cytochrome c from *bovine heart*, papain from *papaya latex*, and ribonuclease A (RNase A) from *bovine pancreas* were purchased from Sigma-Aldrich and dialyzed against the buffer used for the experimental conditions.

Preparation of the charged core-shell microgel

The same batch of the CSM dispersion was used as in the experiments of Welsch *et al.* [22]. In brief, the polystyrene core was synthesized by emulsion polymerization in the first step. After purification of the core particles, the microgel shell, containing 5 mol-% N,N-methylenebisacrylamide (BIS) cross-linkers and 10 mol-% acrylic acid with respect to the amount of pNi-PAm, was polymerized on the polystyrene core by seed polymerization. After purification, the particles were transferred into buffer solution by ultrafiltration against 10 mM MOPS buffer at pH 7.2. In this preparation state, the microgel is swollen and strongly hydrated with more than 90% volume fraction of water. DLS experiments (Malvern Instruments) were applied to determine the hydrodynamic radius of the polystyrene core to $R_{cr} \simeq 62$ nm and the radius of the total CSM to $R_M \simeq 129 - 180$ nm depending on solution conditions [22].

ITC measurements

As in the studies of Welsch *et al.*, single protein adsorption isotherms were obtained by ITC [22]. The experiments were performed using a VP-ITC instrument (Microcal) with a fixed cell volume of 1.4 mL, which was filled with the microgel dispersion at $c_M \simeq 8.42 \cdot 10^{-7}$ mM. A buffer-matched protein solution of roughly 280 μ L was titrated stepwise into the sample cell and the incremental heat change $Q'(x)$ after each injection was measured. Afterwards the same protein solution was titrated into the pure buffer system to account for the dilution heat. The following three buffer systems were used:

- i. 10 mM MOPS, 2 mM NaN_3 (7 mM ionic strength),
- ii. as i. with additional 10 mM NaCl (17 mM ionic strength),
- iii. as i. with additional 25 mM NaCl (32 mM ionic strength).

The experiments were performed at 298 K and the pH-value was held constant at $\text{pH} \simeq 7.2$.

Fluorescence spectroscopy experiments

Competitive protein adsorption was studied using fluorescence spectroscopy. Fluorescein isothiocyanate (FITC) was purchased from Fluka and used for labeling lysozyme. FITC displays sensitivity to pH changes and possesses a high extinction coefficient and a quantum yield (~ 0.92) [168]. The fluorescence spectra were recorded with a Fluoro-Max-3 spectrometer (JY-Horiba) at a slit width of 1.5 nm and an optical path length of 1 cm. For competitive adsorption experiments an optical quartz cell was filled with 1.64 μ M lysozyme^{FITC} solution and $2.4 \cdot 10^{-5}$ μ M of buffer-matched microgel suspension was added afterwards. This corresponds to a load of the microgel by lysozyme^{FITC} of roughly 60%. Quenching effects of FITC lead to a decreased fluorescence when lysozyme^{FITC} penetrates the microgel network. The fluorophore fluorescence peak was monitored at 518 nm. Increasing amounts of the competing protein were injected step by step to the microgel solution loaded previously with lysozyme^{FITC}. After each injection step the system was equilibrated for five minutes under stirring at 298 K previous to the measurement of the fluorescence intensity. The quenching effect was used to quantify the concentration of non-adsorbed protein using a calibration line (intensity vs. protein concentration). The amount of adsorbed proteins is the difference between the total protein concentration and the concentration of non-adsorbed proteins in equilibrium which contribute to the remaining intensity.

It has to be noted that all DLS, ITC, and fluorescence spectroscopy experiments on protein adsorption described above, whether single or competitive, were performed by Dr. Nicole Welsch, Michael Oberle, and Qidi Ran in the Institute for Functional Materials at Helmholtz-Zentrum Berlin. Their experimental data sets will be described by the theoretical models named previously.

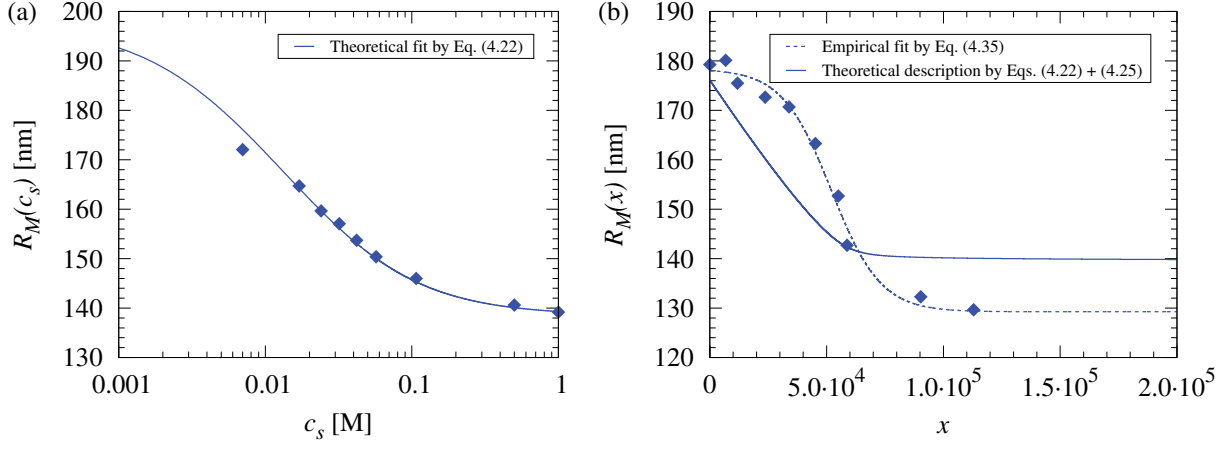


Figure 4.3: Hydrodynamic radii of the CSM particles at $T = 298$ K. The experimental data (filled diamonds) are obtained from DLS measurements. (a) CSM radius $R_M(c_s)$ as a function of the salt concentration c_s in the bulk (without proteins). The blue solid line is a theoretical fit according to Eq. (4.22). (b) CSM radius $R_M(x)$ versus the molar ratio $x = c_P^{\text{tot}}/c_M$ of lysozyme at 7 mM ionic strength. The blue dashed line depicts a simple empirical fit according to Eq. (4.35) used as input for the fitting of ITC binding isotherms. The blue solid line is a theoretical prediction from Eqs. (4.22) and (4.25) based on electrostatic considerations only.

4.3 Experimental and theoretical results of one-component binding

The aim of this section is the comparison of results from protein adsorption experiments to our theoretical model as introduced in the previous section. In the first part, we focus on the swelling state of the CSM. Here, we describe theoretically the hydrodynamic radius change of the CSM depending on the bulk salt concentration and on protein load. Afterwards, an in-depth investigation of experimental bindings isotherms by the Langmuir and CB model is performed. This analysis enables a more accurate separation between specific and electrostatic interactions of proteins with CSM particles. Finally, we perform an interpretation of the applied Langmuir and CB models.

4.3.1 CSM deswelling by salt and proteins

As confirmed by previous experimental observations [14, 24, 30], DLS measurements depict a deswelling of the CSM upon the systematic addition of salt up to a concentration of $c_s = 1$ M. The experimental data together with the result of Eq. (4.22) (solid line) are shown in Figure 4.3 (a). The CSM radius decreases monotonically and saturates at $c_s = 1$ M to $R_M \simeq 139$ nm. The best fit of our mechanical balance approach yields a very good agreement in almost the whole range of c_s . From the fit we obtain $R_0 \simeq 138.5$ nm in the limit of $c_s \rightarrow \infty$ and thus a bulk modulus of $K_M(V_0) = 204$ kPa. Assuming Poisson's ratio to be $\frac{1}{3}$ valid for neutral polyacrylamide or pNiPAm microgels [169, 170], then Young's modulus $E \simeq K_M$. The determined value for K_M is thus fully consistent with recently measured Young moduli investigated for varying BIS cross linker density at similar temperatures [171]. In the latter

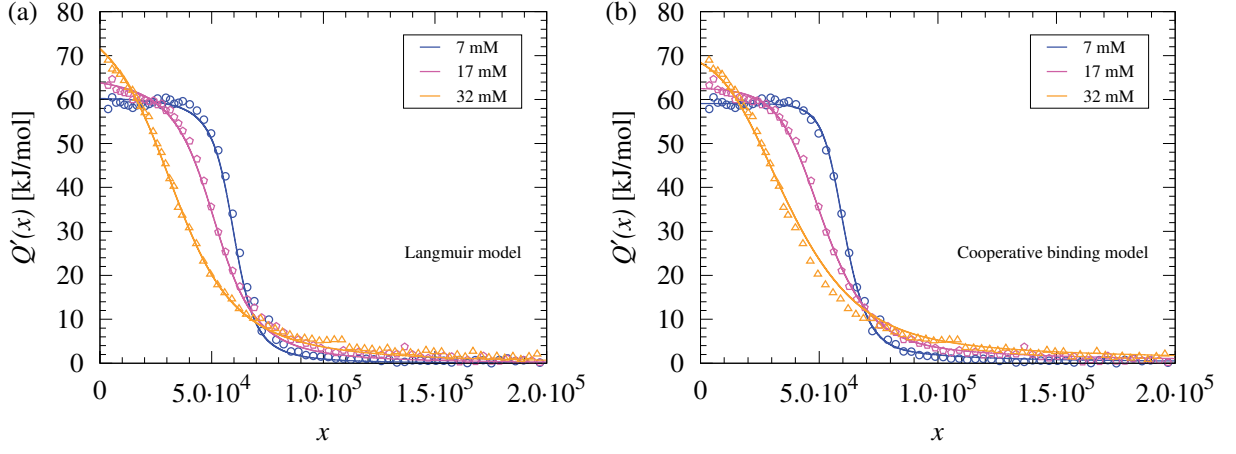


Figure 4.4: Experimental binding isotherms (symbols) measured by ITC for lysozyme at different salt concentrations at $T = 298$ K. The solid lines are results from fitting to (a) the Langmuir binding model and (b) the CB model. See Table 4.1 and 4.2 for the obtained fitting parameters.

E was measured between 80 kPa and 500 kPa for BIS contents of 2% and 10%, respectively, compared to 5% in this thesis. This good agreement confirm our considerations leading to Eq. (4.22).

The DLS measurement of the CSM radii depending on the molar ratio x of lysozyme at 7 mM salt concentration is shown in Figure 4.3 (b). Analogously to the salt-only case, deswelling of the CSM is now observed with increasing protein load. In the saturation regime, that is at $x \simeq 1.1 \cdot 10^5$, the CSM radius is notably smaller than R_0 pointing to binding-related network tightening. By fitting the DLS data to the empirical fit Eq. (4.35), we find $R_{\max} \simeq 172$ nm, $R_{\min} \simeq 129$ nm, $\Delta \simeq 24000$; x_0 can be identified with the number of binding sites N_P . Thus, the CSM volume in a fully loaded state is $\frac{V_0}{V_{\min}} \simeq 1.3$ times smaller than in the neutral reference state. If we assume that the charged proteins under full load lead to complete charge neutralization and, therefore, $p_{ion} \simeq 0$, then the bulk modulus K_M induced by protein binding scales $\propto \left(\frac{V_0}{V_{\min}}\right)^{9/4}$ and is approximately 1.7 times larger than without proteins. Hence, the CSM is roughly two times stiffer due to protein adsorption. This has to be considered as a lower bound as it is likely that ionic contributions to the osmotic pressure still play a role, and may be protein osmotic effects due to excluded volume interactions need to be considered.

However, in order to check to which amount purely electrostatic effects by proteins induce CSM deswelling, we plot the description by Eqs. (4.22) and (4.25) also in Figure 4.3 (b) using the experimental ITC binding isotherm $N_P(x)$ as input. This description is now a prediction without any adjustable variables. While the overall shrinking of the CSM is reasonably captured, the model yields a too fast decrease for small x . This may point to shortcomings of the mean-field cell model (see Section 4.1.2) since ion and protein fluctuations are not included. For large x , the experimental saturation of $R_{\min} \simeq 129$ nm is not reached, indicating that non-electrostatic effects to the CSM elasticity play a role. Similar unsatisfying performances of simple Donnan models have been observed also in a recent work [30]. However, from our comparison it is quite reasonable to judge that the dominant effect to CSM deswelling by

Table 4.1: Thermodynamic parameters determined from fitting the ITC data to the standard Langmuir model at $T = 298$ K. A lower LSD value corresponds to a better fit quality.

c_s [mM]	ΔH_{ITC} [kJ/mol]	N	K [L/mol]	ΔG_0 [k _B T]	LSD
7	60.7	60100	$2.62 \cdot 10^6$	-14.8	123
17	66.1	52800	$6.25 \cdot 10^5$	-13.4	82
32	83.8	37600	$1.85 \cdot 10^5$	-12.2	62

protein uptake originates from osmotic pressure caused by the ions.

4.3.2 Characterizing experimental binding isotherms

The protein lysozyme was object of many different protein adsorption studies since it is stable and very well characterized [172, 173]. For this reason, lysozyme appears to be a suitable choice, which was also selected by the experimenters to investigate in detail the adsorbing process on the CSM. In the following paragraphs, we first compare the experimental binding isotherms of lysozyme at different salt concentrations to the Langmuir and CB model, while the adsorption behavior of the other proteins to the CSM are discussed afterwards.

Langmuir model

The evaluation of the ITC data by the standard Langmuir binding model at 7 mM, 17 mM, and 32 mM ionic strength is presented in Figure 4.4 (a). As mentioned before, the Langmuir binding model is very sensitive in the pre-saturation region. The resulting fitting parameters are summarized in Table 4.1. From looking at the fits by eye and judging from the overall least square deviation (LSD) to the ITC data (*cf.* Table 4.1), all fits look comparably well. Here, we observe that the number of Langmuir binding sites N_S decreases with increasing ionic strength. The reason is *a priori* unclear as the Langmuir model assumes a fixed number of binding sites independent of ionic strength. We further notice that the heat of adsorption ΔH_{ITC} slightly increases with ionic strength. More importantly, K or rather ΔG_0 stays fairly independent of c_s .

Cooperative binding model

The fitting of the same ITC data set by the CB model including the volume change of the CSM is presented in Figure 4.4 (b). The corresponding fitting parameters are listed in Table 4.2. Note again that the initial CSM volume at $x = 0$ decreases for increasing ionic strengths (see Figure 4.3 (a)). For the data set measured at 17 mM and 32 mM ionic strength no DLS data were available. Thus, V_M is obtained by using the known R_{max} from Figure 4.3 (a) and $x_0 = N_P$, while $R_{\text{min}} = 129$ nm is used from the 7 mM fit. The only free variable Δ is employed as an additional fit parameter obtained by least square fitting to ITC data. We find that Δ appears to be correlated with the change of the sharpness of the binding isotherms N_P with c_s .

Table 4.2: Results of fitting the same ITC data set to the CB model with $R_P = 1.9$ nm and $Z_P = +7$ e at $T = 298$ K. The change of the CSM volume was considered in the fit according to Eq. (4.35).

c_s [mM]	ΔH_{ITC} [kJ/mol]	ΔG_0 [k _B T]	LSD
7	59.1	-6.3	46
17	62.1	-6.7	38
32	70.1	-6.5	153

Like for the Langmuir binding model, the binding isotherms are described excellent with the CB model according the LSD to the experimental data. The resulting values for the heat ΔH_{ITC} are also consistent with the Langmuir fits except for the 32 mM data set. This is not surprising, as this value is determined by the plateau in $Q'(x)$ for small x , far away from the saturation regime. For that reason, $\Delta H_{\text{ITC}} = 70.1 \frac{\text{kJ}}{\text{mol}}$ for the 32 mM data set is more reasonable instead of $83.8 \frac{\text{kJ}}{\text{mol}}$ obtained from the Langmuir binding model. The fitting parameter N_P is now directly calculated in the CB model, depending on the packing fraction η and thus on R_P , the effective hard core radius of the protein. The agreement is remarkable and justifies the assumptions leading to the CB model, *i.e.*, the packing picture of globular proteins. A very small salt dependency of ΔG_0 remains, indicating a slightly inaccurate subtraction of the nonspecific effects in this model. However, the salt concentration dependency is low and on average we find $\Delta G_0 \simeq -6.5$ k_BT. This value might be attributed to hydrophobic interactions or possibly other local binding effects. We also note that the effective net charge of chicken egg white lysozyme as used in this experiments may be slightly larger on average due to protonation effects within the CSM [22]. However, using $Z_P = +7.5$ e or $+8$ e for lysozyme in our analysis we end up with a similar $\Delta G_0 \simeq -6.5$ k_BT. The reason is that while the prefactor in the electrostatic contribution (4.20) rises, the Donnan potential (4.3) decreases quicker with load. These effects roughly cancel each other for our particular system.

A conspicuous point is the difference in the magnitude of the intrinsic adsorption energy ΔG_0 in both models. At 7 mM ionic strength, we obtain from the Langmuir binding model roughly $\Delta G_0 \simeq -15$ k_BT and from the CB model $\Delta G_0 \simeq -6.3$ k_BT. The volume change has a considerable effect on the electrostatic contribution which grows by several k_BT (see Section 4.3.3). This trend can be understood by the fact that the monomer charge density $c_M = \frac{N_M}{V_M}$ increases with CSM shrinking due to protein adsorption and the contributions in ΔG_{el} as given by Eq. (4.20) rise. Considering volume changes in charged systems is important for quantitative fitting, especially in those systems where deswelling is significant. In contrast to the standard Langmuir binding model, the nonspecific electrostatic contributions have been consistently separated and the remaining ΔG_0 becomes salt concentration independent.

Furthermore, we would like to comment on the magnitude of $\Delta G_0 \simeq -6.5$ k_BT for the intrinsic interaction of lysozyme with the pNiPAm network. If methane-methane interactions are taken as reference with attractions on the order of 2-3 k_BT, then 6.5 k_BT correspond to 2-

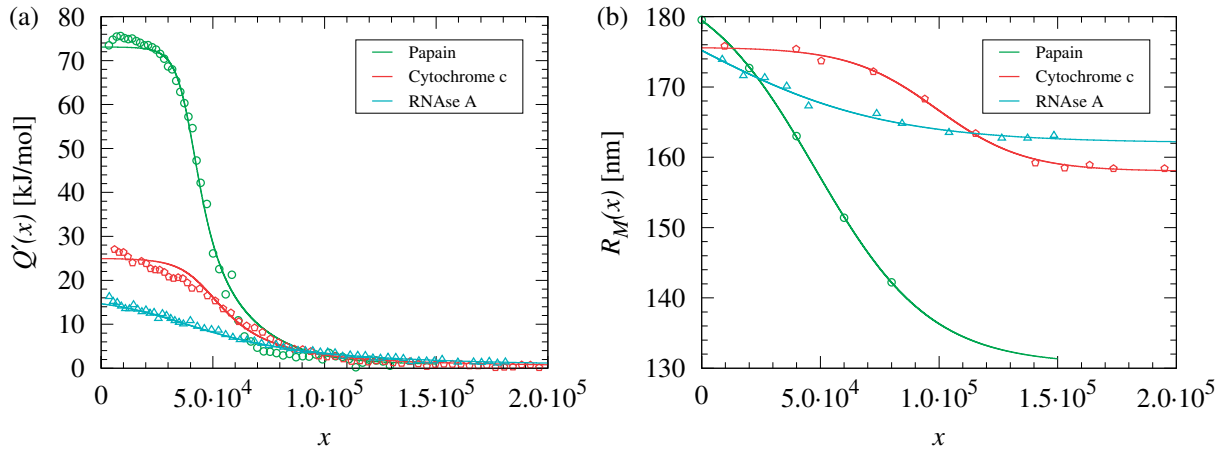


Figure 4.5: (a) Binding isotherms of papain, cytochrome c, and RNase A onto the CSM at 7 mM ionic strength and $T = 298$ K. (b) Change of the hydrodynamic radius of the CSM during protein uptake as obtained by DLS measurements. The DLS data are fitted by Eq. (4.35) and used as input in the CB model to fit the binding isotherms.

3 hydrophobic protein-pNiPAm contacts on average which seems reasonable. Increasing the temperature leads to an increase in ΔG_0 , which is conform with the signature of hydrophobic interactions [174]. A recent study on a similar system showed hardly uptake of lysozyme by an uncharged pNiPAm microgel [30]. Reasons for this discrepancy may be the different batches of CSM which may differ, *e.g.* in larger pore sizes within the CSM. Alternatively, we overestimate the effects of hydrophobicity and other local effects, such as salt bridges.

Other proteins

In the previous paragraph we have successfully separated the salt-independent intrinsic free energy. This advantage enables us to study the adsorption for other proteins at one single salt concentration.

The single adsorption of papain, cytochrome c, and RNase A to the CSM at 7 mM ionic strength by ITC demonstrates also a strong binding. The resulting binding isotherms are presented in Figure 4.5 (a), while the corresponding thermodynamic parameters are summarized in Table 4.3. The uptake of all proteins by the CSM is endothermic since $\Delta H_{\text{ITC}} > 0$. A particular point is the order of the binding enthalpies. Those are associated apparently with the net charges Z_i , because the magnitude of ΔG_0 is almost same for all proteins. Papain possesses the largest net charge and consequently the largest enthalpy change, followed by cytochrome c and RNase A. Hence, protein adsorption onto oppositely charged CSM particles is due to electrostatics and essentially determined by the net charge of the proteins. The ionizable groups on the protein surface play certainly a significant role in the binding process. This is the most likely reason why the swelling state of the CSM is different for all investigated proteins as shown in Figure 4.5 (b). For example, the adsorption of papain lead to a deswelling of roughly 65% of the core-shell particles, while for cytochrome c and RNase A the effect is less pronounced. This indicates that shrinkage is due to specific binding effects between CSM network monomers and adsorbed proteins. The protein radii R_P

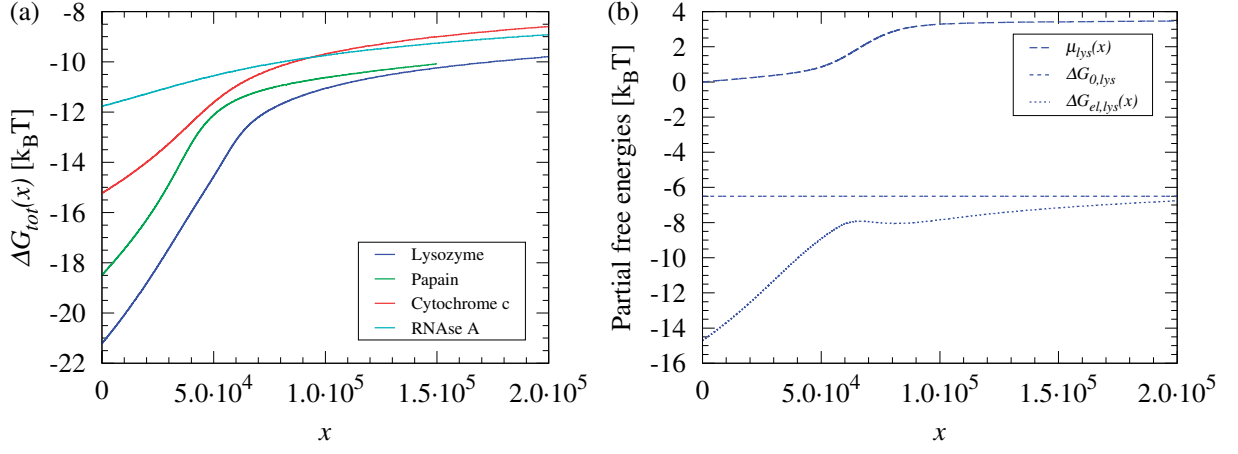


Figure 4.6: (a) Total binding energy ΔG_{tot} as a function of the molar ratio of the respective proteins at $c_s = 7$ mM and $T = 298$ K. (b) Decomposition of the total binding energy for lysozyme into its contributions; intrinsic adsorption free energy $\Delta G_{0,lys}$, electrostatic contribution $\Delta G_{el,lys}$, and configurational chemical potential μ_{lys}

used in this model show a very good agreement with hydrodynamic radii known from literature [175–178]. The same is true for the protein charge Z_P . The values were calculated from experimentally determined protein crystal structures provided by the Protein Data Bank (PDB) [179] or in case of RNase A from literature [180]. Table 4.3 summarizes all model parameters. The experimenters observed aggregation in adsorption experiment with papain at molar ratios $x > 80000$ (data not shown). Further experiments with papain were carried out not exceeding $x \approx 80000$.

4.3.3 The total binding energy

Figure 4.6 (a) presents the total binding affinity $\Delta G_{tot} = \Delta G_0 + \Delta G_{el} + \mu$ of all investigated proteins in the one-component case as obtained from the fitting of the ITC data at 7 mM ionic strength. Evidently, ΔG_{tot} is not a constant as presumed in the Langmuir binding model, but depends strongly on the protein load and thus on the molar ratio x . At low molar ratios, the binding affinity of lysozyme is the largest with $\Delta G_{tot} \simeq -21$ k_BT followed by papain with roughly $\Delta G_{tot} \simeq -18$ k_BT. Lysozyme has the highest intrinsic adsorption free energy and a relatively high net charge as shown in Table 4.3. Papain possesses the highest net charge of all proteins and thus a higher electrostatic attraction to the oppositely charged CSM. However, the non-electrostatic binding, expressed by ΔG_0 , is lower compared to lysozyme and therefore binds as the second most. The two other proteins, cytochrome c and RNase A bind less strongly to the CSM, which is reflected by their properties, also summarized in Table 4.3. From a thermodynamic point of view, the total binding energies ΔG_{tot} of all proteins have to converge to the same value in equilibrium. In fact, it is not the case as the protein density inside the CSM obviously depends on the CSM volume V_M . V_M itself depends on the molar ratio x in a protein-specific way.

For practical reasons, we show in Figure 4.6 (b) the different contributions to the binding affinity for lysozyme at 7 mM ionic strength. The intrinsic adsorption free energy ΔG_0 is

Table 4.3: Summary of the thermodynamic parameters determined from the binding isotherms of the adsorption of individual proteins onto the CSM at 7 mM ionic strength and $T = 298$ K.

Protein	ΔH_{ITC} [kJ/mol]	ΔG_0 [k _B T]	R_P [nm]	Z_P [e]
Lysozyme	59	-6.5 ^a	1.9 (1.9) ^b	+7 (+7) ^c
Papain	73	-4.5	2.2 (2.0) ^b	+8 (+7) ^c
Cytochrome c	25	-4.7	1.7 (1.8) ^b	+6 (+7) ^c
RNAse A	16	-4.1	1.8 (1.9) ^d	+4 (+4) ^d

^a: averaged over 7 mM, 17 mM, and 32 mM ionic strength, ^b: values for the hydrodynamic radii from literature, ^c: calculated protein charges from crystallographic structure (lysozyme: 193L, papain: 1PPN, cytochrome c: 2B4Z, RNAse A: 1AFU), ^d: from reference [180]

a constant contribution, while the electrostatic energy ΔG_{el} and the configurational chemical potential μ contributions depend explicitly on x . μ accounts for the entropic penalty of hard-sphere packing and is negligible small at low molar ratios. However, μ increases to unfavorable 3 k_BT in the saturation regime. We found $\Delta G_0 \simeq -6.5$ k_BT for lysozyme which constitutes roughly $\frac{1}{3}$ or $\frac{1}{2}$ of the total binding affinity in the small and high load regimes, respectively. The electrostatic binding energy as expressed by Eq. (4.20) consists of the electrostatic transfer energy and the Born solvation energy. The first term depends on the protein charge and the Donnan potential. At the beginning of the titration experiment, the magnitude of the Donnan potential is considerable and about $1.77 \frac{k_B T}{e}$ ($\simeq 44$ mV). The potential quickly decreases with protein load due to charge neutralization. The Donnan potential is also expected to be highly correlated with the surface potentials of the microgel which governs colloidal stability in solution [30]. We find that the Born contribution constitutes a favorable 2-3 k_BT to the electrostatic energy and cannot be neglected. Thus, the electrostatic contribution for very small protein loads ($x \simeq 0$) is big and may assume values up to -15 k_BT. This energy decomposition reveals that electrostatic forces contribute mainly to the binding event.

4.3.4 Interpretation of Langmuir and cooperative binding model results

In Section 4.3.2 we argued that the CB model is formally equivalent to the Langmuir approach in the low packing regime ($\eta \ll 1$), if the number of binding sites, N_P , is equal to the number of free spots, $\frac{V_M}{2B_2}$. Indeed, if we consider a mean CSM radius of $R_M = 150$ nm and for instance a protein diameter $\sigma_P = 3.8$ nm for lysozyme, we end up with $N_P = \frac{V_M}{2B_2} \simeq 59000$. This is completely consistent with numbers obtained from fitting to the Langmuir binding model, *cf.* Table 4.1. This agreement implies that the strict Langmuir assumption of a fixed set of binding sites can still be considered as an interpretable quantity, even if the nature of the bound state is not well-defined. From that point of view, the decrease in N_P in the Langmuir models with increasing ionic strengths can be understood: for increasing c_s , the CSM volume V_M decreases and packing penalties becoming more important for a smaller number N_P of bound protein. Hence, in the standard Langmuir fitting of the ITC data sets

for adsorption onto soft materials [22, 23, 25–27, 160], it is not likely that a condensation-like binding of proteins takes place. Thus, the stoichiometry of binding may be interpreted taking packing effects into account.

As we demonstrated in Figure 4.6 (b), the electrostatic and configurational energies and therefore the total binding affinity ΔG_{tot} are functions of the molar ratio x . Consequently, the question arises how the constant K from the standard Langmuir fitting can be interpreted [22, 23, 25–27, 160]. As argued in Section 3.5.1 fitting is most sensitive within the pre-saturation region $x \simeq N_P$. Indeed, the data in Figure 4.6 (a) shows that $\Delta G_{tot}(x \simeq N_P)$ equals the values of the standard Langmuir fitting, see Table 4.1. Thus, we can conclude that a binding constant obtained from a standard Langmuir fit is a reasonable number, which can be interpreted as binding affinities in the pre-saturation regime, *i.e.*, in the intermediate to high protein load regime, where also volume changes are not so large anymore. However, for small protein loads ($x \ll N_P$) our separation into electrostatic and hydrophobic contributions shows that binding affinities can be much larger than in the pre-saturation regime. This may have implications for the modeling and interpretation of protein binding kinetics [22, 24, 51, 181].

4.4 Competitive protein adsorption of binary mixtures: comparison between experiment and theory

In the previous section we have elaborated thermodynamical parameters of single protein binding onto CSM using our CB model. As a matter of course, these parameters can be reinstated into the CB model to predict competitive adsorption between two or more proteins onto the CSM. This type of prediction is new for multi-component mixtures of proteins because no further parameters as listed in Table 4.3 are involved.

The results of competitive protein adsorption experiments by means of fluorescence spectroscopy at 7 mM salt concentration are shown in Figure 4.7. First, around 60% FITC labeled lysozyme (lysozyme^{FITC}) proteins are adsorbed to the CSM. The binding fraction Θ is calculated by assuming a maximum number of binding sites of $N_S = 65000$ from experimental consideration. When a second protein bounds onto the CSM, a certain number of lysozyme^{FITC} will be released and thus recorded by the change of the fluorescence intensity. We investigated the competitive adsorption of unlabeled lysozyme to a CSM loaded with lysozyme^{FITC} as shown in Figure 4.7 (a). In this case, all thermodynamic parameters are the same and no CSM volume change is assumed. Moreover, this particular case can also be exploited to demonstrate the reversibility of protein adsorption onto the CSM and more importantly to proof the validity of our CB model. The lysozyme^{FITC}-lysozyme exchange exhibits the predicted intersection point at nearly half the initial binding fraction at $\Theta \approx 0.38$. At the intersection point, the ratio between lysozyme^{FITC} and unlabeled lysozyme is 1:1. This confirms that protein adsorption to the CSM is a equilibrium process without

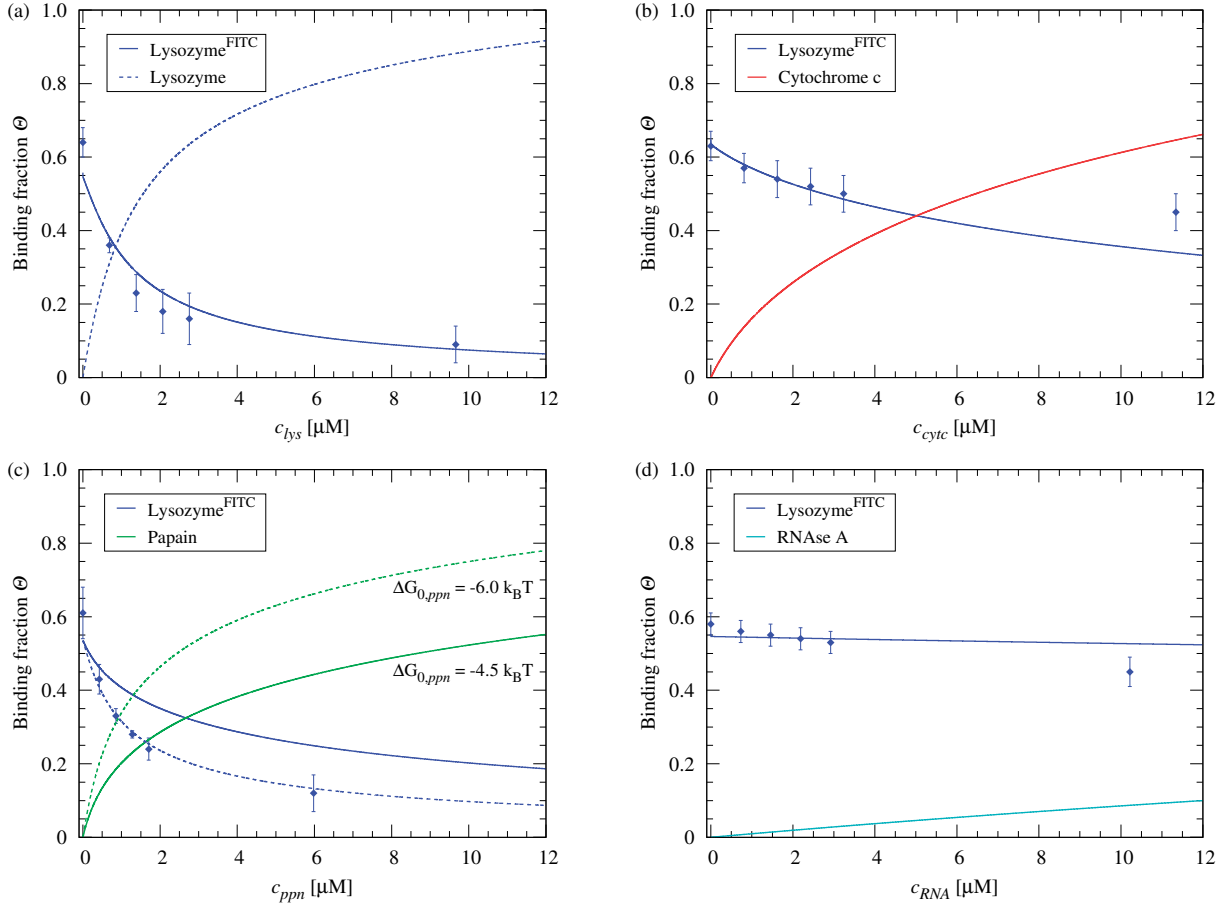


Figure 4.7: Competitive protein adsorption measured by fluorescence spectroscopy at $c_s = 7$ mM and $T = 298$ K. (a) lysozyme^{FITC} vs. lysozyme, (b) lysozyme^{FITC} vs. cytochrome c, (c) lysozyme^{FITC} vs. papain, and (d) lysozyme^{FITC} vs. RNase A. Θ is the binding fraction calculated from the change in fluorescence intensity. Solid and dotted lines predict the competitive adsorption based on the CB model.

a doubt. For the other proteins we incorporate the CSM volume change by an interpolation of V_M as defined in Eq. (4.36). Except for papain, all predictions by theory agree quantitatively with experimental binding and desorption values of the competing proteins. Thus, RNase A displaying the lowest binding constant and net charge, replaces the bound lysozyme^{FITC} (Figure 4.7 (d)) to a lower extent than cytochrome c (Figure 4.7 (b)). Using $\Delta G_0 = -4.5$ k_BT for papain, the prediction of the CB model is not satisfying. However, adapting $\Delta G_0 = -6$ k_BT, agreement with the experimental data set can be achieved. This discrepancy is not entirely understood. The reason may be probably a strong mutual attraction of the bound proteins within the CSM, which is not yet included in the CB model.

4.5 Concluding remarks

In this chapter, we have introduced a multi-component cooperative binding model to characterize physical interactions of protein adsorption onto CSM particles in thermodynamical equilibrium. In particular, single and competitive adsorption of lysozyme, papain, cytochrome c, and RNase A by the CSM was experimentally studied and compared with model calculations. The model separates electrostatic cooperativity and yields a salt-independent

(intrinsic) interaction energy ΔG_0 of proteins with CSM particles. Packing constraints between the proteins inside the CSM as well as the deswelling behavior of the CSM volume were also taken into account. Hence, a more quantitative interpretation of binding value [22, 23, 25–27, 30, 31, 160] in terms of separate physical interactions is possible. We have shown particularly that fitting based on standard Langmuir binding models yields interpretable binding affinities and stoichiometry. Once the intrinsic adsorption free energies are obtained from ITC experiments with one-component protein solutions, the competitive adsorption of an arbitrary mixture can be predicted. Here, we have successfully predicted the competitive adsorption and desorption of binary protein mixtures onto the CSM.

5 Simulation of protein adsorption onto soft polymeric biomaterials

This chapter presents a comprehensive study of protein adsorption to a single polyelectrolyte and planar polyelectrolyte brush by means of Langevin dynamics computer simulations. By constructing well-defined models for patchy proteins and coarse-grained models for the PE materials, the adsorption process as well as the effective pair interactions between like-charged proteins, associations of like-charged protein-PE complexes, and the uptake of an oppositely and like-charged protein by a PE brush are investigated depending on various physical parameters. Simple analytical models are also developed and compared to the simulation results.

5.1 Models and methods

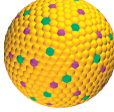
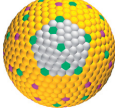
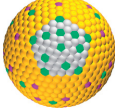
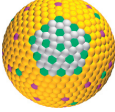
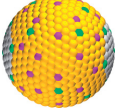
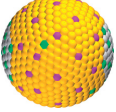
In this section, we introduce the models used for the biomaterials and describe the method and details of the simulations. How we calculate the potential of mean force between two binding partners, specify ion condensation on the surface of the biomaterials, and define a patch vector is explained afterwards.

5.1.1 Charged patchy protein models

Our aim is to introduce spherical particle models for nanometer-sized globular proteins that do not unfold and change their structure with well-defined patchiness and multipolarity, including the effects of charge discreteness. For this, we start the construction of our charged patchy protein models (CPPMs) with subdivisions of the triangular faces of an icosahedron. This way we obtain points (represented as colored beads in Table 5.1) and project them onto a sphere with radius $R_P = 2$ nm. This is a size typical for small globular proteins such as lysozyme or lactoglobulin [182]. With that, the rough but essentially spherical surface is composed of 642 beads plus one auxiliary bead we place in the centroid and can be bonded to surface beads for an additional stabilization of the structure. The bond length b_P of neighboring beads on the surface is between 0.28 nm and 0.31 nm, while the spring constant K_P connecting neighboring beads is fixed to $4100 \frac{\text{kJ}}{\text{mol nm}^2}$.

To build a charge patch, one bead on the surface is randomly chosen and subsequently the closest neighbor beads are selected until the required patch area $A_P = 3 \text{ nm}^2$ is achieved. This size of the area is on the same order as the size of naturally occurring larger clusters of charged amino acids of the same sign, based on the inspection of crystal structures of small globular proteins such as lactoglobulin [183]. Afterwards, s positive charges are placed on the patch. We construct protein models with one ($m = 1$) or two ($m = 2$) patches. In protein models with two patches the patches are antipodally directed, that is, on the

Table 5.1: A Summary of our charged patchy protein models (CPPMs) denoted by P_s^m . The index m stands for the number of patches, while s denotes the number of positive charges on each patch. In the images of the CPPMs in the top row, the pink beads depict the negatively charged atoms, while turquoise beads depict the positively ones. Yellow and white atoms depict the same neutral atoms and are only distinguished here to better illustrate the patch region which roughly has an area of 3 nm^2 . All CPPMs have a radius of $R_P = 2 \text{ nm}$ and a net charge of $Q_P = -8 \text{ e}$. The patchy proteins carry individual dipole moments as also summarized in the Table. The corresponding quadrupole (tensorial) moments are provided in the Appendix B.

						
Label	P_0^0	P_8^1	P_{12}^1	P_{16}^1	P_8^2	P_{12}^2
Radius R_P [nm]	2	2	2	2	2	2
Patch area A_P [nm ²]	0	3	3	3	3 (x2)	3 (x2)
Total charge Q_P [e]	-8	-8	-8	-8	-8	-8
Dipole moment μ_P [D]	158.67	896.03	1328.71	1632.67	206.41	151.12

exact opposite sides. In order to assign a net charge Q_P to the patchy proteins, we fixed the number of negatively and positively charged beads to be $N_n = 37$ and $N_p = 29$ in all protein models. Thus, the resulting net charge of the patchy proteins is $Q_P = -8 \text{ e}$ for all CPPMs, comparable to absolute protein net charges of proteins of similar size at physiological conditions. The N_n negative charges are homogeneously distributed on the surface around the positive patch. The remaining $N_p - m \cdot s$ positive charges are distributed in such a way that charged beads (positive or negative) are not immediately adjacent. Our globular protein models are denoted by P_s^m where m specifies the number of patches and s the number of positively charged beads per patch.

See Table 5.1 for illustrative snapshots and a summary of the CPPM features, in particular, the dipole moments. In our models we consider $m = 1, 2$ and $s = 8, 12, 16$ resulting in mean patch charge densities (per area) of around 1 to 2 e/nm² corresponding to a local assembly of a few amino acids separated from each other by a few Ångströms [61, 183]. The dipole moments are in the range of 159 Debye to 1633 Debye, *cf.* Table 5.1, also comparable to proteins of this size. Lactoglobulin, for instance, has 730 Debye [184]. The quadrupole moments of the patchy proteins are given in the Appendix B.

5.1.2 Polyelectrolyte and polyelectrolyte brush models

A simple bead-spring model for the PE chain and PE brush that is suitable for our purposes is described in the following.

Polyelectrolyte

A single flexible PE is modeled in a coarse-grained fashion as a sequence of N_{mon} freely jointed beads. Each bead represents a monomer with a radius σ_{LJ} and an electric charge of one negative elementary charge e . Thus, the fraction of ionized monomers is $f_{\text{mon}} = 1$. The PE monomers are connected by a harmonic bond potential with an equilibrium bond length

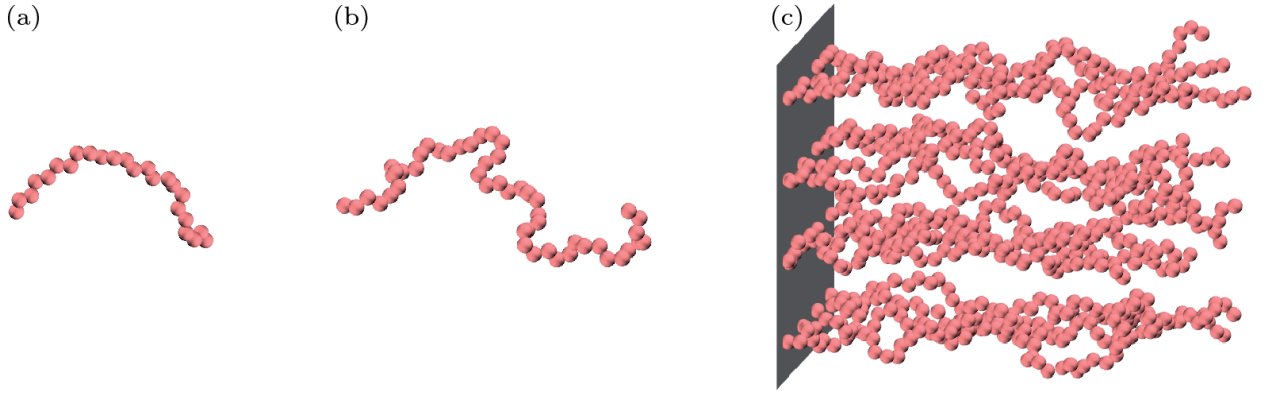


Figure 5.1: Coarse-grained models of single polyelectrolytes and a polyelectrolyte brush. Typical configurations of PE chain lengths with (a) PE_{25} , (b) PE_{50} , and (c) a PE brush B_{50} with 50 monomers per PE chain.

$b_{\text{mon}} = 0.4 \text{ nm}$ and a force constant $K_{\text{mon}} = 4100 \frac{\text{kJ}}{\text{mol nm}^2}$. The flexibility of the PE chain is ensured via a harmonic angle potential in which the angle between a triplet of monomers is $\gamma = 120^\circ$ and the force constant is $K_\gamma = 418 \frac{\text{kJ}}{\text{mol rad}^2}$. In our studies, we consider relatively short PE chains with monomers of $N_{\text{mon}} = 25$ and $N_{\text{mon}} = 50$ as used in related experimental studies [185–187].

Polyelectrolyte brush

The PE brush model is composed of 16 flexible PE chains each with 50 monomers and fixed at one end on a neutral and planar surface in equidistant spacings. With a surface area of 100 nm^2 , the grafting density corresponds to $\tau_B = 0.16 \frac{\text{molecules}}{\text{nm}^2}$. See also Figure 5.1 for example snapshots of single PE chains and PE brush.

5.1.3 Simulation method and details

In our simulations, the dynamics of each bead is governed by Langevin’s equation of motion (see Section 3.3). The potential energy of the system U is given by

$$U = U_{\text{bond}} + U_{\text{ang}} + U_{\text{LJ}} + U_{\text{Coul}} + U_{\text{res}}, \quad (5.1)$$

where U_{bond} and U_{ang} are harmonic intramolecular bonded and angular interactions between neighboring beads in a molecule. Note that we have not specified angle potentials for the patchy protein models. Interatomic Lennard-Jones interactions U_{LJ} between all non-bonded beads and Coulombic interactions U_{Coul} between all charged beads govern the pair potential. Additionally, we have applied a harmonic restraint potential U_{res} to fix a molecule or atoms to a reference position.

The simulations are performed using the GROMACS 4.5.4 software package [188]. A leap-frog algorithm with a time step of 2 fs is used to integrate the equations of motion. The Langevin thermostat with $\xi_i = 0.5 \text{ ps}^{-1}$ keeps the temperature at $T = 298 \text{ K}$. Center of mass translation of the system is removed every 10 steps. The cut-off radius is set to 1.2 nm to

calculate the real-space interactions, while Particle-Mesh-Ewald (PME) is implemented to account for long-range electrostatics [189]. The solvent is modeled as a continuous medium with a static dielectric constant $\epsilon_r = 78.44$ whereas the ions are explicitly considered. All particles (either a bead or an ion) have mass $m_i = 1$ amu, diameter $\sigma_{LJ} = 0.3$ nm, energy well $\epsilon_{LJ} = 0.1$ k_BT and integer charges $q_i = 0, +1$ or -1 e. The mass was chosen artificially low to enhance orientational fluctuations and sampling. Clearly, equilibrium properties, as investigated in this thesis, are not affected by any reasonable mass choices as long as the simulations are ergodic.

Setting up a simulation box

Since we consider different types of systems, it is appropriate to select suitable simulation boxes for the respective systems to prevent artifacts and to realize an isolated system.

1. Protein-protein and protein-PE simulations

For the simulations of single and pairs of patchy proteins as well as protein-PE complexes, a cubic box with side lengths of $L = 30$ nm is employed and periodically replicated in all spatial directions to generate a quasi-infinite system. The PME method is computed in the reciprocal space with a FFT grid of 0.47 nm spacing and a cubic interpolation of fourth-order. When building the simulation box, the protein with the lower dipole moment in case of protein-protein simulations and the protein in case of protein-PE simulations are position-restrained in the box center but still free to rotate. The respective second molecule is initially positioned at a distance of $r \approx 11$ nm relative to their individual mass centers. Note also that in single protein simulations the protein is also position-restrained in the center of the box.

2. Protein uptake by a PE brush simulations

The rectangular simulation box with $L_x = L_y = 10$ nm, and $L_z = 30$ nm is periodic only in the x, y -directions, while at $z = 0$ nm and $z = 30$ nm walls are placed. The walls, each having a density of $0.5 \frac{\text{nm}^3}{\text{nm}^2}$ are represented by a 9-3 Lennard-Jones potential. The reciprocal summation of the PME method is still computed on a 3D FFT grid but with spacings of 0.32 nm in x, y -directions and 0.23 nm in z -direction using a fourth-order interpolation. Because of the periodicity, a correction term to the Ewald summation in the z -direction is added to produce a pseudo-2D summation [190, 191]. While one end of the PE chains is position-restrained in the immediate vicinity of the wall at $z = 0$ nm by a harmonic potential, the globular protein is initially placed at $z \approx 26$ nm.

After the simulation box is set up, the corresponding number of counterions is added to ensure electroneutrality of the system. Additionally, monovalent salt of different concentrations c_s is added to the system. Because all ions are randomly placed, the system is relaxed for 100 ps to remove local contacts and afterwards equilibrated for 30 ns.

5.1.4 Calculating the potential of mean force

For calculating the potential of mean force (PMF) between two binding partners we use steered Langevin dynamics (SLD) [85] as realized by the pull code in the GROMACS software. Here, the center of mass of one molecule (either a protein or a PE) is restrained in space by an external time-dependent force. This force is applied as a constraint, *e.g.* by a harmonic potential, and moved with a constant pulling velocity v_p to steer the molecule in the prescribed direction [85]. After several test runs, the pulling rate $v_p = 0.1 \frac{\text{nm}}{\text{ns}}$ was chosen which is small enough to warrant equilibrium sampling and a harmonic force constant $K_p = 2500 \frac{\text{kJ}}{\text{mol nm}^2}$. The pulling rate also determines the simulation time that is required to bring the binding partners from a separated state to a contact state. The simulation of the PMF takes 70 ns ($3.5 \cdot 10^7$ steps) between two globular proteins, 105 ns ($5.25 \cdot 10^7$ steps) for the formation of a protein-PE complex, and 240 ns ($1.2 \cdot 10^8$ steps) for the protein uptake by a PE brush. The standard deviation was calculated by standard block averages to specify the statistical error.

After a successful simulation run, the friction force $F_{vis} = -m\xi v_p$ was subtracted from the constraint force and averaged within a specific interval of discrete spacing Δr to obtain the mean force. According to our simulation setup, the mean force was integrated backwards to get the PMF. Because the object is constraint in space, the PMF has to be corrected for entropic effects [192–194] by

$$w(r) = w^I(r) - (c - 1)k_B T \ln[r], \quad (5.2)$$

where $w^I(r)$ is the integrated mean force and c the dimension of the constraint.

Additionally, standard umbrella sampling (US) simulations as implemented in GROMACS were carried out for certain protein-protein combinations to countercheck the results of the SLD method. We emphasize that in all our simulations the globular proteins were able to rotate freely and thus all our results are orientation-averaged with the appropriate and correct Boltzmann-weight.

5.1.5 Ion counting and patch orientation

In order to count ions in the immediate vicinity of a molecular surface of arbitrary shape, a finite volume element over the surface is constructed. The volume element is made up from the superposition of spheres with a fixed radius r_s centered at each molecular bead B_i as depicted in Figure 5.2 (a). Since the surface can be contorted, care is taken to the overlapping volumes to avoid double counting of ions. As an example, consider following situations (see Figure 5.2 (a)):

- The ion I_1 is within the radius r_s of B_1 and B_2 but closer to B_2 . Therefore, I_1 is condensed on B_2 and is only counted once.

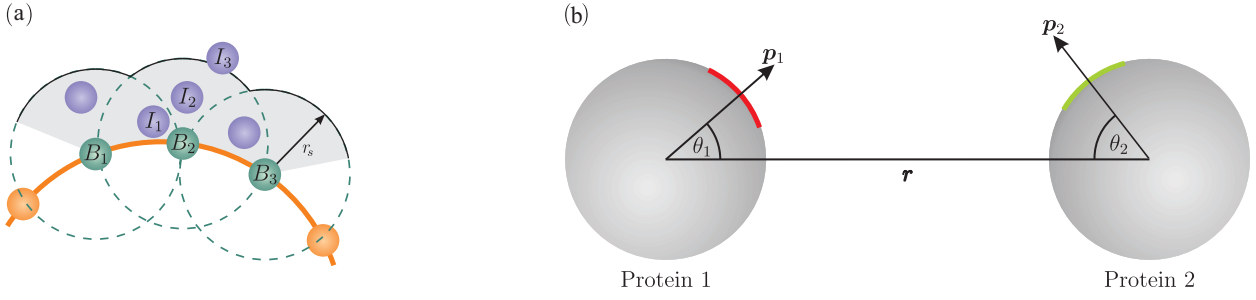


Figure 5.2: (a) A descriptive illustration of ion counting I_i in a finite volume element. For the construction of the finite volume, spheres with radius r_s are centered at each surface bead B_i . (b) A geometrical sketch of the patch orientation. The angular orientation θ_i is defined by the patch vector \mathbf{p}_i and the distance vector \mathbf{r} connecting the two centers of mass of both molecules.

- The center of ion I_3 is outside of the radius r_s . Thus, I_3 is not counted.

According to our definition, ions found in the volume element are *condensed* on the molecular surface and N_c denotes the number of condensed ions. If it is not mentioned otherwise, r_s is fixed to 0.4 nm in this thesis.

The introduction of a patch vector provides a method to analyze the angular orientation of the patch between the mass centers of the molecules of interest in dependence of their center-to-center separation \mathbf{r} , as represented in Figure 5.2 (b). The patch vector \mathbf{p} points from the protein center to the patch center and provides also a very good approximation of the dipole direction of the P_s^1 models. In our analysis we computed the distance-resolved cosine of the angle $\theta_i(r)$ by

$$\cos[\theta_i(r)] = \left\langle \frac{\mathbf{p}_i \cdot \mathbf{r}}{|\mathbf{p}_i| \cdot |\mathbf{r}|} \right\rangle_r, \quad (5.3)$$

where we average $\langle \cdot \rangle_r$ at a fixed distance r . The distance-dependent angular correlation of the patch vectors is calculated via the second Legendre polynomial $P_2(\cos[\theta])$ with $P_2(x) = \frac{3x^2-1}{2}$. In protein models with two patches only one patch is used to calculate the orientation since the patches are antipodally directed.

5.2 Simulations of charged patchy proteins

This section presents simulations with single and pair of patchy proteins in monovalent electrolyte solutions. The main focus is put on the comparison of simulation results with predictions obtained from theoretical models.

5.2.1 Ionic and potential distribution around a single protein

The normalized radial density distribution functions $g_{\pm}(r) = \frac{c_{\pm}(r)}{c_s}$ obtained from simulations with a single globular protein in an electrolyte solution of 20 mM and 100 mM ionic strength are shown in Figure 5.3. As expected, counterions are overall concentrated around the

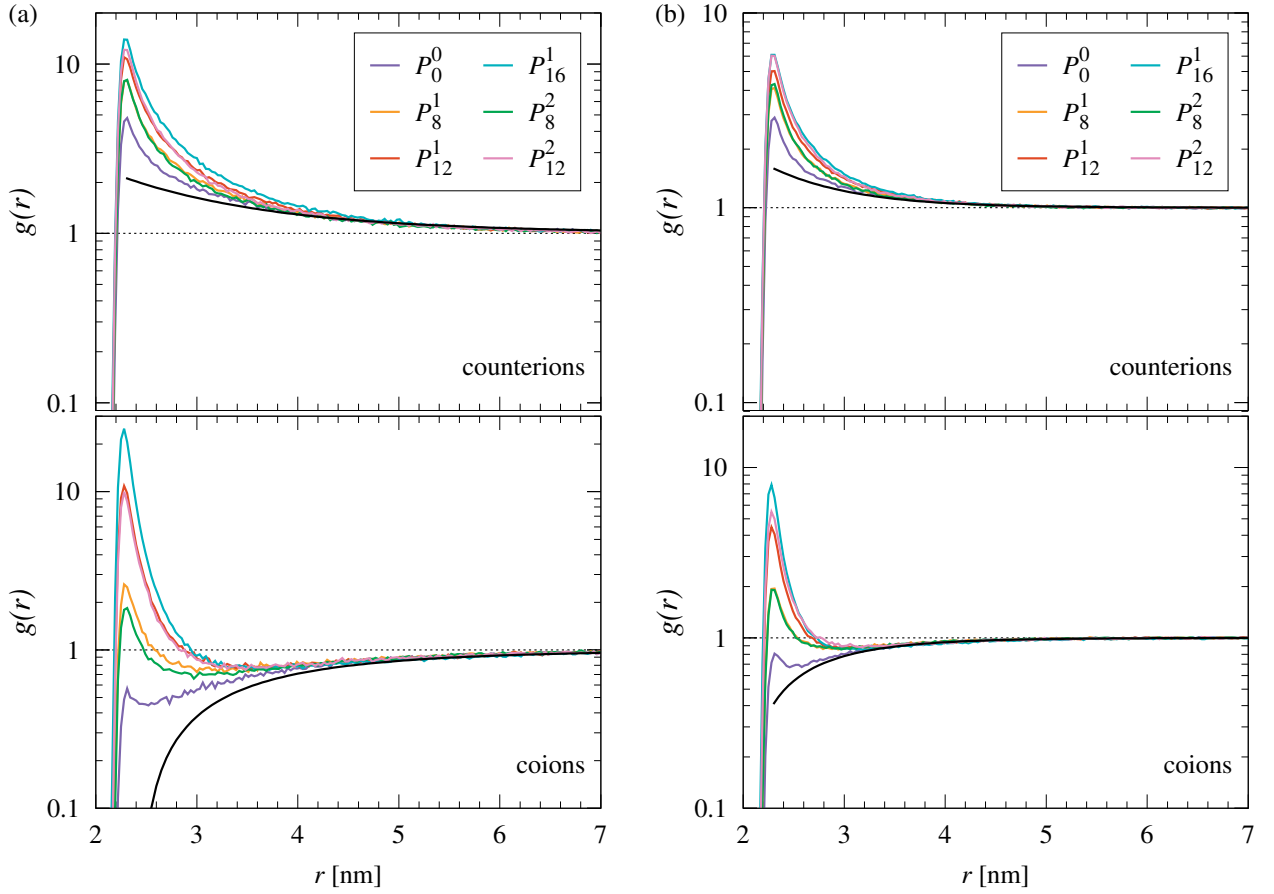


Figure 5.3: Normalized radial density distribution functions $g(r)$ of counterions and coions around a single globular protein as denoted in the legend. The simulations were conducted in an ionic solution of (a) 20 mM and (b) 100 mM. The black solid lines are predictions from the Debye-Hückel theory for a uniformly charged sphere of the same net charge $Q = -8 e$.

oppositely charged spheres, while the coions show a more peculiar behavior. The latter are depleted only for larger distances ($r \gtrsim 3$ nm) while, apart from the patchless P_0^0 , they are concentrated close to the protein. Even for P_0^0 a small peak of the coions at contact at around $r \approx 2.3$ nm is visible, owing to the discreteness and mixed charge distribution on the protein surface, where a few coions are attracted to single positive beads. This demonstrates clearly the presence of a local Stern layer of bound ions due to surface discreteness with probable implications for the exact value of the surface potential.

In the case of one patch and increasing surface charge density (*i.e.*, increasing s in P_s^1) both, the counterion and coion concentration close to the surface are enhanced. The reason is the growing attraction of coions to the positive patches which in turn are neutralized by accompanying counterions. However, increasing the number of patches from 1 to 2 interestingly leaves the contact peaks roughly unchanged, even decreases it notably in the case of coions at 20 mM ionic strength, pointing to some correlation effects between the two patches. As expected, the addition of salt screens electrostatic interaction and the density profiles in the 100 mM case are more short-ranged and have overall smaller contact peaks, *cf.* Figure 5.3 (b). Additionally to the simulation results, in Figure 5.3 predictions from the DH Eq. (3.11) for the ion profiles around a uniformly charged sphere of the same net charge

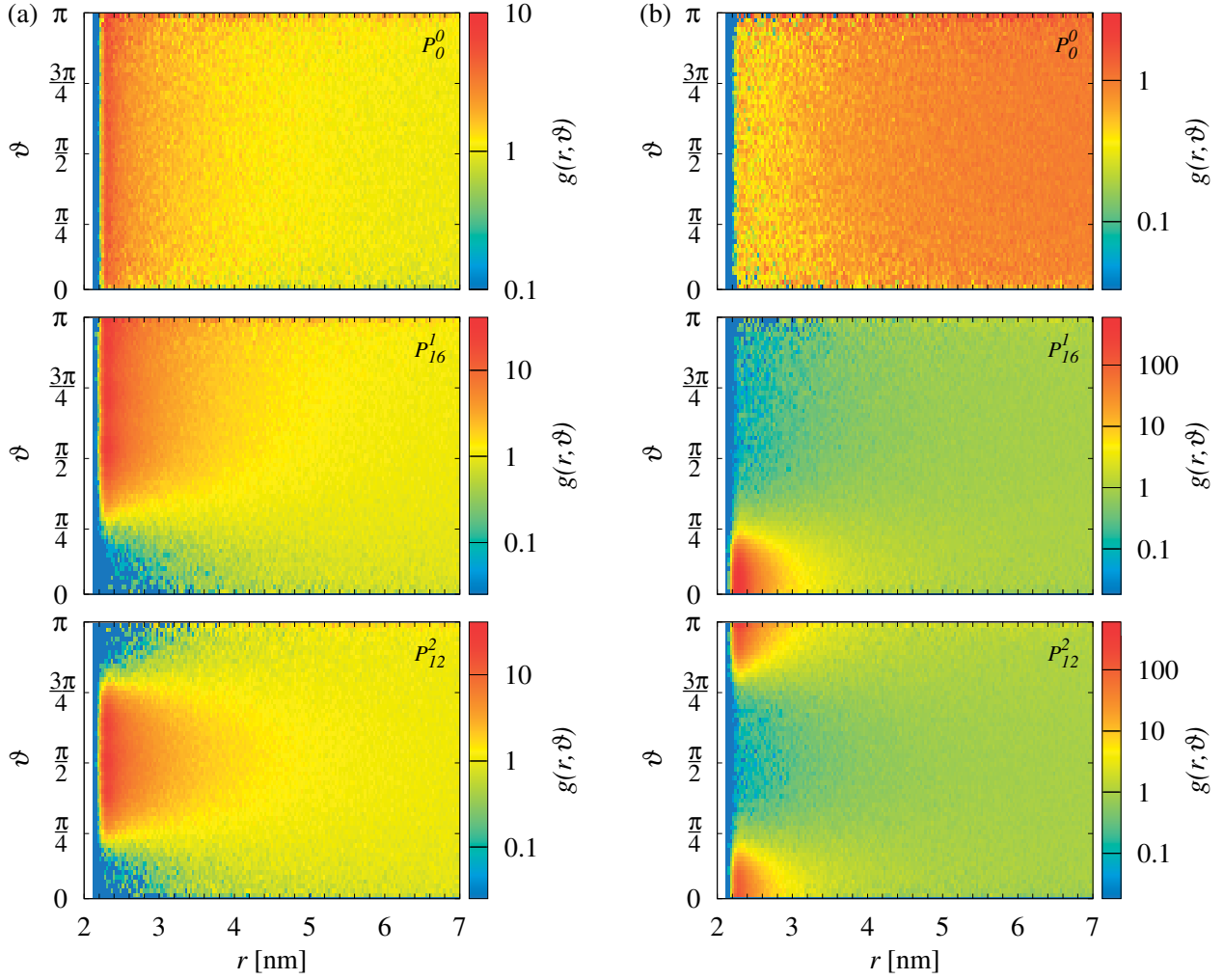


Figure 5.4: Angle-dependent distribution functions $g(r, \vartheta)$ of (a) counterions and (b) coions around a single globular protein P_s^m in an ionic solution of 20 mM. For the one-patched P_{16}^1 and two-patched P_{12}^2 a clear modulation of counterion and coion density distribution is visible due to the accumulation of the respective ions at the patches.

as the globular proteins are presented (solid black lines). Due to the spherical DH solution, it is clear that the enrichment and contact peaks of the coion profiles can not be described. For the simplest protein P_0^0 , which resembles closest a uniformly charged sphere, apart from discreteness effects at the protein surface, the agreement is satisfying at 100 mM but fails at 20 mM. Deviations from this linear theory in the latter case must be obviously attributed to the presence of high surface potentials, as will be shown further below.

Figure 5.4 (a) and (b) shows the angle-dependent distribution functions $g(r, \vartheta)$ for counterions and coions, respectively, for the case of 20 mM salt concentration. Since P_0^0 is essentially homogeneously charged there is no particular accumulation of ions to a certain angular surface region. The situation changes when patches are present. For instance, P_{16}^1 has a highly positive patch leading to a large accumulation of coions and to a depletion of counterions at the patch in a range of $\vartheta : 0^\circ - \frac{\pi}{4}$. Because the patches in P_{12}^2 are antipodally directed, accumulation and depletion of coions and counterions are found on both patches ($\vartheta : 0^\circ - 40^\circ$ and $150^\circ - \pi$). The range of accumulation of the ions (red regions in r -direction) in Figure 5.4 (a) and (b) is well described by the DH screening length $\kappa^{-1} \approx 2.1$ nm for

20 mM ionic strength.

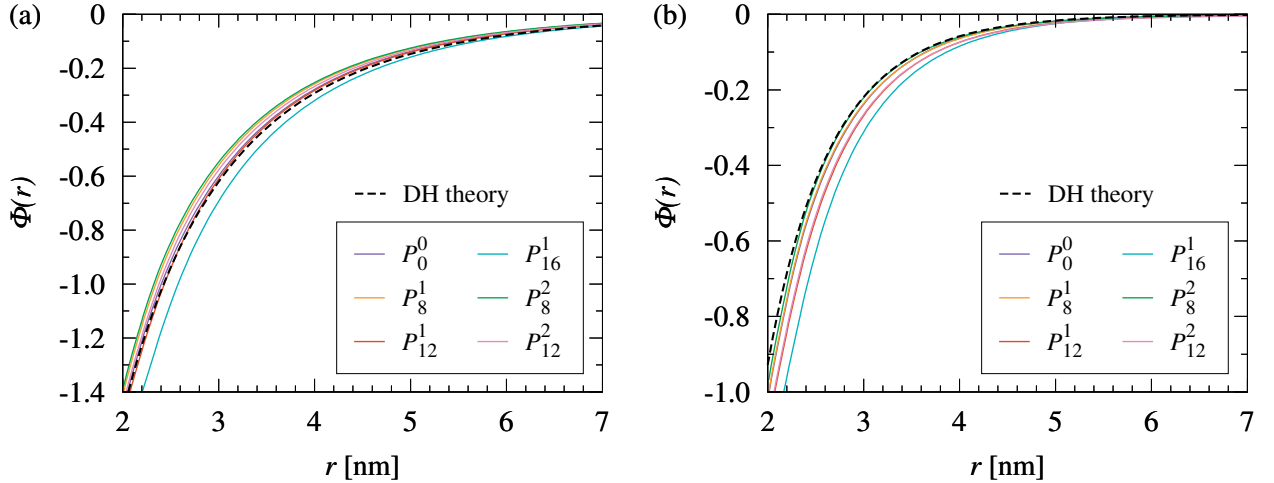


Figure 5.5: Dimensionless radial electrostatic potentials surrounding a single globular protein in a solution of (a) 20 mM and (b) 100 mM ionic strength. The colored solid lines represent the electrostatic potentials calculated from simulations via Poisson's equation, while the black dashed line is a prediction from the classical DH theory.

In Figure 5.5 (a) and (b) the dimensionless radial electrostatic potential $\Phi(r)$ around a single globular protein is presented along with the DH prediction from Eq. (3.11) for uniformly charged spheres with charge $Q = -8 e$ and radius $R_P = 2$ nm for 20 mM and 100 mM salt concentration, respectively. The prediction from the pure DH theory is very good, even without rescaling the charges since we operate in a regime of intermediate $\kappa R_P \simeq 1$ and small structural charges [97]. An interesting effect observable in Figures 5.5 (a) and (b) is that with changing patchiness the electrostatic potentials hardly change. This can be understood by looking at the cumulative (running coordination) number of counterions and coions close to the protein surface as illustrated in Figure 5.6. Increasing patchiness enhances the number of coions which in turn is accompanied by an increasing number of counterions. The small difference of 2-3 ions between the cumulative numbers of the counterions and coions $\Delta N = N_+ - N_-$ for increasing patchiness, shown in Figure 5.7, indicates that in the vicinity of the protein surface ($r \approx 2.3$ nm) there are only small changes in the radial net space charge. Since the potential results from the (double) integration of the latter, the mean surface potential prevails almost independent from the degree of patchiness. This finding is not so obvious for the small salt concentration (20 mM) where we expected some nonlinear effects in ion screening.

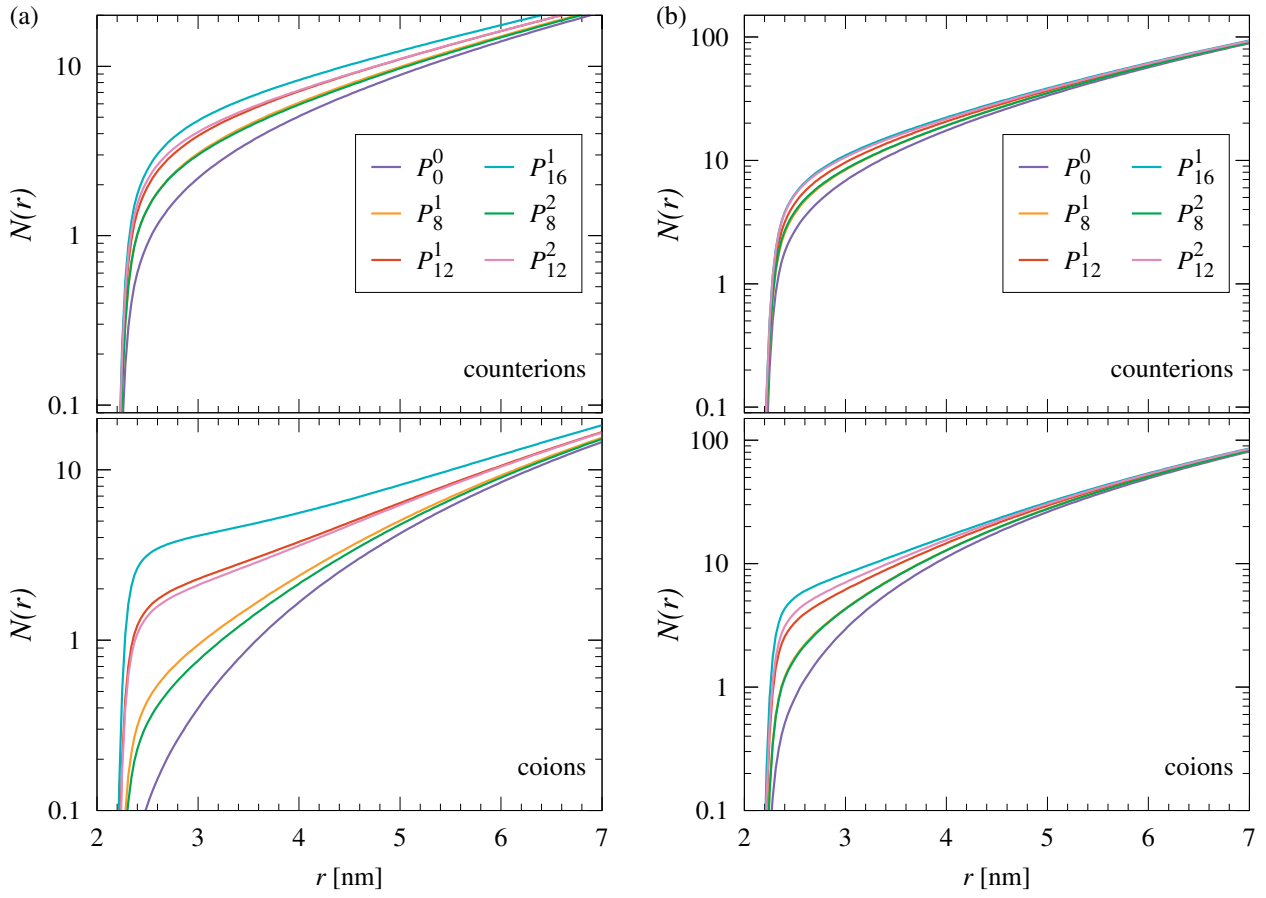


Figure 5.6: Cumulative number of counterions and coions around a globular protein in a solution of (a) 20 mM and (b) 100 mM ionic strength.

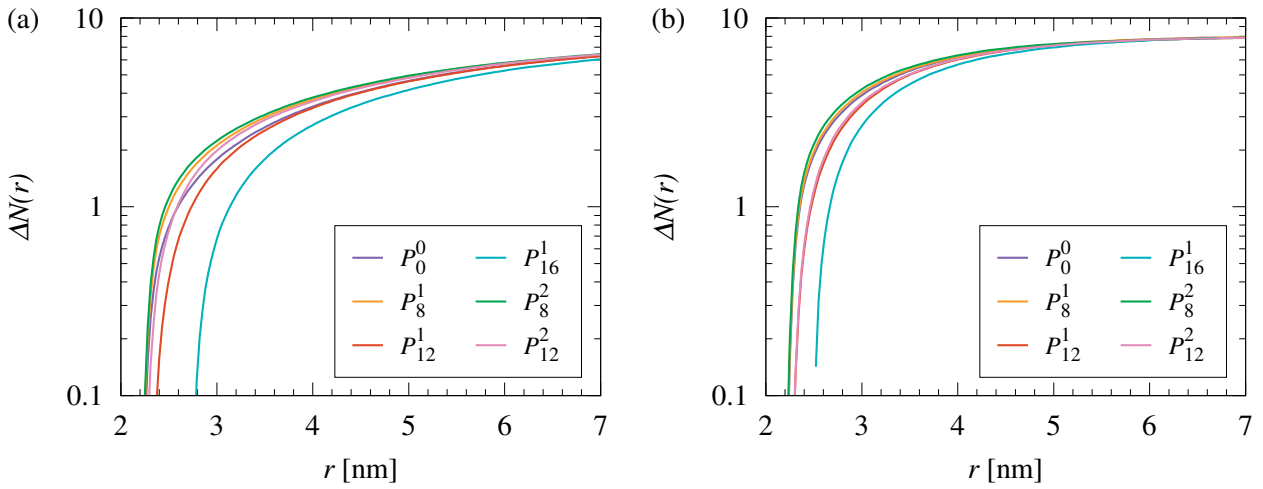


Figure 5.7: Difference regarding the cumulative number of counterions and coions for (a) 20 mM and (b) 100 mM salt concentration.

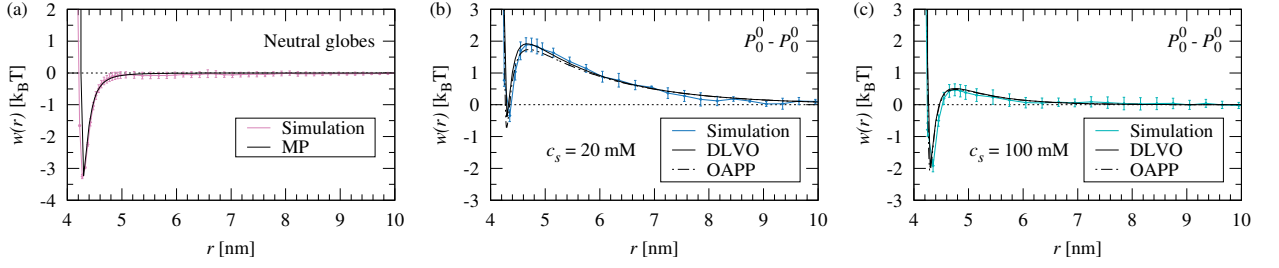


Figure 5.8: Panel (a) shows the PMF between two neutral spheres of the same elementary form as the proteins, while the solid black line displays the Mie potential with $n = 5$ and $k = 3$. Panels (b) and (c) represent the PMFs for $[P_0^0 - P_0^0]$ at $c_s = 20$ mM and $c_s = 100$ mM as a function of the center-to-center separation r , while the black lines are the DLVO potential (solid) and the OAPP (dashed). The colored symbols with error bars are simulation results.

5.2.2 Effective interaction between two proteins

In Figure 5.8 (a) the PMF between two neutral spheres is presented fitted by the Mie potential (solid black line) with $r = r - 2R_0$ and the parameters $n = 5$, $k = 3$, $\epsilon^* = 3.25$ k_BT, $\sigma^* = 0.15$ nm, and $R_0 = 2.05$ nm. The radius R_0 and the protein radius R_P have slightly different values due to the roughness and the fluctuations of the sphere surface. It can be recognized that at large distances ($r \gtrsim 5$ nm) no forces between the neutral spheres prevail. Once the spheres come closer, the van der Waals attraction rises and leads to the global minimum ϵ^* at $r \approx 4.3$ nm and upon further approach the PMF is expectedly repulsive.

The PMFs for the charged but patchless $[P_0^0 - P_0^0]$ pair at ionic strengths of 20 mM and 100 mM are shown in Figure 5.8 (b) and (c), respectively. Both are mostly repulsive, as anticipated, due to the long-ranged monopole repulsion, while at 100 mM ionic strength the repulsion is shorter-ranged due to higher screening by the salt. At small separations ($r \lesssim 4.6$ nm) both PMFs become attractive due to the van der Waals interactions. In addition, the DLVO potential, that is, Eq. (3.19), and the OAPP Eq. (3.26) are also shown in the figures. As expected from our successful DH description of the electrostatic potential around a single P_0^0 , we find that the PMFs at 20 mM and 100 mM salt concentrations are in very good agreement with the analytical models using $R_P = 2.0$ nm, the dipole value in Table 5.1 (for OAPP only), and a not renormalized charge $Q_P = -8$ e. Note that the small difference of DLVO and OAPP PMFs in Figure 5.8 (b) arises from the small but non-vanishing dipole moment of the P_0^0 particle.

Results for monopole-dipole $[P_0^0 - P_s^1]$ pairs with $s = 8, 12, 16$ are presented in Figure 5.9 and 5.10 for $c_s = 20$ mM and $c_s = 100$ mM, respectively. Note that in addition to the SLD sampling of the PMF, standard umbrella sampling (US) was performed for $[P_0^0 - P_{16}^1]$ at 20 mM salt concentration. Within the statistical errors the SLD and US methods agree indicating that the SLD technique is valid. In panel (a) of the figures the calculated PMFs are shown, while the number of ions on the patch and the patch orientation along the center-to-center separation are displayed in panel (b) and (c). As we see in panel (a), the introduction of the patch leads to a considerable short-ranged attraction when compared to the P_0^0 models. Hence, at small separations the standard DLVO potential fails to describe the

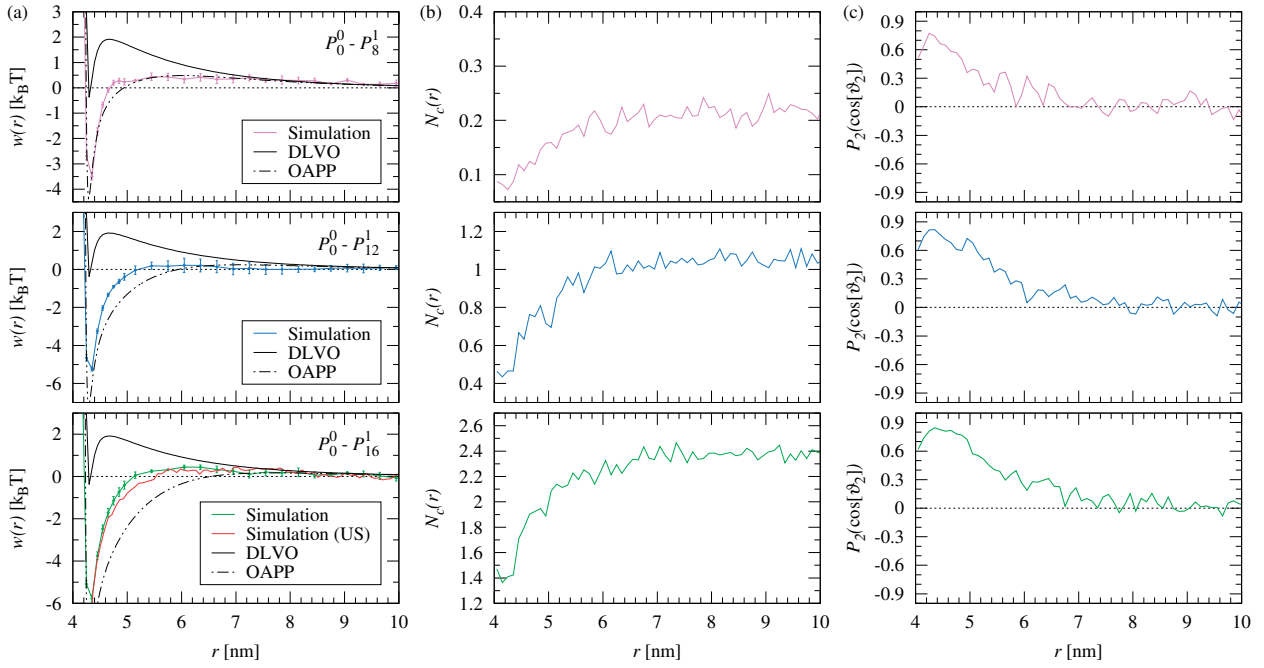


Figure 5.9: Simulation results for $[P_0^0 - P_s^1]$ pairs with $s = 8, 12, 16$ at $c_s = 20$ mM. (a) PMF along the separation r . The black lines represent the DLVO potential (solid) and the OAPP (dashed). The statistical uncertainty of the PMF is depicted by vertical error bars. US denotes a verifying independent umbrella sampling calculation. (b) accumulated ions on the patch, and (c) displays the second Legendre Polynomial of the patch orientation.

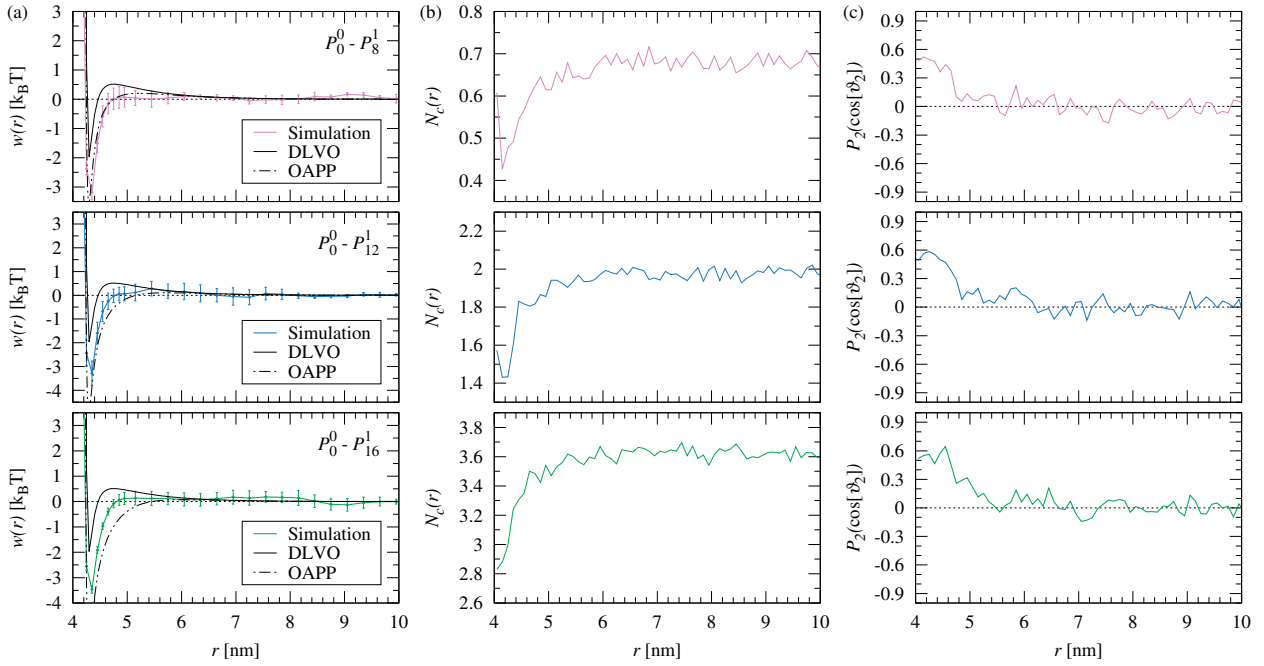


Figure 5.10: The same as in Figure 5.9 but for $c_s = 100$ mM.

orientation-averaged interaction. However, by comparing to the OAPP the agreement within the simulation errors is very good for the globular proteins with lower dipoles P_8^1 and P_{12}^1 even for the relatively low salt concentration of 20 mM. For larger dipoles, P_{16}^1 , the agreement is not satisfactory anymore. Possibly agreement can be enforced by renormalization of monopole charge and dipole moment values as input to the OAPP but we have not attempted such a fitting exercise. Regarding the effect of salt on the PMF we observe that increasing the ionic strength from 20 mM to 100 mM leads to a weaker electrostatic repulsion and higher short-ranged attraction between the globular proteins. Also as expected for a linear electrostatic theory a better performance of the OAPP model is observed for the higher salt concentration. Inspecting the accumulated ions in Figure 5.9 (b) and 5.10 (b) on the patch surface it turns out that at short separations ions are only weakly displaced from the patch surface. This effect becomes stronger with increasing patch charge s and at most *one* ion is released from the patch upon protein binding. In Figure 5.9 (c) and 5.10 (c) the angular orientation $P_2(\cos[\theta])$ of the patch along the center-to-center distance r is represented. At large r there is no favorite alignment of the patch but this changes when the center-to-center distance becomes closer. Around $r \approx 6$ nm the globular proteins begin to align themselves with the positive patch naturally pointing towards the negative protein. Since the orientation of the protein is related to the charge-dipole interactions, the orientation of the patches becomes most pronounced in the attractive regime of the PMF. Moreover, higher salt concentration leads to a weaker alignment.

Figure 5.11 and 5.12 present simulation results of dipole-dipole $[P_s^1 - P_s^1]$ pairs with $s = 8, 12, 16$ for 20 mM and 100 mM ionic strengths, respectively. With growing patch size s , the dipole moment of the globular protein increases (see Table 5.1) which results in a substantial attraction already at intermediate distances and a strong attraction on the order of 10 $k_B T$ at contact. The corresponding PMFs are presented in Figure 5.11 (a) and 5.12 (a). For the lower salt concentration, while DLVO as expected clearly fails, the OAPP model also does not describe the simulated PMFs at 20 mM salt concentration. At $c_s = 100$ mM the agreement with OAPP, within the statistical uncertainty, is good again at least for the smallest dipole protein. We further find that in the bound state the proteins have released 1-2 ions from the patch when compared to the unbound state. The orientational order shown in 5.11 (c) and 5.12 (c) indicates parallel alignment of the patches along the distance vector, as expected for dipolar arrangements, though less than for the monopole-dipole case. A representative snapshot is shown in Figure 5.15 (a).

Results for proteins with antipodally aligned patches are presented in Figure 5.13 and 5.14 for salt concentrations of 20 mM and 100 mM, respectively. The short-range attraction is considerable but its range is smaller than in the dipole-dipole case due to the high quadrupole and relatively small dipole moments of these globular proteins. Hence, for the smaller quadrupole in $[P_8^2 - P_8^2]$ up to a spatial approach larger than 5-6 nm the interaction is dominated by the monopole contribution again as captured by the DLVO potential. The same is not valid anymore for the $[P_{12}^2 - P_{12}^2]$ PMF at 20 mM ionic strength where the quadrupole interac-

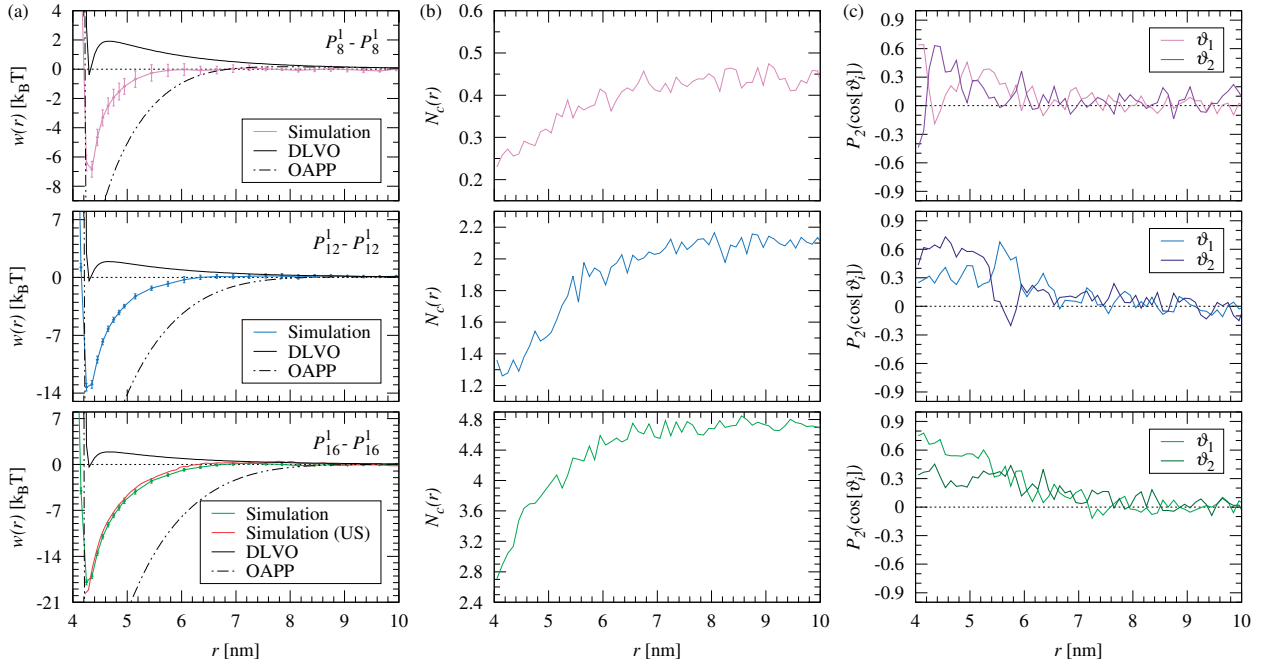


Figure 5.11: Simulation results of two identical proteins $[P_s^1 - P_s^1]$ with $s = 8, 12, 16$ and $c_s = 20$ mM. (a), (b), and (c) are the same as in Figure 5.9.

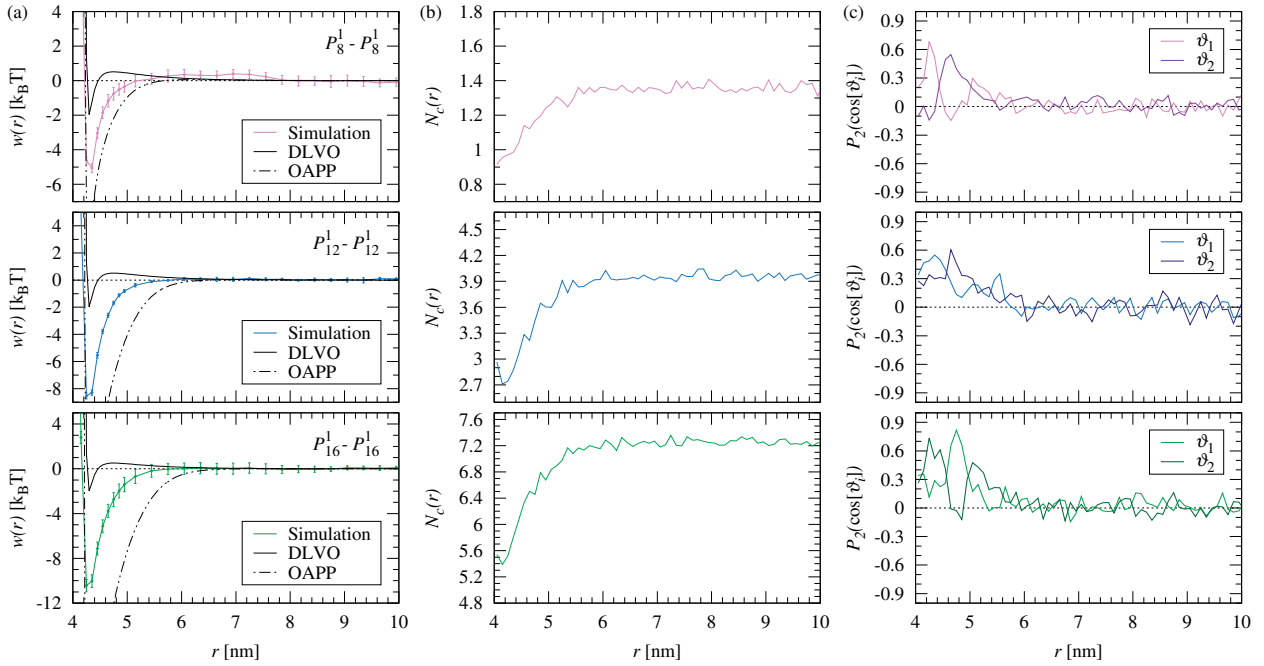


Figure 5.12: The same as in Figure 5.11 but for $c_s = 100$ mM.

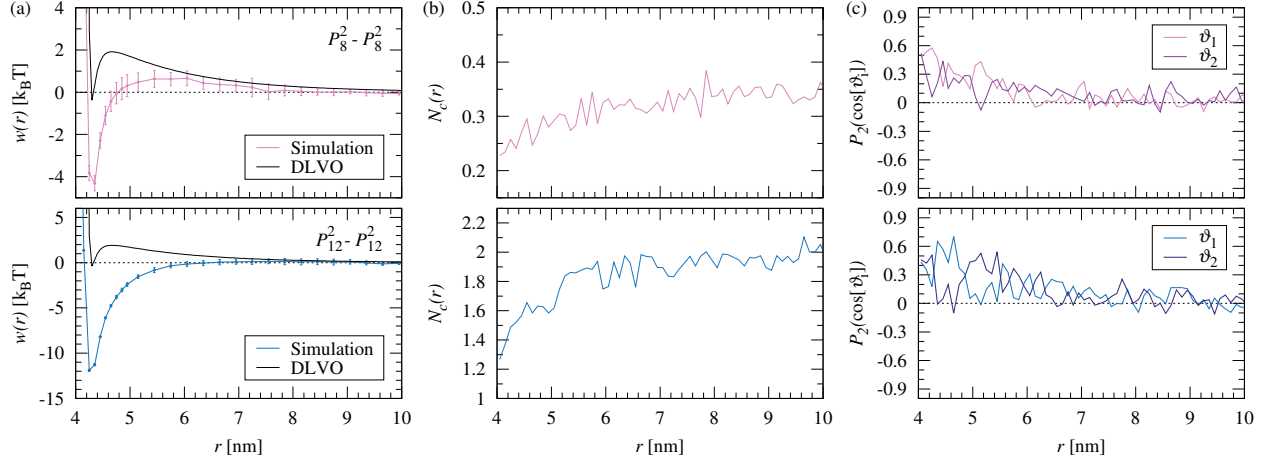


Figure 5.13: Simulation results for $[P_s^2 - P_s^2]$ with $s = 8, 12$, $c_s = 20$ mM and antipodally orientated patches ($m = 2$). (a), (b), and (c) are the same as in Figure 5.9.

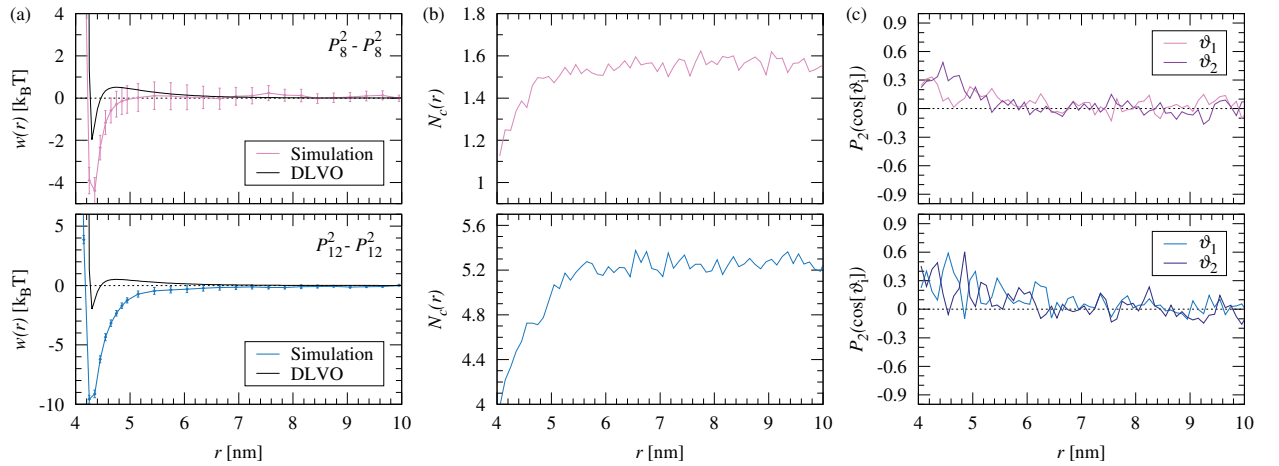


Figure 5.14: The same as in Figure 5.13 but for $c_s = 100$ mM.

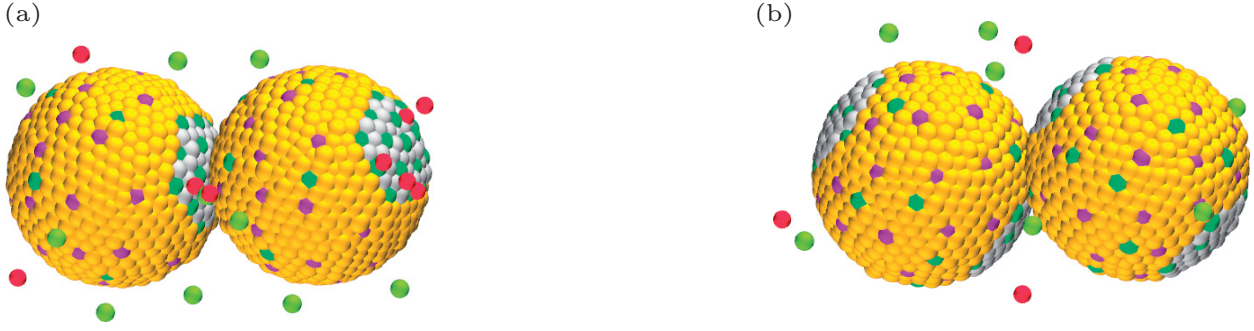


Figure 5.15: Visualization of typical simulation snapshots at contact: (a) $[P_{16}^1 - P_{16}^1]$ and (b) $[P_8^2 - P_8^2]$. Both snapshots are made in an ionic solution of 20 mM. The green colored beads are positively charged ions while the red colored beads are negative ions.

tion is much stronger. The OAPP as employed in this work is not applicable anymore due to the lack of consideration of the quadrupole interactions. At 100 mM ionic strength as shown in Figure 5.14 all the weak long-ranged contributions are entirely screened and the short-ranged effects remain strong and essentially unscreened. Figure 5.13 (b) indicates a release of accumulated patch ions comparable to those found in the systems above. The patch orientation in Figure 5.13 (c) implies a less pronounced patch orientation in distance direction. A representative snapshot is shown in Figure 5.15 (b). The reason for the weaker orientational order as probed by our order parameters is very likely the occurrence of patch orientations perpendicular to the distance vector to satisfy local attraction to the positive patch of the second protein.

5.3 Like-charged protein-polyelectrolyte complexation

In this section, we report on the complex formation between a single PE and like-charged protein depending on different physical parameters. We also provide a simple counterion release/Debye-Hückel model to satisfactorily explain the salt-dependent binding affinity of the formation.

A simple model to combine ionic release and screening effects

An important quantity is the binding affinity of the PE to the patchy protein which in principle is an easily accessible number in experiments through the measurement of equilibrium binding constants [60, 61]. Since we resolve the total PMF along the distance coordinate, the binding affinity can be naturally defined as the difference in free energy of the stable complex versus the separated reference state. Hence, the binding free energy can be written as

$$w_{min}(c_s) = w(r_{min}, c_s), \quad (5.4)$$

where r_{min} is the location of the global minimum of the PMF characterizing the stable complex. This binding affinity is in general a sum of van der Waals, PE chain entropy, and multipolar electrostatic contributions (including ionic entropy effects). However, the first two

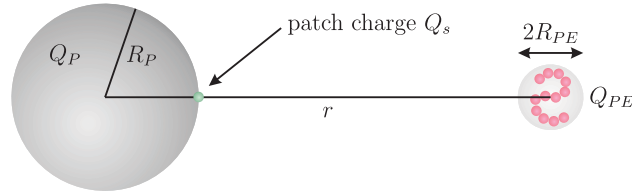


Figure 5.16: Simple electrostatic model for describing the salt concentration dependence of the binding free energy of a protein-PE complex. The PE chain on the right-hand-side is modeled as a charged sphere with effective charge Q_{PE} and effective radius R_{PE} . The simplified globular protein (left-hand-side) has a radius R_P and a negative charge Q_P located in its center, while a point charge with valence Z_s (green spot), representing the positive patch, is located on the surface along the connecting axis.

parts are at least one order of magnitude smaller than the electrostatic one for our systems and will therefore be neglected in our discussion. For the interpretation of the resulting salt concentration dependence of the electrostatic part, we compare our simulations to the classical counterion release mechanism and complement it eventually to include screening effects by mapping our system onto a highly simplified model of an interacting charge-dipole system in the DH limit.

An obvious weakness of the counterion release approach is that it only captures the translational entropy contributions of the ions tightly condensed in the first layer of the PE and protein (see Section 3.1.4). While this is justified for the PE, the picture is not so clear for ions condensing on the charge patch of a weakly curved spherical surface [97, 195, 196]. For the latter, condensation and charge renormalization depends on the sphere size, charge density, and salt concentration. For our protein model parameters, close to physiological ones for globular proteins, we operate in a regime of intermediate $\kappa R \simeq 1$ and small structural charges of the globule and have not found any charge renormalization effects (see Section 5.2.1). Hence, it is not unlikely that the counterion concept can only account for binding effects near the PE, while ions around the patches have to be treated within a conventional ionic-screening framework.

To account for this, we propose a combined counterion release/DH-screening (CR/DH) approach, where we consider the explicit condensation effect only on the PE and treat the rest of the system in a simplified DH picture to treat the effects of screening. The strategy is to map the simulated protein-PE system onto an interacting charge-multipole system and treat it on an analytic Debye-Hückel level. An illustrating sketch is shown in Figure 5.16. In our discussion later we will revolve around the one-patched, dipolar P_{12}^1 type of protein. In our simplified model, therefore the patchy protein has a radius $R_P = 2.0$ nm and a negative charge $Q_P = Z_{PE}e = -20e$ located in its center, while a point charge with valence $Z_s = +12$, representing the positive patch, is located on the surface along the connecting axis. The PE chain is modeled as a charged sphere with effective charge $Q_{PE} = Z_{PE}e$ and effective radius R_{PE} . For such a simplified model, where an extended dipole within a globule (protein) interacts with a monopolar blob (PE), the electrostatic association free energy at contact of

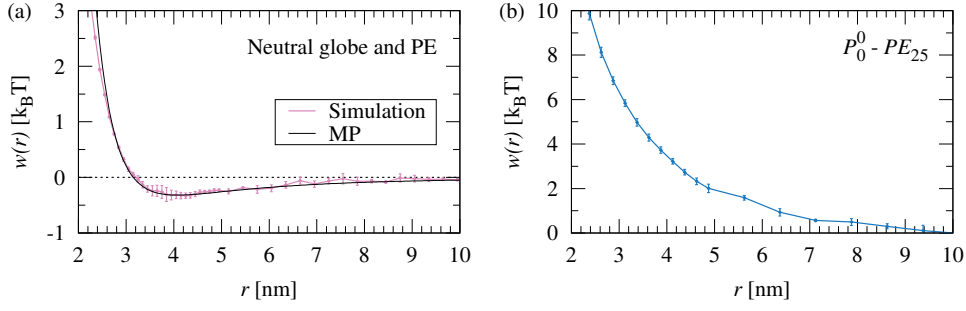


Figure 5.17: (a) Simulated PMF between a fully neutral spherical globule (no beads charged) and a neutral PE_{25} . The black solid line represents a fit by the Mie potential according to Eq. (3.18). (b) PMF profile of a charged $[P_0^0 - PE_{25}]$ complex in an ionic solution of 20 mM.

the two spheres ($r_{min} = R_P + R_{PE}$) can be written down on a Debye-Hückel level as

$$\beta w_{min}(c_s) = \frac{Z_P Z_{PE} \lambda_B}{(R_P + R_{PE})[1 + \kappa(c_s)R_P][1 + \kappa(c_s)R_{PE}]} + \frac{Z_s Z_{PE} \lambda_B}{R_{PE}[1 + \kappa(c_s)R_{PE}]} + \tilde{N} \ln \left[\frac{c_s}{c_{PE}} \right], \quad (5.5)$$

where the first term accounts for screened monopole charge repulsion and the second term effectively describes the screened electrostatic patch-PE attraction, and $\kappa(c_s) = \sqrt{8\pi\lambda_B c_s}$ is the usual inverse DH screening length. The last term is the contribution from the released ions from the PE chain according to the Record-Lohman approach in Eq. (3.16). The effective charge of the PE chain will be taken from the simulations in which the number of condensed counterions is explicitly calculated. The remaining free parameter R_{PE} will be fitted to the results from the simulations of the 'real' protein-PE complex and is expected to be on the order of the radius of gyration of the chain of nanometer size. Note again that the contribution of the configurational rearrangements of the PE on the extended patch surface are not considered in this model, but believed to be small (on the order of a $k_B T$) with respect to the calculated binding affinities in the tens of $k_B T$.

5.3.1 Reference simulations

We start our discussion of the PMFs with two reference cases specified by i) a charge-free system which consist only of a neutral sphere and a short neutral PE_{25} as shown in Figure 5.17 (a) and ii) a homogeneously charged protein such as P_0^0 and a uniformly charged PE_{25} in an explicit ionic solution as depicted in Figure 5.17 (b), respectively. Note again that the PMF is plotted versus the distance between the centers of mass of both molecules. The PMF of the neutral complex exhibits a weak but long-ranged attraction but is otherwise repulsive for short distances. The solid black line represents the Mie potential. It was used to fit the PMF with $n = 5$, $k = 3$, $\sigma^* = 3.15$ nm, and $\epsilon^* = 0.33$ $k_B T$ and shows good conformity. The attraction must be attributed to van der Waals interactions (modeled by the Lennard-Jones interaction between all beads), while the repulsion is due to the entropic penalty from restricting available chain configurations to the PE. As expected, the simulated PMF of the charged $[P_0^0 - PE_{25}]$ complexation at $c_s = 20$ mM in Figure 5.17 (b) is purely

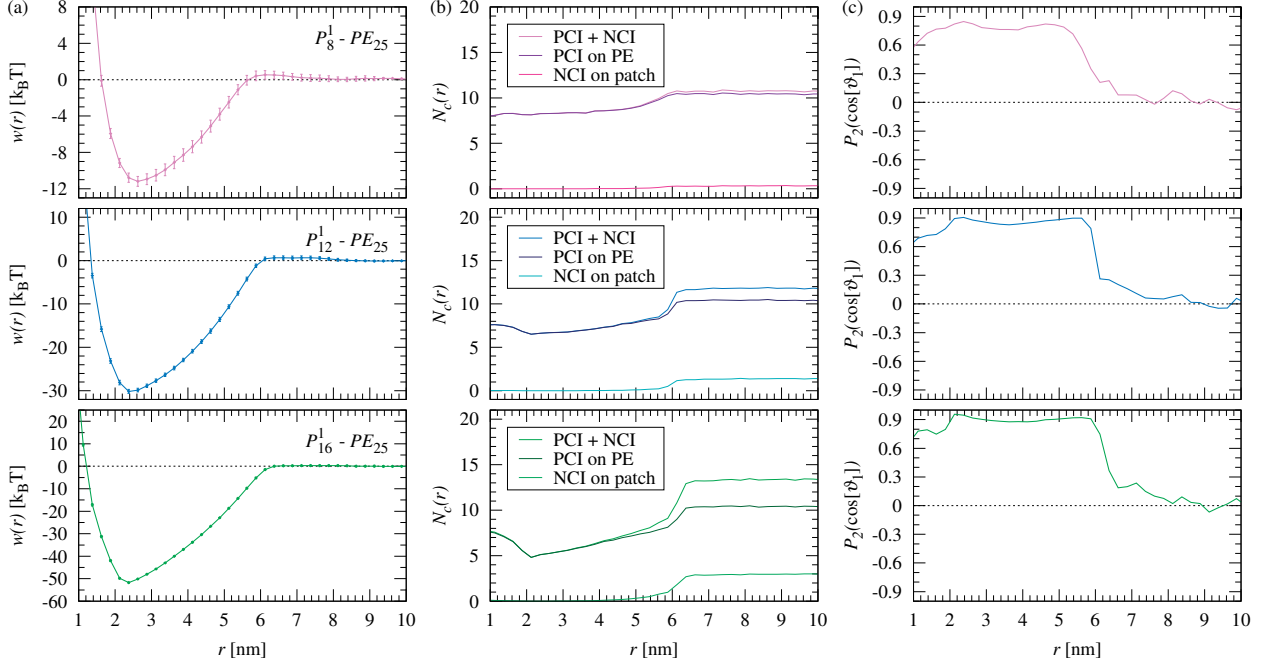


Figure 5.18: Simulation results of $[P_s^1 - PE_{25}]$ complexes with $s = 8, 12, 16$ in an electrolyte concentration of $c_s = 20$ mM. (a) PMF as a function of the distance r of the centers of mass of the patchy protein and PE. (b) Number of condensed ions $N_c(r)$ as a function of r . PCI denotes the number of positively charged ions condensed on the PE, while NCI is the number of negatively charged ions condensed on the protein patch. (c) Patch orientation with respect to the mass centers of the protein and PE displayed via the second Legendre Polynomial.

Table 5.2: Snapshots of different patchy protein-PE complexes at $c_s = 20$ mM and different center of mass distances r . The green colored beads are positively charged ions, while the red colored beads are negative ions.

Complex	Center of mass distance r in nm			
	~ 1.5	~ 2.5	$\sim 5-6$	~ 10
$P_8^1 - PE_{25}$				
$P_{12}^1 - PE_{25}$				
$P_{16}^1 - PE_{25}$				
$P_8^2 - PE_{25}$				
$P_{12}^2 - PE_{25}$				

repulsive due to simple charge repulsion.

5.3.2 Influence of protein patchiness and salinity on complexation

We will now investigate the effect of changing the charge distribution on the surface of the globular protein as well as the ionic strength on the effective interaction in more detail.

Results for one-patched proteins

The results of protein-PE simulations with one patch, P_s^1 , and growing patch charge $s = 8, 12, 16$ at 20 mM salt concentration are shown in Figure 5.18, respectively. The PMFs are now strongly attractive in the tens of $k_B T$ for a wide distance-range except for a small repulsive barrier at around $r \approx 6$ nm. For rising patch charge s (and thus increasing dipole) of the patchy protein the attraction is more pronounced and the barrier vanishes. The insets in Table 5.2 show typical configurations of the protein-PE complex in the stable bound state at $r \approx 2.5$ nm. Here, we can see that almost the entire PE chain is adsorbed on the patch in the bound state. Configurations for other distances are also displayed in Table 5.2. For $r \approx 10$ nm the PE is desorbed and exhibits relatively stiff, rod-like configurations. For a closer distance of about $r \approx 6$ nm the PE is able to reach out and touch the attractive patch; this is reflected in the onset of attraction in the PMFs in Figure 5.18 (a). The distance $r \approx 1.5$ nm in Table 5.2 corresponds to the closest distance approachable in our SLD simulations and is, according to the PMF, energetically strongly penalized. Here, the PE embraces the globular protein to fulfill the external force constraint in the SLD that the PE center of mass is close to that of the globular protein.

The number of negatively charged ions (NCI) as well as positively charged ions (PCI) condensed on the protein patch and on the PE for the $[P_s^1 - PE_{25}]$ simulations are shown in Figure 5.18 (b). At large separations the number of condensed ions is fairly constant, while the absolute value increases with growing patch charge s . When the PE begins to adsorb on the patch, $r \lesssim 6$ nm, counterions and coions on both molecules are simultaneously released, their number increasing the closer the associating partners come to each other. Hence, protein-PE complexation is accompanied by a significant release of condensed ions mostly stemming from the PE. A detailed analysis on numbers will follow in the next paragraph. In Figure 5.18 (c) the patch orientations along the separation r with respect to the distance vector are presented. For large distances ($r > 7$ nm) no correlation effect is observable, however, when the PE begins to attach to the patch with its first monomer, a favorite orientation of the patch towards the PE immediately locks in. This orientation persists until the PE is completely attached to the patch. For very small distances $r \lesssim 2$ nm the orientation correlation weakens due to the (forced) embracing of the PE around the globular protein.

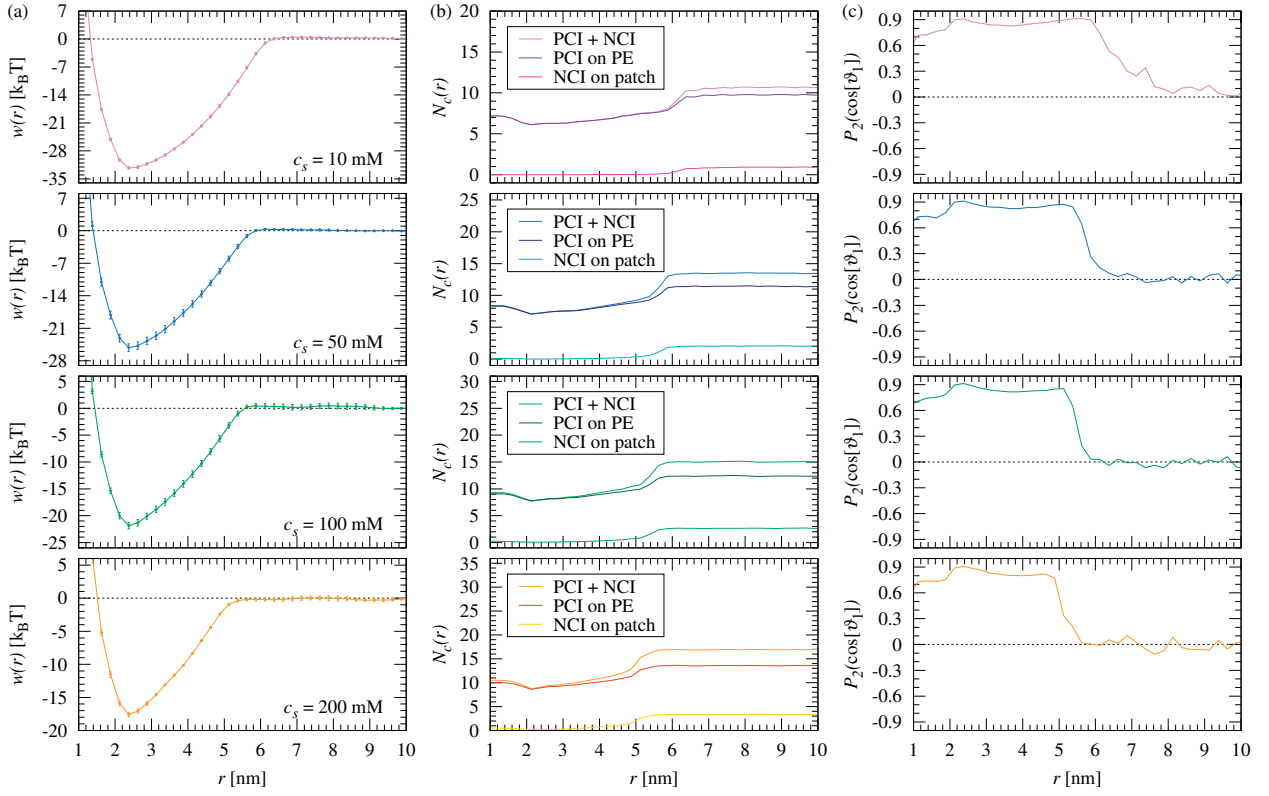


Figure 5.19: Simulation of $[P_{12}^1 - PE_{25}]$ at different salt concentrations ranging from 10 mM to 200 mM. (a), (b), and (c) are the same as in Figure 5.18.

Effects of added salt

The influence of the ionic strength on the PMF and the ion release is investigated based on the $[P_{12}^1 - PE_{25}]$ complex. The results for salt concentrations between 10 mM and 200 mM are presented in Figure 5.19. First of all, it is evident that the attraction of the PMFs as depicted in Figure 5.19 (a) decreases with increasing salt concentration c_s since the electrostatic interaction between the patch and the PE monomers is more screened. A further effect of the screening is that the beginning of the attraction (adsorption of the PE head monomer to the patch) is shifted to shorter separations with increasing c_s due to a lesser stiffness of the PE chain. The corresponding number of condensed ions N_c is shown in Figure 5.19 (b), respectively. It is clear that increasing the ionic strength leads to more condensed ions on both molecules which can be unambiguously verified from the trajectories. The average number of released ions is between 4.4 for the lowest salt concentration and up to 7.8 for the highest salt concentration. The position of the N_c -minimum roughly coincides with the PMF minimum, *i.e.*, there is a clear correlation between ion release and attraction for all salt concentrations. The patch orientation behavior, *cf.* Figure 5.19 (c), does not exhibit any marked salt concentration behavior, apart from a shorter correlation range for increasing c_s due to the shorter attraction range discussed above.

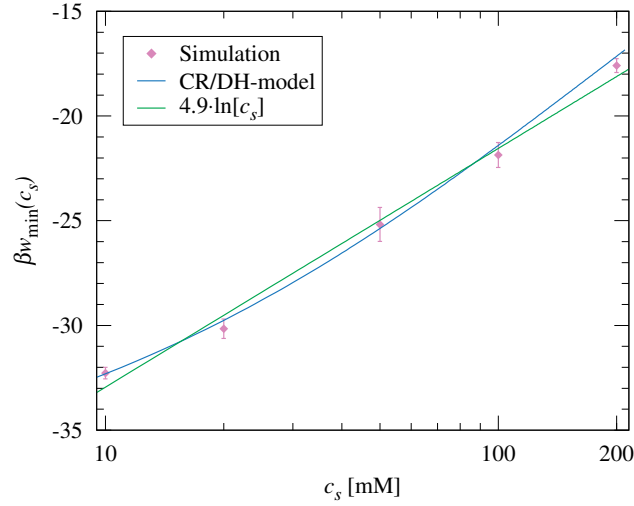


Figure 5.20: The binding affinity represented by the minimum value of the PMF, w_{\min} , of the $[P_{12}^1 - PE_{25}]$ complex as a function of the salt concentration c_s (violet symbols) in a lin-log plot. The linear blue solid line is a fit according to the fit function $\beta w_{\min}(c_s) = \tilde{a} + \tilde{N} \ln[c_s]$ with $\tilde{a} = -44.3$ and $\tilde{N} = 4.9$. The green solid line is a fit to the combined CR/DH model around Eq. (5.5), see text for explanation.

Salt concentration of the binding affinity

To analyze the correlation between the free energy of binding w_{\min} (the 'binding affinity') and salt concentration in more detail, we plot in Figure 5.20 the variation of the PMF minimum with the logarithm of the salt concentration $\ln[c_s]$. As motivated by our discussion on ion release effects around Eq. (3.16) in Section 3.1.4, we have fitted the data with a function of the form $\beta w_{\min}(c_s) = \tilde{a} + \tilde{N} \ln[c_s]$. The result is also shown in Figure 5.20 and represents actually a very satisfactory fit to the data with $\tilde{a} = -44.3$ and $\tilde{N} = 4.9$, implying that every time an average of 4.9 ions are released upon complexation, independent of salt.

We go further into the details of the counterion release analysis by actually counting ions and evaluating the free energy changes corresponding to ions released from patch and PE as defined in Eq. (3.17), respectively. The results are summarized in Table 5.3. First we would like to direct the attention to the value of N_+^{apart} , the number of condensed ions on the PE chain in the isolated state. With a Manning parameter of $\Gamma = 1.78$ we expect $N_{\text{mon}}(1 - \Gamma^{-1}) = 10.9$ counterions to be condensed right at the chain. As we see in Table 5.3, we indeed find numbers between 9.7 at the lowest salt concentration up to 13.6 at the highest c_s , coinciding with the prediction but also exhibiting a noticeable salt dependence. The number of released ions from the chain upon complexation, ΔN_+ only slightly depends on salt, increasing from roughly 3.5 to 4.7. This also agrees well with a prediction that $Z_s \cdot N_{\text{mon}} = 5.1$, with the binding patch valence $Z_s = 12$, should be released from the PE upon binding. Hence, the ion-PE system behaves as expected and shows a very robust ion condensation and release effect.

In contrast to the ionic behavior at the PE, the number of accumulated and released ions on the protein patch, ΔN_- , increases from about 1 to 3.2 in the considered concentration range, *i.e.*, a much stronger salt dependence of the number of released ions is found at the patch. The individual free energy contributions w_{patch} and w_{PE} , evaluated by Eq. (3.17),

Table 5.3: A summary of the values of the PMF minimum w_{\min} with respect to the salt concentration c_s and the number of condensed ions when the patchy protein and PE are apart (N_i^{apart}) and in the complexed state (N_i^{min}) taken from the data for $[P_{12}^1 - PE_{25}]$ in Figure 5.19 and 5.18. The difference of condensed ions is then $\Delta N_i = N_i^{\text{apart}} - N_i^{\text{min}}$. The concentration c_{patch} is the local density of negative ions on the protein patch. For c_{PE} in Eq. (3.17) we used a constant 3.5 M as measured in our simulation.

c_s [mM]	w_{\min} [k _B T]	Patch					PE			
		N_-^{apart}	N_-^{min}	ΔN_-	c_{patch} [M]	βw_{patch}	N_+^{apart}	N_+^{min}	ΔN_+	βw_{PE}
10	-32.3	0.96	0.00	0.96	1.36	-4.7	9.69	6.24	3.45	-20.2
20	-30.3	1.41	0.00	1.41	1.99	-6.5	10.39	6.62	3.77	-19.4
50	-25.3	2.09	0.02	2.07	2.96	-8.5	11.35	7.22	4.13	-17.5
100	-21.9	2.65	0.05	2.60	3.75	-9.4	12.42	7.93	4.49	-16.0
200	-17.6	3.31	0.15	3.16	4.68	-10.0	13.59	8.92	4.67	-13.4

are also shown in Table 5.3. Attractive contributions from the patch are actually growing (from about -5 to -10 k_BT) for increasing c_s due to the significant increase of accumulated ions on the patch. In contrast, the contribution from the PE is decreasing (from about -20 to -13 k_BT) because the number of condensed ions stays relatively constant. Interestingly, the sum of both contributions only shows little salt dependence and is about -25 ± 1 k_BT, while the simulated free energy is about 14 k_BT from ca. 32 k_BT at 10 mM to ca. 18 k_BT at 200 mM. Clearly, the approach Eq. (3.17) cannot satisfactorily describe the values and trends of the binding affinity with salt concentration. We believe that this must be assigned to a missing counterion condensation mechanism on the protein patch, where only conventional charge screening effects apparently play a role. We note that we have experimented with the cut-off radii that define the condensed layer around the patch in a reasonable range but have not found any qualitative improvement of the prediction.

The charge screening effect should be captured in our combined CR/DH model, Eq. (5.5), as previously introduced. A best fit is also presented in Figure 5.20. Since we find on average about 8 ions still condensed on the complexed PE, the PE charge Q_{PE} was fixed by an effective valence of $-25 - (-8) = -17$. The number of condensed ions \tilde{N} on the PE was fixed to 4.9 as found in the Record-Lohman fit. The only remaining fit parameter is the effective size of the adsorbed chain, R_{PE} . For the best fit we find $R_{PE} = 1.17$ nm. This value is indeed close to the patch size and to the mean radius of gyration of about 1.3 nm in the bound state (*cf.* Figure 5.21). As we can see in Figure 5.20 the fit describes the simulated data very well with essentially only one fit parameter of reasonable value. It is interesting to see that the DH part of the theory induces some curvature to the fitted curve in addition to the linear logarithmic behavior in this lin-log plot. Actually such a curvature can also be noticed made by the simulation data points. Hence, we have strong indications that the combined CR/DH model captures the right physics in the system, in particular the fact that the condensed ions on the PE *only* play the decisive role in the counterion release framework.

In a recent experimental and computational study of Yu *et al.* [Paper V], it was found that counterion release occur even in more complex protein models and essentially contribute to the binding affinity. This also justifies the use of our patchy protein models.

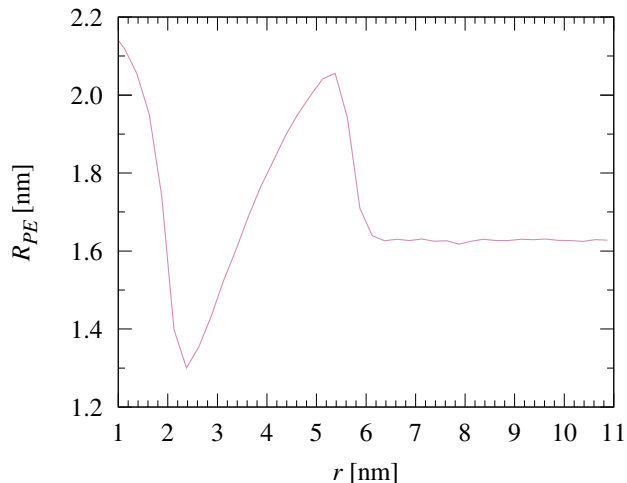


Figure 5.21: The mean radius of gyration R_{PE} of the 25meric PE chain resolved versus the center of mass distance to the P_{12}^1 protein at a salt concentration of 50 mM. The PE bulk value of the size $R_{PE} \approx 1.6$ nm, increases at intermediate distances ($r \approx 5$ nm), where the chain stretches out, to a value of $R_{PE} \approx 2.1$ nm and collapses to $R_{PE} \approx 1.3$ nm in the bound state ($r \approx 2.4$ nm).

Results for two-patched proteins

Figure 5.22 shows results of protein-PE complexes with two ($m = 2$) antipodally aligned patches in an ionic solution of 20 mM. Despite an additional patch, the simulated PMFs between $[P_s^2 - PE_{25}]$ in Figure 5.22 (a) are less attractive compared to $[P_s^1 - PE_{25}]$ systems with $s = 8, 12$ (see Figure 5.18). Furthermore, a distinct shift of the global minimum to a larger separation is present. A possible explanation could be that in patchy protein models with $m = 2$ the negative charges are denser distributed on the surface leading to a raised repulsive electrostatic interaction and a reduced attraction between PE monomers and the patchy protein. In counting the condensed ions N_c on the both molecules again, ion release is found as depicted in Figure 5.22 (b) where ions are mainly released from the PE. As in the one-patch systems, the attraction is accompanied by a strong orientation of the interacting attractive patch to the PE, see Figure 5.22 (c). The orientation is reversed at very small distances $r \lesssim 1.8$ nm; but note that those are improbable to observe in equilibrium anyway due to the high free energy penalty. Hence, for the short PE_{25} chain that cannot reach to the second patch of the protein, the results are qualitatively similar than for the analogous one-patch system, albeit with considerably less attraction.

5.3.3 Influence of polyelectrolyte chain length on complexation

We will now see that a longer PE chain can interact with both patches simultaneously and lead to qualitatively very different PMFs.

The simulated PMFs of complexation of the two-patched proteins with the longer PE chain, $[P_{12}^2 - PE_{50}]$, simulated at different salt concentrations ranging from 20 mM to 200 mM are presented in Figure 5.23 (a). In stark contrast to the shorter chain, we now observe a two-step PE adsorption to the patchy protein with a second but metastable attraction minimum at $r \approx 4.5$ nm for the smallest salt concentration, decreasing to $r \approx 3.5$ nm for

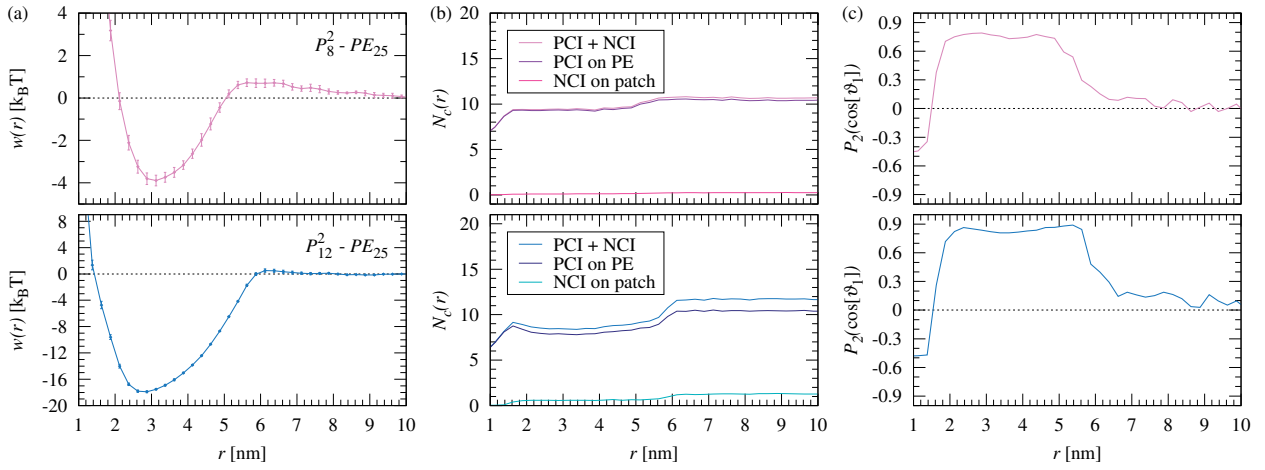


Figure 5.22: Simulation results of $[P_s^2 - PE_{25}]$ complexes with $s = 8, 12$ at $c_s = 20$ mM. (a), (b), and (c) are the same as in Figure 5.18.

the largest salt concentration. As we see from the graphical snapshots in Table 5.4, the metastable minimum at $r \approx 4.5$ nm corresponds to binding configurations where the PE is attached solely to one of the two patches. The global minimum is now shifted towards much smaller distances $r \approx 1.5$ nm when compared to the one-patched systems and shorter chains. The corresponding binding configurations are also summarized in Table 5.4. By fully embracing the globular protein, extended parts of both the head and the tail of the chain can now simultaneously interact with both of the patches, while the center of mass of the chain is very close to that of the globular protein. The global and local minima are separated by a free energy barrier at $r \approx 2.5 - 3$ nm. The barrier must be attributed to the electrostatic repulsion between one of the loose ends of the PE (while the other is attached to one patch) and the negative (un-patched) parts of the globular protein when the PE attempts to closely embrace the globular protein before being able to attach to the second patch. Regarding the number of released ions we find that the two-state PMF behavior is also reflected by a two-step release of ions as shown in Figure 5.23 (b). The orientation of the corresponding patch vector versus distance is given in Figure 5.23 (c), respectively. We again observe the strong patch alignment induced by PE binding for larger separations as in the previous cases. In addition, due to the large conformational change of the complex at short separations, when crossing from the metastable PMF minimum to the global one, the orientation drastically changes from parallel alignment of patch-PE to antiparallel alignment with the PE fully embracing the globular protein.

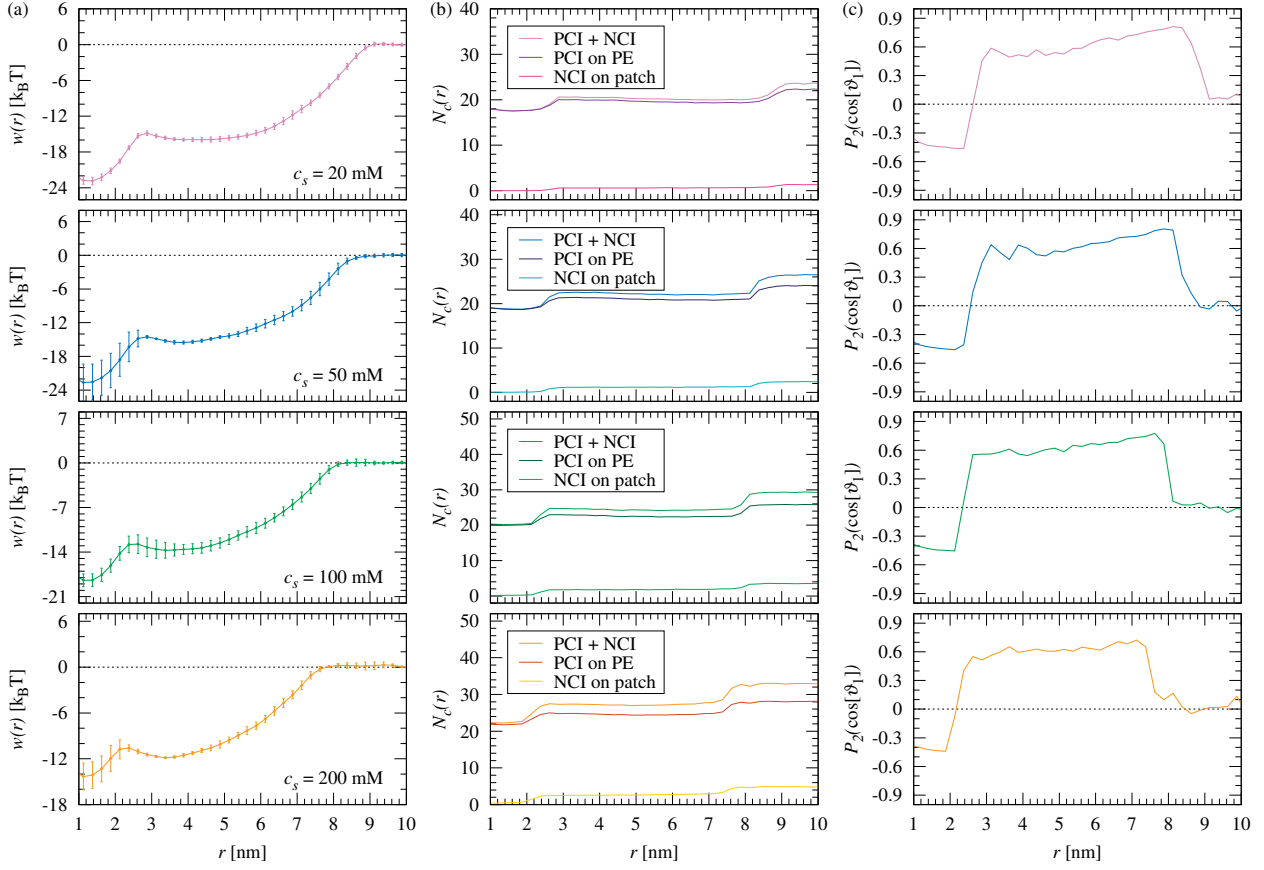


Figure 5.23: Simulation results of $[P_{12}^2 - PE_{50}]$ complexes at salt various concentrations c_s . (a), (b), and (c) are the same as in Figure 5.18.

Table 5.4: Snapshots of $[P_{12}^2 - PE_{50}]$ complexes at various salt concentrations c_s and different center of mass distances r . The green colored beads are positively charged ions, while the red colored beads are negative ions.

c_s [mM]	Center of mass distance r in nm			
	~ 1.5	~ 4.5	$\sim 7-9$	~ 10
20				
50				
100				
200				

5.4 Protein uptake by a polyelectrolyte brush

Before the focus is put on the simulation results, we note that all systems under consideration have a slab geometry wherefore all calculated quantities are resolved only in the z -direction, that is, perpendicular to the grafting surface. An illustrative representation of the simulation box and the procedure of the protein uptake by a PE brush is depicted in Figure 5.24. Furthermore, we aim to compare the simulated PMFs with the outcomes of a simple approach which is presented in the following.

Simplified model for the interaction between a protein and PE brush

A suitable approach for modeling and characterizing the interaction between a globular protein when approaching and in entering a PE brush layer may be given by van der Waals and electrostatic forces through the ansatz

$$U_{\text{EV/LOE}}(z) = U_{ev}(z) + U_{mc}(z) + U_{dc}(z). \quad (5.6)$$

The first term $U_{ev}(z)$ on the right-hand-side represents a polynomial fit of fifth order which accounts for contributions arising from steric and van der Waals interactions. In particular, $U_{ev}(z)$ is obtained by fitting the PMF of a completely neutral globular protein interacting with a neutral PE brush. The leading order electrostatic interaction terms are defined by

$$U_{mc}(z) = Z_P \cdot \Phi(z), \quad (5.7)$$

$$U_{dc}(z) = -\mu_P \cdot |E(z)|, \quad (5.8)$$

and characterize the monopole and dipole contribution, respectively. $\Phi(z)$ and $E(z)$ are the electric potential and field across the simulation box in z -direction and are determined from the density profiles through Poisson's equation. μ_P is the dipole moment of the protein. In the further course, this excluded volume/leading order electrostatics approach is referred to as the EV/LOE model.

Analogously to Section 3.1.4, the gain in translational entropy of released ions during the uptake of a protein by a PE brush is expressed by

$$\beta w_{ion}(z) = \{\Delta N_- - N_-(z)\} \ln \left[\frac{c_s}{c_{\text{patch}}} \right] + \{1 - \Gamma^{-1}\} N_+(z) \ln \left[\frac{c_s}{c_B} \right]. \quad (5.9)$$

Here, ΔN_- denotes the number of negatively charged ions released from the positive patch. $N_-(z)$ is the distance-resolved number of negatively charged ions accumulated on the positive patch and c_{patch} is the same as defined in Section 5.3.2. $N_+(z)$ is the number of positively charged ions condensed on the negative PE monomers along the z -direction. Thus, the term $\{1 - \Gamma^{-1}\} N_+(z)$ specifies the number of released positively charged ions from the PE chains/monomers when the globular protein enters into the PE brush layer. c_B is the concen-

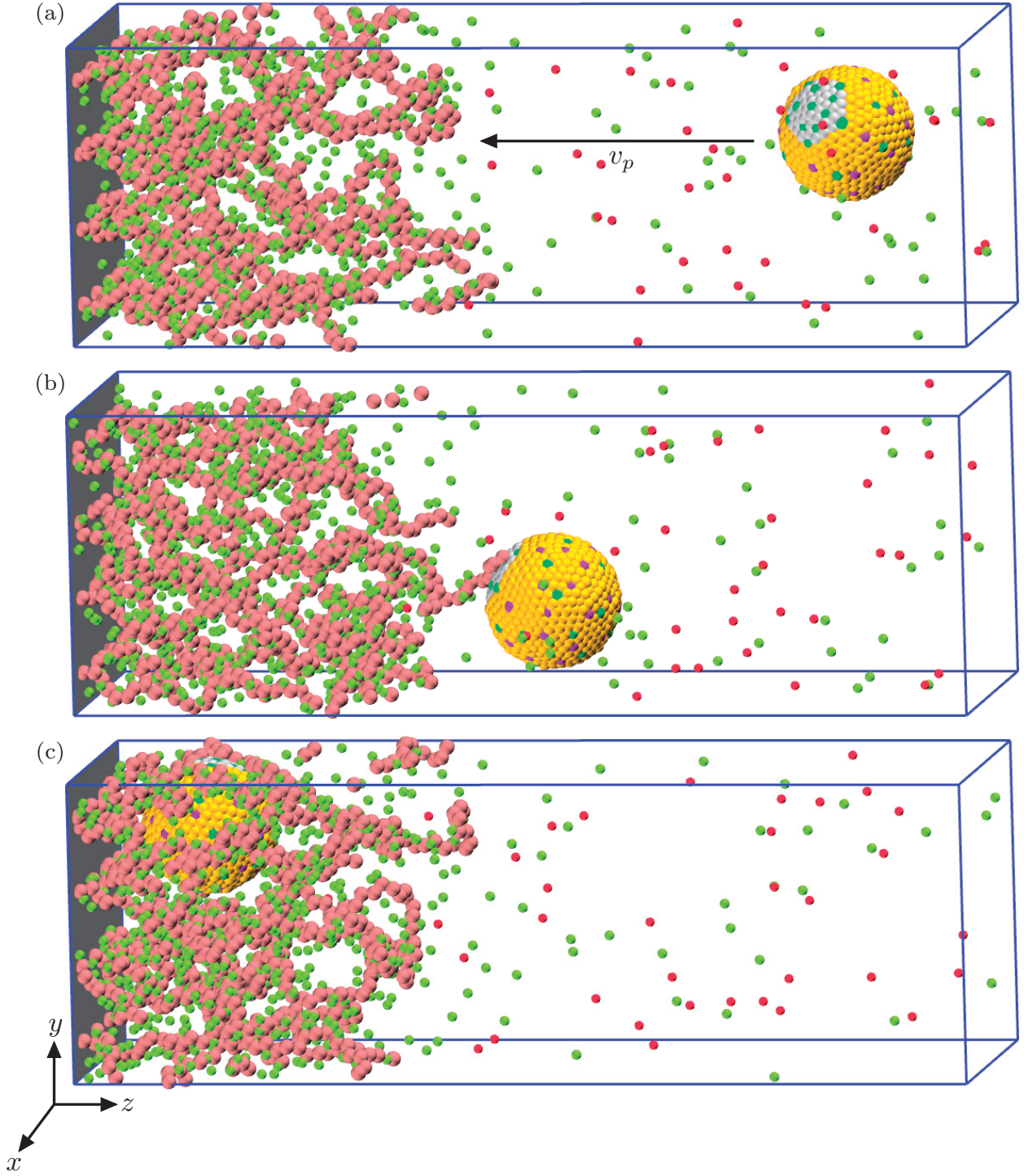


Figure 5.24: Simulation of protein uptake by a planar PE brush confined in slab geometry. At the beginning (a) the protein is situated in the bulk region which is moved with a constant pulling rate v_p towards the brush surface (b), and then further into the brush layer (c).

tration of condensed ions in the immediate vicinity of the PE chains and will be determined in the next section. In contrast to Eq. (5.5), Eq. (5.9) explicitly accounts for the number of released ions from the protein patch. We also expect that Eq. (5.6) together with Eq. (5.9) describe the total binding affinity, that is, the minimum value of the PMF.

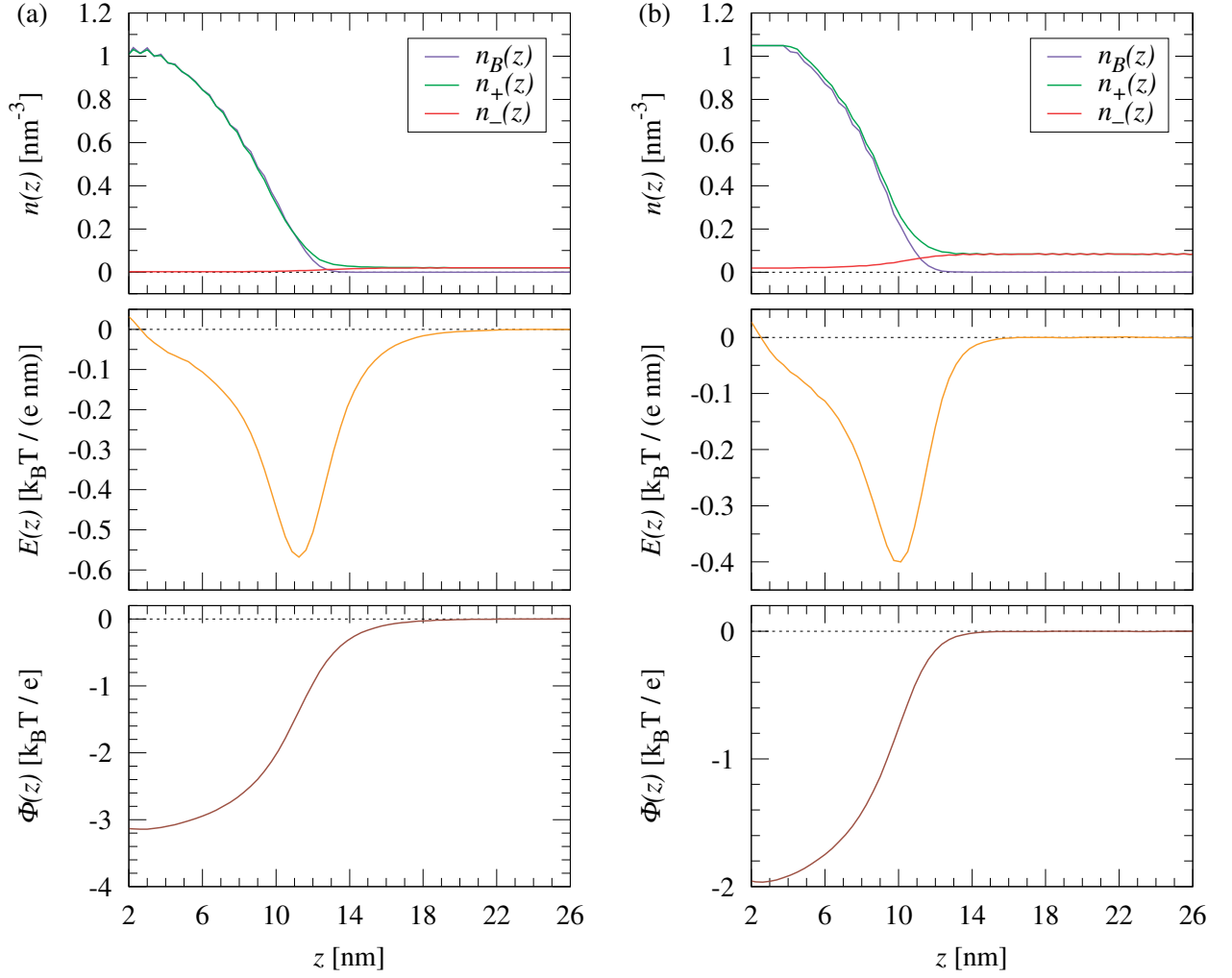


Figure 5.25: Density profiles, electric field and potential of an isolated polyelectrolyte brush at (a) $c_s = 20$ mM and (b) $c_s = 100$ mM.

5.4.1 Reference simulations

We first present an analysis of the density profiles and electrostatic properties of an isolated PE brush at a low and high salt concentration, while the PMFs for two fundamental reference cases are discussed afterwards.

Isolated polyelectrolyte brush

Obviously, the PE monomer density profiles $n_B(z)$ at ionic strengths of 20 mM and 100 mM in Figure 5.25 (a) and (b) show a monotonically decreasing function of the distance from the grafting surface which quickly converge to zero in the bulk region. Comparing the PE monomer density profiles together, it is striking that for the low salt concentration, the brush height is a bit smaller, while the brush thickness is slightly wider. The counterion profiles $n_+(z)$ closely follow the brush density profiles in the brush layer indicating that virtually all counterions are confined within the brush and thus lead to an electrostatic neutralization of the PE brush. This result is in accordance with theoretical predictions, *e.g.* from reference [197]. However, at $c_s = 100$ mM the $n_+(z)$ profile is marginally higher than

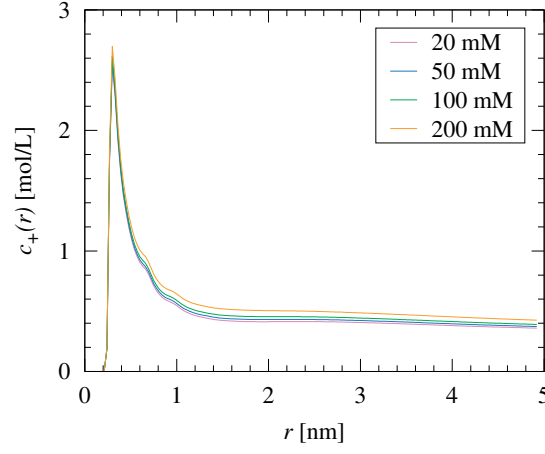


Figure 5.26: The radial concentration profiles of positive ions around single PE monomers at different salt concentrations.

the $n_B(z)$ profile inside the brush layer. Although this points to an overcharged brush, this is balanced by a small number of coions $n_-(z)$ within the brush layer. Both the counterion and coion profiles converge to their respective concentration values in the bulk region. From the density profiles it is possible to calculate the electric field $E(z)$ and potential $\Phi(z)$ of the system via Poisson's equation by means of integration. Hence, the thickness of the brush layer may be approximately estimated from the minimum position of the electric field. We find that the brush thickness is about 11 nm at 20 mM and roughly 10 nm at 100 mM where the electric field takes values of $-0.6 \frac{k_B T}{e \text{ nm}}$ and $-0.4 \frac{k_B T}{e \text{ nm}}$, respectively. The electrostatic potential is strongly negative through the brush layer and saturates to zero in the bulk region. Near the grafting surface, it reaches $-3.1 \frac{k_B T}{e}$ at the low ionic strength and $-2 \frac{k_B T}{e}$ at the higher ionic strength.

Figure 5.26 presents the radial concentration of the positive ions around single PE monomers for ionic strengths ranging from 20 mM to 200 mM. If we define an ion condensation layer with a thickness of 0.4 nm and average over all salt concentrations between $r = 0.2$ nm and 0.4 nm results in a concentration of $c_B = (1.76 \pm 0.05)$ M. Indeed, this value corresponds to the concentration of positive ions condensed on the PE chains and according to Eq. (5.9), it will be used later to determine the gain in translational entropy of released ions when the protein enters into the brush layer.

Reference systems

Figure 5.27 specifies two reference cases by i) a system consisting only of a neutral globule and a PE brush and ii) a patchless protein interacting with a like-charged PE brush at two different salt concentrations. From the PMF of the neutral system it can be recognized that the pulling of the globule into the PE brush leads to a rising van der Waals attraction up to $-1 k_B T$ at $z \approx 10$ nm, while the repulsion found in the brush layer stems from excluded volume interactions between all beads in this region. The solid black line in Figure 5.27 (a) represents a polynomial fit of fifth order to the simulated PMF which accounts for $U_{ev}(z)$ in the EV/LOE model. The simulated PMF of the $[P_0^0 - B_{50}]$ system at $c_s = 20$ mM

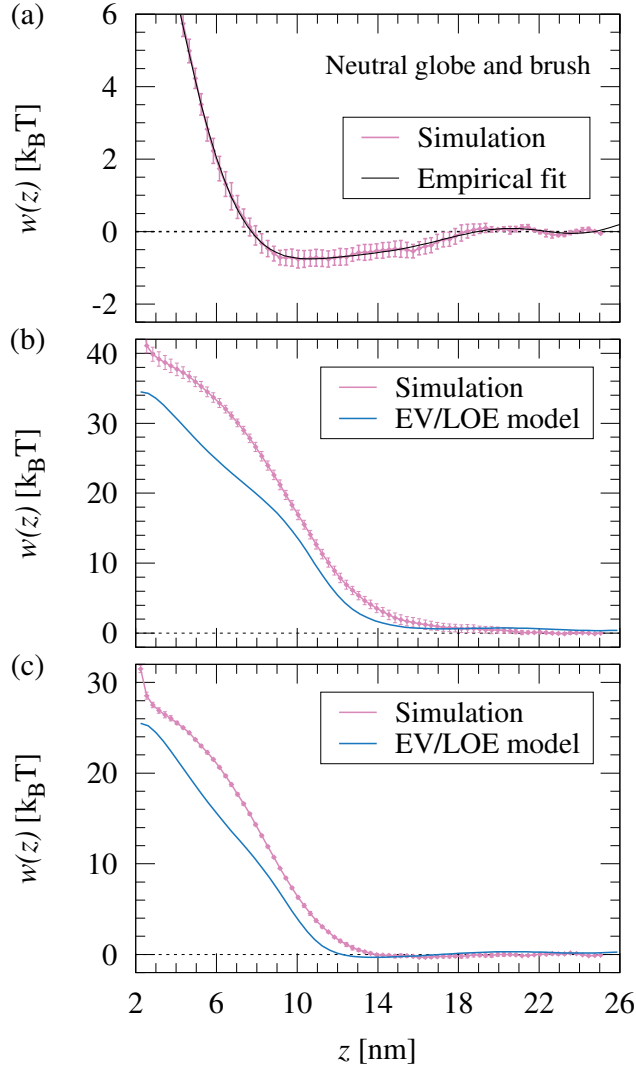


Figure 5.27: Results from reference simulations. (a) PMF between a fully neutral globule and a PE brush. The solid black line represents a polynomial fit of fifth order. (b) and (c) simulated PMF profiles for $[P_0^0 - B_{50}]$ at 20 mM and 100mM salt concentrations, respectively.

and $c_s = 100$ mM salt concentrations in Figure 5.27 (b) and (c) reveals a purely repulsive interaction between the two constituents. Indeed, the favorable electrostatic interactions of the PE monomers with the positive discrete charges on the protein surface are too weak in order to mediate attractions in the PMFs which is why a remarkable repulsion arises in the brush layer. The effect of the salt is also obvious and weakens the repulsion almost by 10 $k_B T$ when increasing the ionic strength from 20 mM to 100 mM. The EV/LOE model which is represented by the solid blue line in the respective figures shows qualitatively the same trend as the PMFs. However, it underestimates the simulated PMFs because contributions from the ions and effects due to charge heterogeneity on the protein surface are not yet captured by the EV/LOE model which we believe is of significant importance.

5.4.2 Uptake of like-charged patchy proteins

We now turn to the simulations of a PE brush interacting with a like-charged patchy protein. Our particular interest is to investigate how patchiness and ionic strength affects the PMF

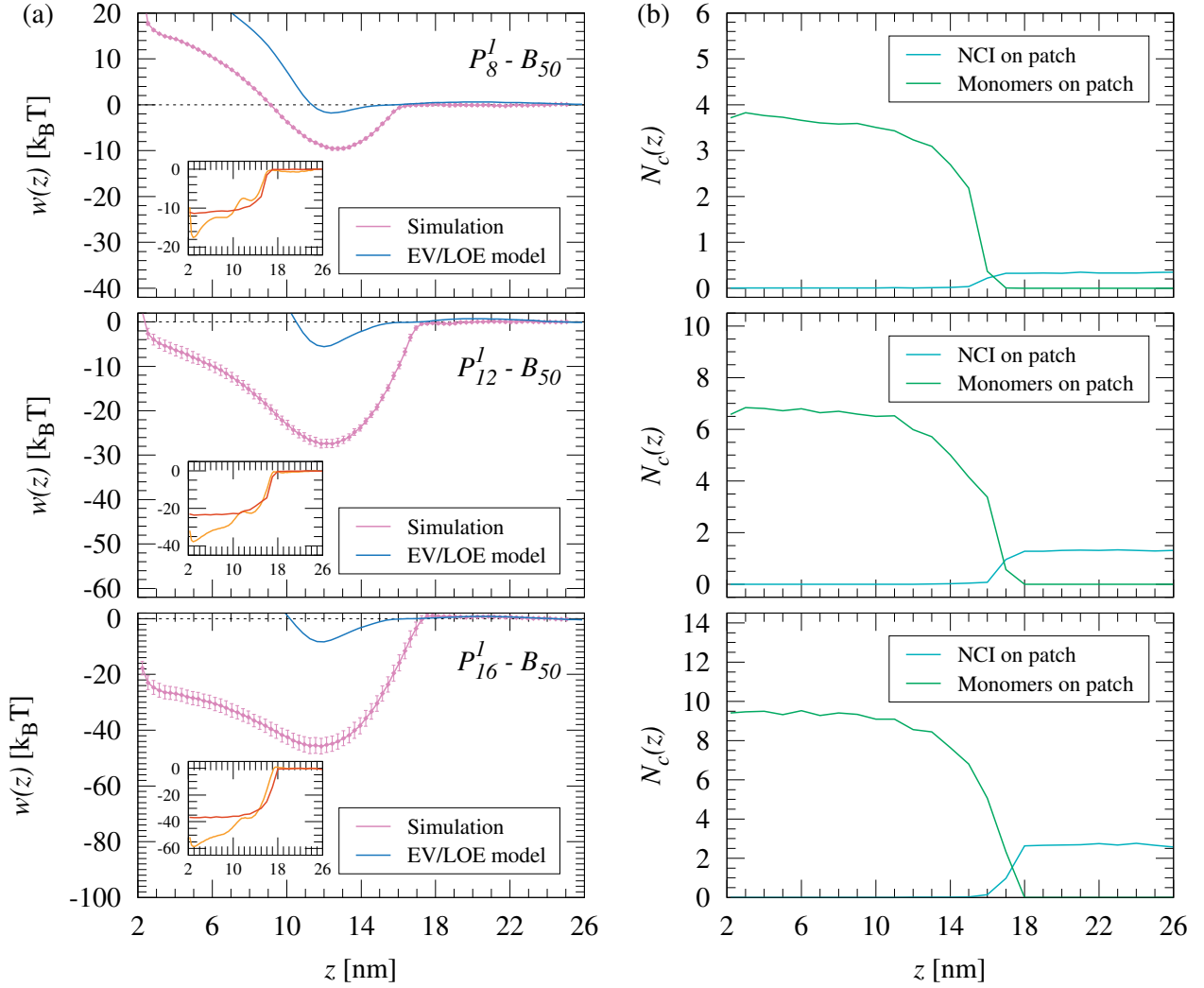


Figure 5.28: (a) Simulated PMFs $w(z)$ for $[P_s^I - B_{50}]$ with $s = 8, 12, 16$ at $c_s = 20$ mM. The insets show the difference between the simulated PMF and EV/LOE model (orange solid line) and the gain in translational entropy of the released ions (brown solid line). (b) Number of counted ions $N_c(z)$ on the patch (denoted by "NCI on patch" in the legend and by $N_-(z)$ in Eq. (5.9)) as well as the contacts of PE monomers with the patch (denoted by "Monomers on patch" in the legend while the number of released positively charged ions is given by $\{1 - \Gamma^{-1}\} N_+(z)$ as defined in Eq. (5.9)) as a function of z .

when steering the protein from the bulk solution into the brush layer. We also devote special attention to the counterions on the patch surface as well as to the contacts of the PE monomers with the positive patch.

Interaction between a PE brush and one-patched proteins

In Figure 5.28 (a) and 5.29 (a) we present PMFs for the uptake of a patchy protein by a like-charged PE brush at ionic strengths of 20 mM and 100 mM, respectively. By increasing the patch size from $s = 8$ to $s = 16$ the attraction in the PMFs at $z \approx 12$ nm rises from initially -10 k_BT to -45 k_BT for $c_s = 20$ mM and from -8 k_BT to -40 k_BT for $c_s = 100$ mM. The decrease of the attraction at the higher salt concentration is attributable to a stronger electrostatic screening of the interaction between the two binding partners. Another conspicuous feature is the shape of the PMF curve. While for $s = 8$ the PMF becomes repulsive when the protein penetrates deeply into the brush layer, it slowly rises

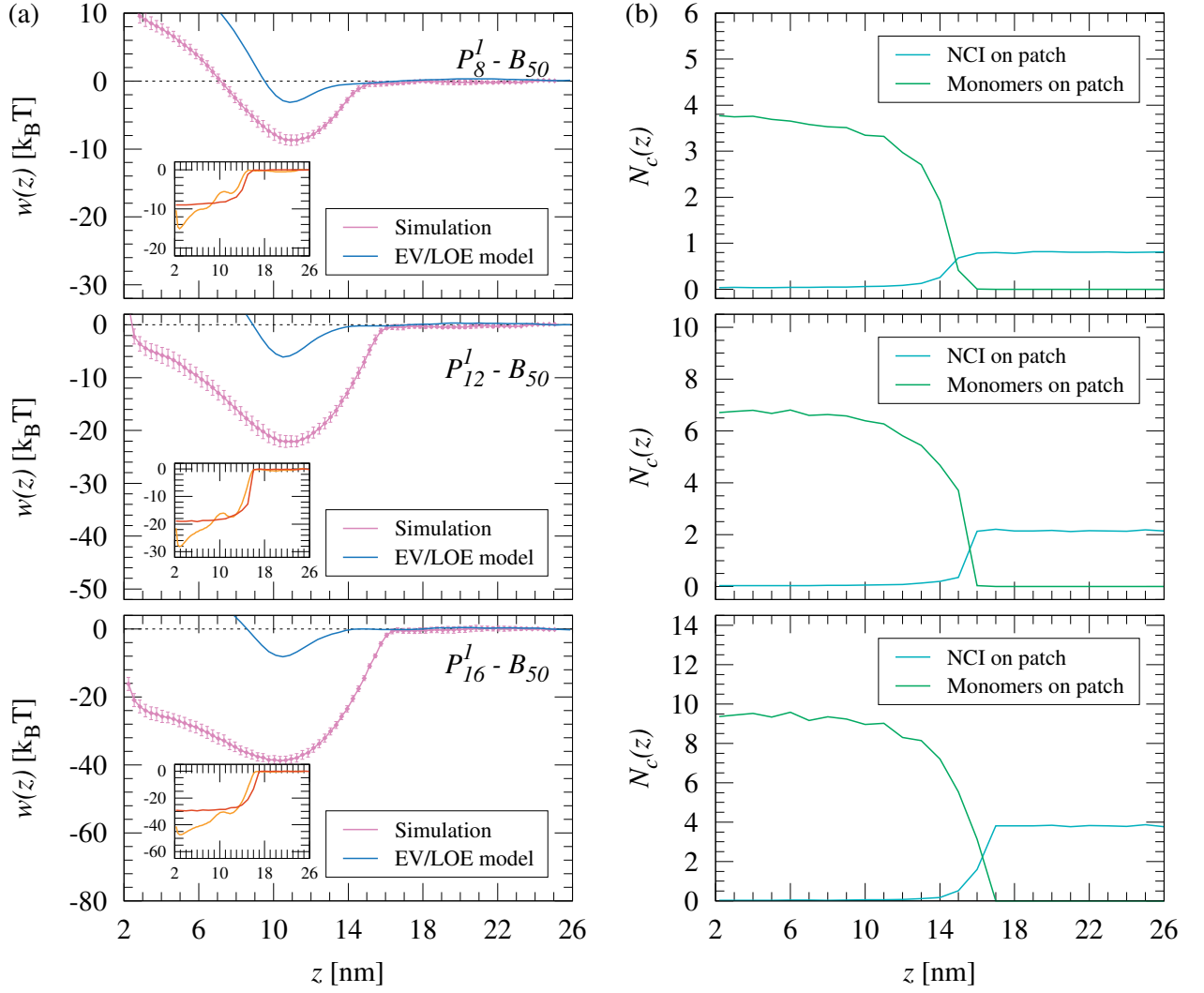


Figure 5.29: (a) Simulated PMFs $w(z)$ for $[P_s^I - B_{50}]$ with $s = 8, 12, 16$ at $c_s = 100$ mM. The insets show the difference between the simulated PMF and EV/LOE model (orange solid line) and the gain in translational entropy of the released ions (brown solid line). (b) Number of counted ions $N_c(z)$ on the patch (denoted by "NCI on patch" in the legend and by $N_-(z)$ in Eq. (5.9)) as well as the contacts of PE monomers with the patch (denoted by "Monomers on patch" in the legend while the number of released positively charged ions is given by $\{1 - \Gamma^{-1}\} N_+(z)$ as defined in Eq. (5.9)) as a function of z .

but is still attractive for the higher patch sizes. This is true for both salt concentrations and also indicates that the degree of charge heterogeneity on surfaces decisively determines whether attraction or repulsion occurs. As is stated in Eq. (5.8), the dipole of the protein couples to the electric field which is strongest in the PMF minimum (not shown) where the patch aligns nearly perpendicular to the grating surface as depicted for example in Figure 5.24 (b). The orange solid line in the insets of Figures 5.28 (a) and 5.29 (a) shows the difference between the simulated PMF and EV/LOE model and clearly reveals a strong attractive phenomenon. To rationalize the origin of this attraction we have determined the gain in translational entropy of the released ions via Eq. (5.9) which is represented by the brown solid line in the same inset. It is found that both curves agree well but only as long as the patchy protein does not completely enter into the PE brush. Deep in the brush, however, the complexity of the system is not easy to explain which is most likely caused by nonlinear ion release effects and asymmetric interactions. Note that the released ions are determined

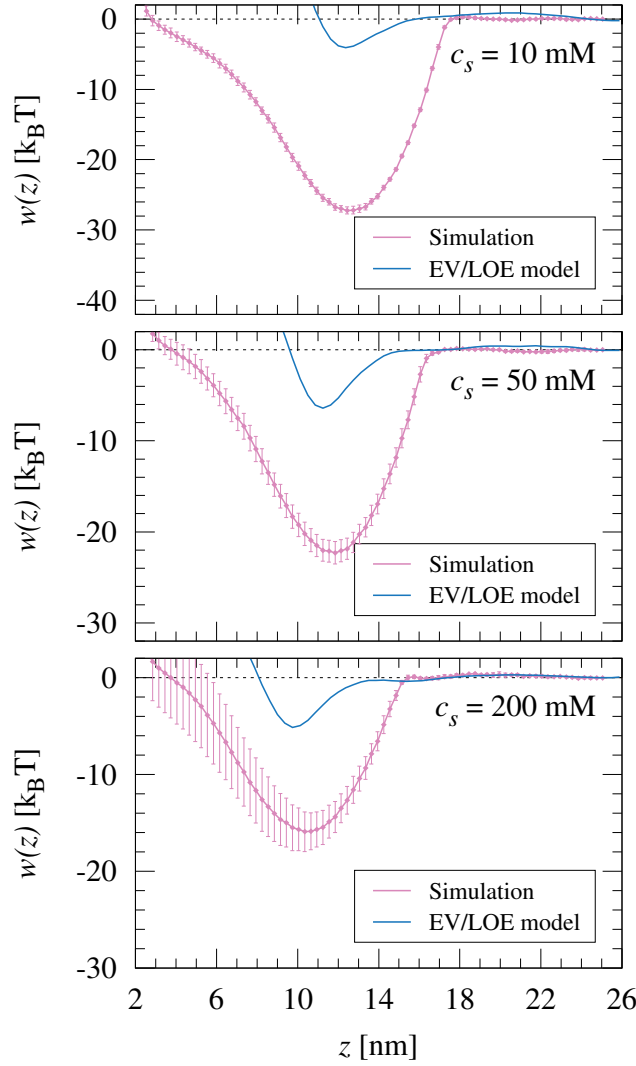


Figure 5.30: Salt concentration dependent PMF profiles $w(z)$ for the $[P_{12}^1 - B_{50}]$ system.

from the localization of the coions (NCI) and PE monomers on the positive patch which are presented in Figure 5.28 (b) and 5.29 (b) and discussed now. When the patchy protein stays in the bulk, the number of negatively charged ions on the patch remains constant which but increases with increasing patch size s or ionic strength c_s . Once the protein reaches the PE brush surface a release of coions occurs, while simultaneously first PE monomers interact with the positive patch and lead to a quick rise of the number of PE monomers. Upon further pulling, the coions are completely released and the number of PE monomers saturates to a constant value in the brush layer. This depends only on the patchiness and may lead up to roughly 10 PE monomers on the patch.

Influence of the salt concentration

For further investigating the effect of the ionic strength on the PMF, we first consider in Figure 5.30 the $[P_{12}^1 - B_{50}]$ system at $c_s = 10$ mM, 50 mM, and 200 mM. As expected, the interaction between the patchy protein and PE brush is weakened with increasing salt concentration. In the proximity of the grafting surface the PMFs are even repulsive which originates from excluded volume interactions because of the high local PE monomer con-

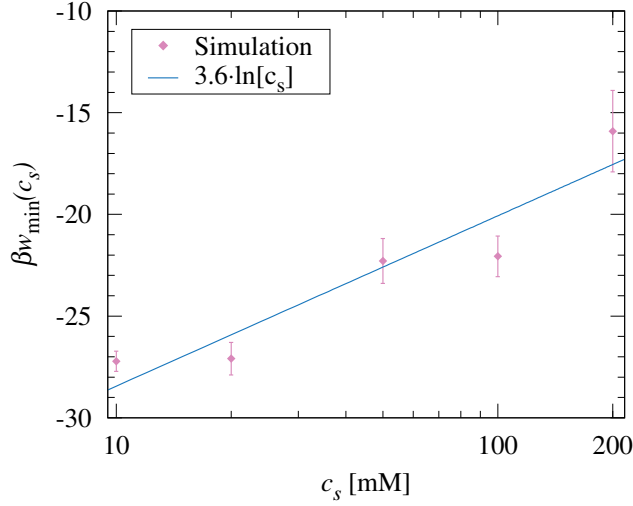


Figure 5.31: Binding affinity βw_{\min} (minimum value of the PMFs) as a function of the ionic strength c_s for the $[P_{12}^1 - B_{50}]$ system. The blue solid line is a fit according to the function $\beta w_{\min}(c_s) = \tilde{a} + \tilde{N} \ln[c_s]$ with $\tilde{a} = -36.8$ and $\tilde{N} = 3.6$.

centration. By comparing the simulated PMFs to the EV/LOE model, we see a distinct difference which becomes smaller with increasing salt concentration. As previously mentioned, in the EV/LOE model the monopole $U_{mc}(z)$ and dipole $U_{dc}(z)$ contribution are obtained from the density profiles and therefore salt concentration dependent. This explains why the position and depth of the EV/LOE-minimum are different for the considered salt concentrations. The brush thickness can be roughly specified from the position of the PMF minimum where it is about 12.5 nm at $c_s = 10$ mM and 10 nm at $c_s = 200$ mM. Hence, the PE chains are stiffer when decreasing the salinity of the system.

Next, we discuss the salt concentration dependence of the binding affinity βw_{\min} represented by the minimum values of the PMFs from the $[P_{12}^1 - B_{50}]$ systems. The data together with a logarithmic fit of the form $\beta w_{\min}(c_s) = \tilde{a} + \tilde{N} \ln[c_s]$ are depicted in Figure 5.31. As can be seen, the data points are somewhat scattered and do not perfectly lie on a straight line as it was, for example, for the protein-PE complexes in Section 5.3.2. This is probably due to the more complex arrangement of the PE chains near the brush surface where the interaction between single PE chains and the positively charged patch is asymmetric and irregular. However, from the best fit we get for $\tilde{a} = -36.8$ and for $\tilde{N} = 3.6$ which indicates ion release in the order of 3 to 4 when the globular protein adheres to the brush surface. Despite this number is small, our analysis unambiguously demonstrate the existence of the ion release mechanism leading to a substantial gain in translational entropy and, moreover, there are electrostatic forces responsible for the uptake of globular proteins into a like-charged PE brush. Remember that this matter is controversially discussed in the literature [35, 37, 38, 40, 198].

Interaction between a PE brush and two-patched proteins

The manner in which a globular protein with antipodally aligned patches ($m = 2$) interacts with a PE brush is presented in Figure 5.32. While for $s = 8$ the simulated PMFs within

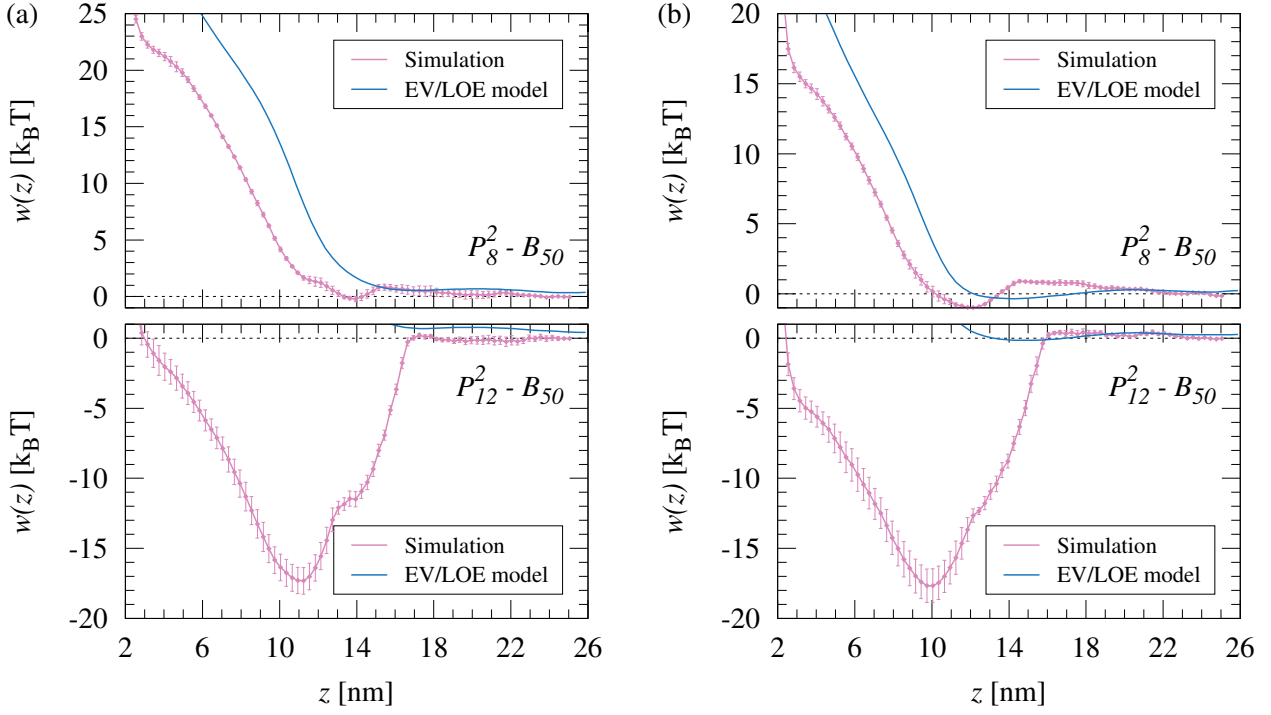


Figure 5.32: Interaction between a protein with antipodally aligned patches ($m = 2$) and a PE brush at ionic strengths of (a) 20 mM and (b) 100 mM.

the brush layer are overall repulsive for 20 mM and 100 mM salt concentrations, they are strongly attractive for $s = 12$ at both ionic strengths. The weakly pronounced global minima in the PMFs of $s = 8$ obviously indicate favorable electrostatic interactions of the PE chains with one of the two patches on the protein surface at the brush surface. Interestingly, at $c_s = 20$ mM there is a small plateau in the PE brush which is due to the penetration of the protein into the brush layer where the PE chains also interact with the second positive patch. However, at $c_s = 100$ mM this plateau is no longer discernible. A putative reason why there is no distinctive minimum in the brush layer might be the fact that the degree of the patchiness is less pronounced to compete electrostatically with the bare charges of the globular protein and PE monomers. In contrast, for $s = 12$ we recognize a metastable state reflected by the first local minimum in the PMF at $c_s = 20$ mM which corresponds to the first contact of PE monomers with one patch while, due to further approaching, a global minimum arises. Moreover, increasing the salinity to $c_s = 100$ mM the metastable state seems to vanish why only a distinct global minimum is recognizable. Not surprisingly, the EV/LOE model overestimates the PMFs since the values of the dipole moments for the two-patched proteins are the lowest ($\mu_P < 250$ D) which is why the dipole term $U_{dc}(z)$ does not contribute strongly to attractive interactions and is outweighed by excluded volume $U_{ev}(z)$ and monopole U_{mc} contributions. While for $s = 8$ the difference is roughly 10 $k_B T$ and 7 $k_B T$ for $c_s = 20$ mM and $c_s = 100$ mM, respectively, it fails completely for $s = 12$.

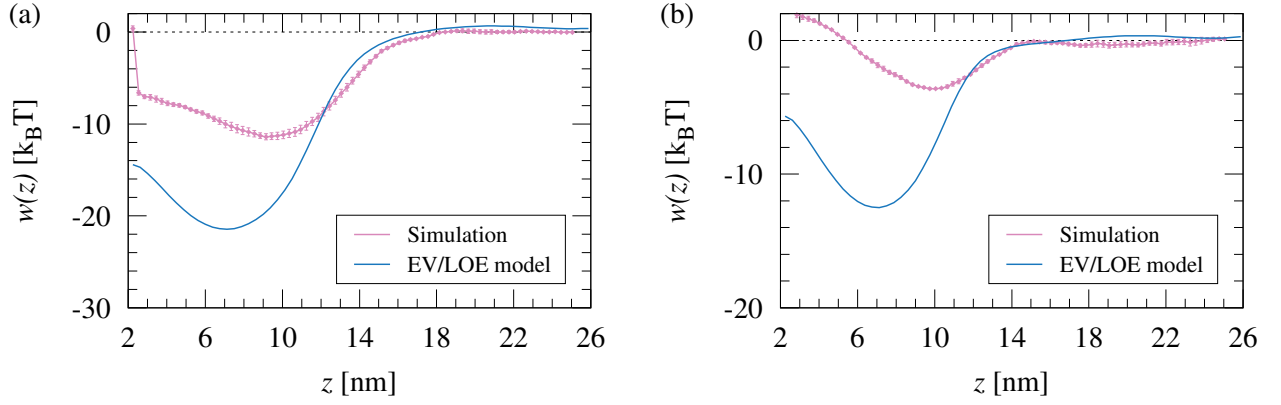


Figure 5.33: PMF profiles for a charge-inversed P_0^0 (+8 e) and B_{50} at (a) 20 mM and (b) 100 mM.

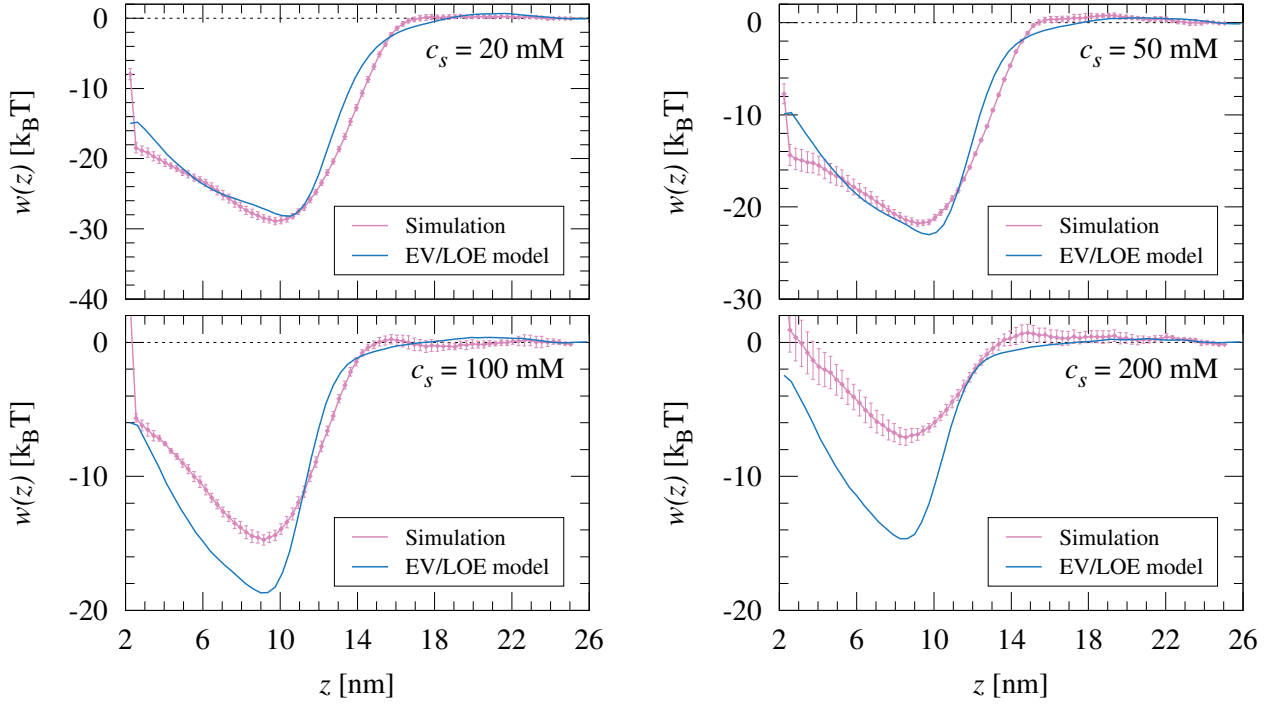


Figure 5.34: PMF profiles for a charge-inversed P_{12}^1 (+8 e) and B_{50} for different salt concentrations.

5.4.3 Uptake of charge-inversed proteins

Another important aspect to study is the inclusion of an oppositely charged protein (with and without patch) into the PE brush. Here, we provide results of interactions between a charge-inversed protein and a PE brush at various salt concentrations. With charge inversion, the inversion of all charges on the protein surface is meant. The proteins carry now a net charge of +8 e. The simulated PMFs of a charge-inversed P_0^0 interacting with a B_{50} at two ionic strengths, 20 mM and 100 mM, are presented in Figure 5.33 (a) and (b), respectively. In line with expectations, the interactions are attractive for both salt concentrations, while screening effects weaken the attraction up to 6 $k_B T$ at $c_s = 100$ mM. Also at the higher salt concentration the PMF is slightly repulsive in the vicinity of the grafting surface. Even though a comparison with the EV/LOE model indicates the correct trend, however, the difference between both is significant in the brush layer. More precisely, simulation and theory deviate by up to 10 $k_B T$ from each other. We assume that a substantial contribution

to this difference arises not only from ionic correlations but also from charge heterogeneity effects on the protein surface. A more interesting case is the interaction between a charge-inversed P_{12}^1 and B_{50} as shown in Figure 5.34 for different salt concentrations. Here, all PMFs are strongly attractive despite a negatively charged patch with $Z_s = -12$. It is obvious that the attraction in the PMFs originates from electrostatic interactions between the PE monomers and the positive discrete charges on the surface of the protein ($N_p > N_n$) since the interaction with the negatively charged patch yields only repulsive contributions in the brush layer. Also ionic effects should be envisaged here. When the simulated PMFs are compared to the EV/LOE model we find a discrepancy at ionic strengths of 100 mM and 200 mM which is about 5 $k_B T$ and 8 $k_B T$, while at 20 mM and 50 mM salt concentrations the agreement is very good. We believe that this correspondence is a fortunate coincidence of higher-order error cancellation.

5.5 Concluding remarks

In this chapter, we have introduced models for charged patchy proteins, PE, and PE brush to explore protein interactions with polymeric biomaterials. By means of implicit-solvent and explicit-ion Langevin dynamics computer simulations, the PMF of the adsorption process was computed depending on the degree of patchiness, ionic strength and PE chain length. The PMFs between pairs of like-charged proteins have revealed attractive interactions at short separations accompanied by only moderate ion release from the patches but substantial orientational alignments. Here, the simulated PMFs were compared to results from analytical models, which have shown a satisfactory agreement within their validity ranges. For like-charged protein-PE complexes and protein-PE brush associations we can safely conclude that in general the counterion release picture is indeed valid and clearly dominates the interactions in our considered systems. As a consequence, the large binding affinities are mostly governed by the gain in the translational entropy of released ions. Thus, the general conclusion of this chapter is that the adsorption process can be almost completely understood by an electrostatic approach and counterion release concept.

6 Summary and Outlook

In the present thesis the physical interactions of protein adsorption onto soft polymeric layers have been theoretically investigated by means of a cooperative binding model and Langevin dynamics computer simulations. The results have given valuable insights into the adsorption process and revealed the major driving force for the protein adsorption in our considered systems.

In order to characterize the driving force in the process of equilibrium protein adsorption onto charged core-shell microgels we have introduced a multi-component cooperative binding model. It separates out electrostatic cooperativity, accounts for protein interactions within the microgel and incorporates deswelling effects of the microgel particles. The model possesses full generality and describes the coupled effects of protein charge, radius and bulk concentration as well as the ionic strength and the intrinsic binding affinity of the protein to the core-shell microgel. Applying this approach to experimentally measured binding isotherms provides a more descriptive interpretation of the driving force in terms of separate physical interactions. Thus, we have shown that the adsorption isotherms of lysozyme, cytochrome c, papain and ribonuclease A to the charged core-shell microgel are mostly driven by electrostatic forces. Furthermore, we have also found that the microgel deswelling is mainly of electrostatic origin. Hence, the microgel becomes at least two times stiffer at high protein load pointing either to more specific effects (*e.g.* cross-links) or electrostatic correlations not accounted for in the mean-field PB cell model approach. The change and control of material properties upon protein load are essential for functionality [199] and suggest challenging investigations in the future. According to this, effects arising from protein aggregation, local pK_a -shifts, or nonlinear electrostatics should be considered in future theoretical studies when modeling protein adsorption onto soft polymeric layers.

The cooperative binding model can also be applied to predict mixtures with an arbitrary number of proteins adsorbing and/or desorbing onto the charged microgel. Once the relevant parameters (protein radius, charge and binding affinity) are determined from single-type protein adsorption, no further variable parameters are needed to predict the competitive protein adsorption. Thus, we successfully predicted the competitive adsorption for the binary protein mixtures lysozyme-cytochrome c, lysozyme-papain, and lysozyme-ribonuclease A onto the charged core-shell microgel. Within the context of a dynamical density functional theory, this binding model can also be used to access the spatial density variations of the proteins and their time-dependence [6], thus providing access to the kinetics of the adsorption process. Accordingly, experimental studies with theoretical comparison along these lines should be envisaged in the future.

For studying adsorption processes and interactions of proteins with polyelectrolyte materials we introduced well-defined models for globular proteins, PE and a PE brush. We used Langevin dynamics computer simulations with an implicit solvent model but explicit ions in

the GROMACS [188] simulation package.

For single globular proteins, we determined ion and electrostatic potential distributions. In particular, angle-resolved radial distribution functions uncovered a strongly heterogeneous accumulation of coions and depletion of counterions on the patch surface of the different globular proteins, while the angle-averaged potential has remained mostly unaltered for the different patchiness and salt concentration regimes considered here. Moreover, we computed the PMFs between various pairs of like-charged globular proteins. It was found that at short separations the PMFs between all globular proteins have attractive interactions accompanied by only moderate ion release from the patches but substantial orientational alignments. We managed to explain the long-ranged (monopole) part of the PMFs by a DLVO-type interaction, while for small dipole moments, no quadrupoles, and high salt concentrations an orientation-averaged pair potential (OAPP) based on DH theory extended to dipolar interactions [116] could also describe the PMFs satisfactorily. Hence, for known protein structures, OAPP may be a viable approach to quantify experimental pair interactions and virial coefficients [200–203]. However, low salt concentrations and large multipolar interactions remain a challenge for tractable theoretical descriptions.

Another computational study focused on the structures and interactions of a relatively short and highly charged PE chain complexing with like-charged patchy proteins as well as the uptake of oppositely and like-charged globular proteins by a PE brush. In both systems we observed strong electrostatic attractions in the PMFs that depend on the salinity, patch charge, and the degree of patchiness. In particular, for protein-PE complexes a novel two-state binding behavior for PEs with length comparable to the protein radius in case of two-patched proteins, where the PE ends are attached to the patches but the rest of the chain is repelled so that it resembles a 'tea-pot handle' like structure. Our systematic analysis further demonstrated a clear correlation between the binding affinity and the number of released ions, identifying them as a major driving factor for the strong association.

We can conclude that in general the counterion release picture is indeed valid and clearly dominates the interactions in our multipolar PE-patchy protein and protein-PE brush systems. As a consequence, the large binding affinities are mostly governed by the translational entropy of released ions. A quantitative analysis of the partial contributions of accumulated ions released from the protein patch and PE, however, appeared less simple due to ill-defined definitions of what are condensed and screening ions. Given the analysis of the individual free energy contributions from patch and PE/PE chains and the marked salt-dependence of the patch contribution, it was actually a bit surprising that the behavior of the 'Record-Lohman fit' is as linear as it appears. For the protein-PE complexes we could reconcile this apparent discrepancy by a combined counterion release/Debye-Hückel (CR/DH) model where we considered only the release effects at the PE, while the rest of the system was treated with a simplified charge-dipole DH model. The CR/DH described the binding affinity quantitatively, using only a single physically reasonable fit parameter, confirming that our model has captured the essential physics. For the protein-PE brush systems we also ap-

plied a model where we considered steric, van der Waals, electrostatic monopole and dipole contributions as well as the released ions from the PE monomers and from the protein patch. This approach satisfactorily described the total binding affinity in the case where the protein adheres on the brush surface, while nonlinear effects deep inside the brush layer complicate the analytical modeling greatly.

With the introduction of our globular proteins, new opportunities for the investigation and quantification of the role of charge patchiness in a wide variety for systems open up. For instance, possible uses of our globular proteins could be the investigation of electrostatic many-body effects, self-assembly of a few globular proteins, or protein interactions with heterogeneously charged surfaces or membranes. Moreover, the work of this thesis should be useful for the interpretation of experimental structures and binding affinities found for protein or nanoparticle complexation with a like-charged PE chain or the adsorption of proteins on PE coatings.

A The Newton-Raphson method

Nonlinear algebraic equations as defined in Eq. (4.26) cannot be solved generally in a closed form, but only numerically and through iteration. This means that from a first approximate solution a second approximate solution is calculated, which is more accurate than the first, which is used again as a base for the next even more accurate approximate solution. This iteration will be continued until the solution reaches the desired accuracy ϵ_{tol} . The most important method for solving systems of nonlinear equations in \mathbb{R}^N is the Newton-Raphson method [204].

In the following the Newton-Raphson method for solving Eq. (4.26) is described in detail. The reader should note that the mathematical variables in this appendix are defined independently to the previous chapters and used only in the context of the mathematical formulation.

For the sake of simplicity, two definitions are introduced:

$$\mathbf{F} \equiv \frac{N_P}{V_M} - \zeta_P c_P e^{-\beta(\Delta G_0 + \Delta G_{el} + \mu)} \quad \text{and} \quad \mathbf{x} \equiv N_P. \quad (\text{A.1})$$

A set of \mathcal{M} nonlinear equations with \mathcal{M} variables can be represented in the form

$$\mathbf{F}(\mathbf{x}) = \mathbf{0}, \quad (\text{A.2})$$

with suitable starting values \mathbf{x}^0 and the unknown solution \mathbf{x}^* . The derivation of the multi-dimensional Newton-Raphson method is then carried out via a multi-dimensional Taylor series expansions where \mathbf{F} is developed at \mathbf{x}^0 which yields [204]

$$0 = \mathbf{F}(\mathbf{x}^0 + \Delta \mathbf{x}) = \mathbf{F}(\mathbf{x}^0) + \mathbf{F}'(\mathbf{x}^0) \Delta \mathbf{x} + O(|\Delta \mathbf{x}|^2). \quad (\text{A.3})$$

Here, $\mathbf{F}'(\mathbf{x})$ denotes the Jacobian matrix of \mathbf{F} with

$$\mathbf{F}'(\mathbf{x})_{ij} = \frac{\partial F_i}{\partial x_j}, \quad (\text{A.4})$$

and $\Delta \mathbf{x} = \mathbf{x}^* - \mathbf{x}^0$. Neglecting higher order terms than one and introducing a so-called damping constant $\tilde{\lambda}_k$ leads to the iteration rule

$$\mathbf{x}^{k+1} = \Psi(\mathbf{x}^k) = \mathbf{x}^k - \tilde{\lambda}_k \frac{\mathbf{F}(\mathbf{x}^0)}{\mathbf{F}'(\mathbf{x}^0)} \quad (\text{A.5})$$

with

$$\max \Psi'(\mathbf{x}) = \max \frac{\mathbf{F}(\mathbf{x}) \mathbf{F}''(\mathbf{x})}{(\mathbf{F}'(\mathbf{x}))^2} = \Omega, \quad (\text{A.6})$$

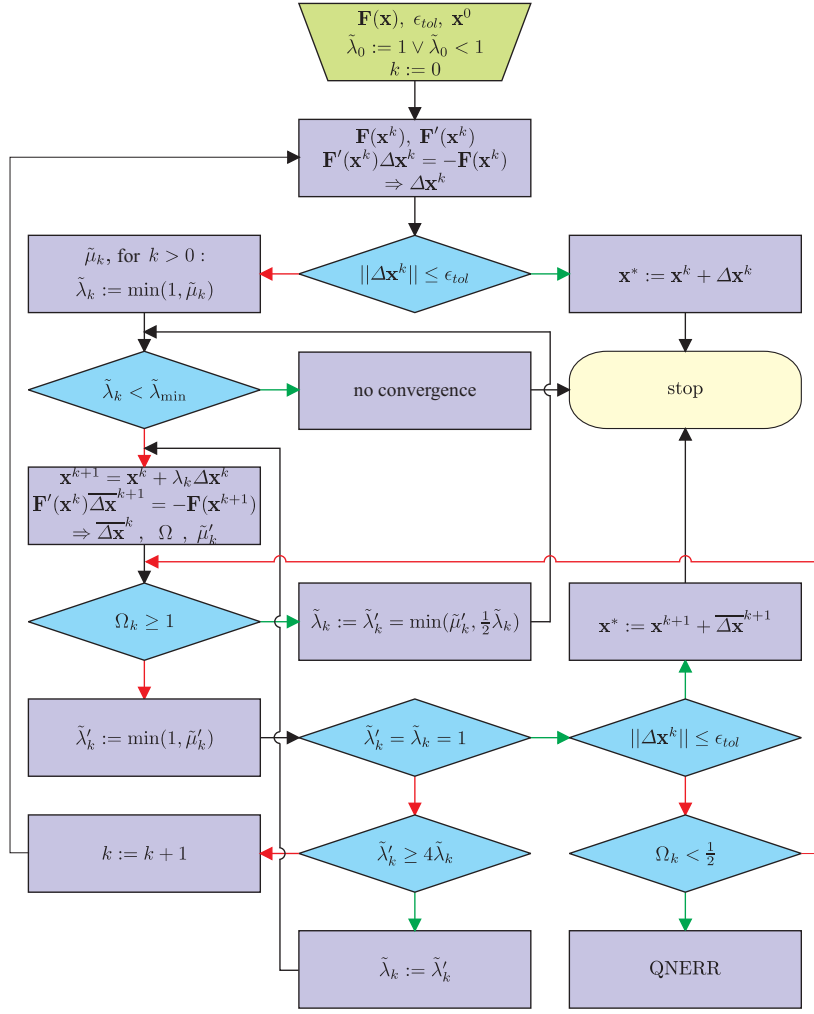


Figure A.1: A schematic diagram of the Newton-Raphson algorithm. QNERR denotes the Quasi-Newton method.

which then results in a linear convergence

$$|\mathbf{x}^{k+1} - \mathbf{x}^*| \leq \Omega |\mathbf{x}^k - \mathbf{x}^*|. \quad (\text{A.7})$$

The finding of starting values, which are in the region of convergence is referred to as trust region method and forms the basis for the code **nleq_err** [204]. This code is implemented in this thesis and adapted for our particular problem (see Chapter 4). Figure A.1 shows the schematic structure of the algorithm with the following used abbreviations:

$$\tilde{\mu}_k := \frac{||\Delta \mathbf{x}^{k+1}|| \cdot ||\overline{\Delta \mathbf{x}}^k||}{||\overline{\Delta \mathbf{x}}^k - \Delta \mathbf{x}^k|| \cdot ||\Delta \mathbf{x}^k||} \cdot \tilde{\lambda}_{k-1} \quad (\text{A.8})$$

$$\tilde{\mu}'_k := \frac{\frac{1}{2} ||\Delta \mathbf{x}^k|| \cdot \tilde{\lambda}_k^2}{||\overline{\Delta \mathbf{x}}^{k+1} - \{1 - \tilde{\lambda}_k\} \Delta \mathbf{x}^k||} \quad (\text{A.9})$$

$$\Omega_k := \frac{||\overline{\Delta \mathbf{x}}^{k+1}||}{||\Delta \mathbf{x}^k||}. \quad (\text{A.10})$$

B Quadrupole moments of charged patchy proteins

The quadrupole moment tensor Q of the introduced charged patchy protein models has been calculated according to [205]

$$Q_{ij} = \sum_l q_l \{3r_{il}r_{jl} - |\mathbf{r}_l|^2 \delta_{ij}\}, \quad (\text{B.1})$$

where Q_{ij} are the components of Q , while the indices i and j denote the Cartesian coordinates x, y , and z . The sum runs over all discrete charges q_l on the protein's surface at positions \mathbf{r}_l whereas δ_{ij} is the Kronecker delta. The quadrupole moments of all charged patchy proteins are provided in the following table.

Label	Q_{ij} in [e nm ²]
P_0^0	$\begin{pmatrix} 2.45 & -0.19 & -0.82 \\ -0.19 & -4.50 & 3.76 \\ -0.82 & 3.76 & 2.05 \end{pmatrix}$
P_8^1	$\begin{pmatrix} -11.20 & 51.27 & 7.47 \\ 51.27 & 39.88 & 8.58 \\ 7.47 & 8.58 & -28.68 \end{pmatrix}$
P_{12}^1	$\begin{pmatrix} -12.33 & 61.99 & 2.74 \\ 61.99 & 59.91 & 3.42 \\ 2.74 & 3.42 & -47.58 \end{pmatrix}$
P_{16}^1	$\begin{pmatrix} -9.56 & 83.37 & 1.16 \\ 83.37 & 74.13 & -0.88 \\ 1.16 & -0.88 & -64.57 \end{pmatrix}$
P_8^2	$\begin{pmatrix} -19.07 & 74.83 & 8.38 \\ 74.83 & 66.71 & -15.09 \\ 8.38 & -15.09 & -47.64 \end{pmatrix}$
P_{12}^2	$\begin{pmatrix} -22.31 & 121.87 & -0.74 \\ 121.87 & 104.50 & -13.99 \\ -0.74 & -13.99 & -82.19 \end{pmatrix}$

C List of abbreviations

BSA:	bovine serum albumin
Coul:	Coulomb
CPPM:	charged patchy protein models
CR:	counterion release
CSM:	core-shell microgel
DH:	Debye-Hückel
DLS:	dynamic light scattering
DLVO:	Derjaguin-Landau-Verwey-Overbeek
el:	electrostatic
EV:	excluded volume
FFT:	fast Fourier transforms
FITC:	fluorescein isothiocyanate
ITC:	isothermal titration calorimetry
LOE:	leading order electrostatics
LPB:	linearized Poisson-Boltzmann
MC:	Monte Carlo
MFA:	mean-field approximation
MP:	Mie potential
OAPP:	Orientation-averaged pair potential of mean force
PB:	Poisson-Boltzmann
PE:	polyelectrolyte
pI:	isoelectric point
PME:	Particle-Mesh-Ewald
PMF:	potential of mean force
pNiPAm:	Poly(N-isopropylacrylamide)
SLD:	steered Langevin dynamics
SMD:	steered molecular dynamics
US:	umbrella sampling
vdW:	van der Waals
\mathcal{P} :	probability distribution
\mathcal{Z} :	partition function
\mathcal{F} :	Helmholtz free energy
\mathcal{H} :	Hamiltonian
F :	force
F_{ext} :	external force
F_{vis} :	frictional force

$\dot{F}(t)$: random force
 \mathbf{p} : momentum of the particle
 \mathbf{r} : position in space
 Λ : thermal de Broglie wavelength
 N : number of particles
 V : volume
 T : temperature
 m : particle mass
 e : elementary charge
 ϵ_0 : dielectric constant
 ϵ_r : relative permittivity
 Z_i : ion charge valency
 k_B : Boltzmann constant
 R : radius
 v : velocity
 t : time
 ξ : friction constant
 q_i : particle charge
 n : exponent for repulsion
 k : exponent for attraction
 ϵ^* : potential well
 σ^* : van der Waals radius
 I : intensity
 τ : time delay
 $g^{(1)}$: first order autocorrelation function
 $g^{(2)}$: second order autocorrelation function
 q_w : magnitude of the scattering wave vector
 m_1 : refractive index
 λ_w : wavelength of laser source
 α : scattering angle
 D : diffusion coefficient
 η_{vis} : viscosity of the solution
 c_s : salt concentration
 c : coion and/or counterion concentration
 B_2 : second virial coefficient
 p : pressure
 p_{osm} : osmotic pressure
 p_{elas} : elastic pressure
 p_{ion} : osmotic pressure of ions
 ρ_f : fix charge distribution

$n(\mathbf{r})$: number density
 $\phi(\mathbf{r})$: total electrostatic potential
 Φ : rescaled electrostatic potential
 Φ_1 : electrostatic perturbation
 Φ_D : Donnan potential
 κ : inverse Debye screening length
 λ_B : Bjerrum length
 R_{cr} : microgel core radius
 R_M : microgel radius
 V_M : microgel volume
 N_M : number of charged network monomers
 Z_M : microgel charge valency
 c_M : microgel concentration
 N_m : number of charged monomers within the cell
 c_m : charged monomers concentration within the cell
 R_c : cell radius
 V_c : cell volume
 x : molar ratio
 c_a : concentration of the absorbent
 ν_0 : standard volume
 ζ : partition sum
 Q : heat
 Q' : incremental heat
 \mathcal{E}_{ads} : adsorption energy
 ΔH_{ITC} : heat of binding
 ΔS : entropy changes
 K : binding affinity
 ΔG_0 : intrinsic free energy
 ΔG_{el} : free energy of electrostatic transferring
 $\beta\mu$: chemical potential
 Θ : fraction of bound molecules
 N_S : number of binding sites
 N_P : number of bound/adsorbed proteins
 N_T : total number of molecules
 N_n : number of negative charges on protein surface
 N_p : number of positive charges on protein surface
 A_P : patch area
 R_P : protein radius
 σ_P : effective protein diameter
 Z_P : protein charge valency

μ_P : protein dipole moment
 c_P : protein concentration
 c_{patch} : concentration of accumulated ions on the positive protein patch
 η : protein packing fraction
 b_P : bond length of neighboring beads
 K_P : spring constant connecting neighboring beads
 R_{PE} : polyelectrolyte radius of gyration
 Z_{PE} : polyelectrolyte charge valency b_{mon} : bond length between two monomers
 K_{mon} : force constant between two monomers
 γ : angle between a triplet of monomers
 K_γ : force constant between a triplet of monomers
 Γ : Manning parameter
 b : distance between charged monomers
 f_{con} : fraction of condensed counterions
 N_{mon} : number of monomers
 \tilde{N} : number of released ions
 c_{PE} : concentration of condensed ions around the polyelectrolyte
 τ_B : grafting density
 L : side length of the simulation box
 v_p : pulling rate

Bibliography

- [1] J. Lippincott-Schwartz, E. Snapp, and A. Kenworthy, “Studying Protein Dynamics in Living Cells,” *Nat. Rev. Mol. Cell Bio.*, vol. 2, pp. 444–456, 2002.
- [2] J. Kleinschmidt, “Membrane Proteins – Introduction,” *Cell. Mol. Life Sci.*, vol. 60, no. 8, pp. 1527–1528, 2003.
- [3] J. Berg, J. Tymoczko, and L. Stryer, *Biochemistry, Fifth Edition*. W. H. Freeman, 2002.
- [4] R. Duncan, “The Dawning Era of Polymer Therapeutics,” *Nat. Rev. Drug Discov.*, vol. 2, no. 5, pp. 1474–1776, 2003.
- [5] P. Dutta, S. Tripathi, G. Mehrotra, and J. Dutta, “Perspectives for Chitosan Based Antimicrobial Films in Food Applications,” *Food Chem.*, vol. 114, no. 4, pp. 1173–1182, 2009.
- [6] Q. Wei, T. Becherer, S. Angioletti-Uberti, J. Dzubiella, C. Wischke, A. Neffe, A. Lendlein, M. Ballauff, and R. Haag, “Protein Interactions with Polymer Coatings and Biomaterials,” *Angew. Chem. Int. Edit.*, vol. 53, no. 31, pp. 8004–8031, 2014.
- [7] A. Hucknall, S. Rangarajan, and A. Chilkoti, “In Pursuit of Zero: Polymer Brushes that Resist the Adsorption of Proteins,” *Adv. Mater.*, vol. 21, no. 23, pp. 2441–2446, 2009.
- [8] M. Knetsch and L. Koole, “New Strategies in the Development of Antimicrobial Coatings: The Example of Increasing Usage of Silver and Silver Nanoparticles,” *Polymers*, vol. 3, no. 1, pp. 340–366, 2011.
- [9] K. Binder and A. Milchev, “Polymer Brushes on Flat and Curved Surfaces: How Computer Simulations can Help to Test Theories and to Interpret Experiments,” *J. Polym. Sci. Part B Polym. Phys.*, vol. 50, no. 22, pp. 1515–1555, 2012.
- [10] W. Blackburn, E. Dickerson, M. Smith, J. McDonald, and L. Lyon, “Peptide-Functionalized Nanogels for Targeted siRNA Delivery,” *Bioconjugate Chem.*, vol. 20, pp. 960–968, 2009.
- [11] S. Ghugare, P. Mozetic, and G. Paradossi, “Temperature-Sensitive Poly(vinyl alcohol)/Poly(methacrylate-co-N-isopropyl acrylamide) Microgels for Doxorubicin Delivery,” *Biomacromolecules*, vol. 10, pp. 1589–1596, 2009.
- [12] M. Smith and L. Lyon, “Multifunctional Nanogels for siRNA Delivery,” *Acc. Chem. Res.*, vol. 45, pp. 985–993, 2012.

- [13] A. Sassi, A. Shaw, S. Han, H. Blanch, and J. Prausnitz, "Partitioning of Proteins and Small Biomolecules in Temperature- and pH-Sensitive Hydrogels," *Polymer*, vol. 37, pp. 2151–2164, 1996.
- [14] G. Eichenbaum, P. Kiser, A. Dobrynin, S. Simon, and D. Needham, "Investigation of the Swelling Response and Loading of Ionic Microgels with Drugs and Proteins: The Dependence on Cross-Link Density," *Macromolecules*, vol. 32, no. 15, pp. 4867–4878, 1999.
- [15] G. Eichenbaum, P. Kiser, D. Shah, S. Simon, and D. Needham, "Investigation of the Swelling Response and Drug Loading of Ionic Microgels: The Dependence on Functional Group Composition," *Macromolecules*, vol. 32, pp. 8996–9006, 1999.
- [16] N. Peppas, P. Bures, W. Leobandung, and H. Ichikawa, "Hydrogels in Pharmaceutical Formulations," *Eur. J. Pharm. Biopharm.*, vol. 50, pp. 27–46, 2000.
- [17] C. Khoury, T. Adalsteinsson, B. Johnson, W. Crone, and D. Beebe, "Tunable Microfabricated Hydrogels – A Study in Protein Interaction and Diffusion," *Biomedical Devices*, vol. 5, pp. 35–45, 2003.
- [18] C. Alarcon, S. Pennadam, and C. Alexander, "Stimuli Responsive Polymers for Biomedical Applications," *Chem. Soc. Rev.*, vol. 34, pp. 276–285, 2005.
- [19] A. Bajpai, S. Shukla, S. Bhanu, and S. Kankane, "Responsive Polymers in Controlled Drug Delivery," *Prog. Polym. Sci.*, vol. 33, pp. 1088–1118, 2008.
- [20] A. Bridges, N. Singh, K. Burnsa, J. Babensee, L. Lyon, and A. Garcia, "Reduced Acute Inflammatory Responses to Microgel Conformal Coatings," *Biomaterials*, vol. 29, pp. 4605–4615, 2008.
- [21] N. Welsch, J. Dzubiella, A. Graebert, and M. Ballauff, "Protein Binding to Soft Polymeric Layers: A Quantitative Study by Fluorescence Spectroscopy," *Soft Matter*, vol. 8, pp. 12 043–12 052, 2012.
- [22] N. Welsch, A. Becker, J. Dzubiella, and M. Ballauff, "Core-Shell Microgels as Smart Carriers for Enzymes," *Soft Matter*, vol. 8, pp. 1428–1436, 2012.
- [23] T. Jung, W. Kamm, A. Breitenbach, G. Klebe, and T. Kissel, "Loading of Tetanus Toxoid to Biodegradable Nanoparticles from Branched Poly(sulfobutyl-polyvinyl alcohol)-g-(lactide-co-glycolide) Nanoparticles by Protein Adsorption: A Mechanistic Study," *Pharm. Research*, vol. 19, pp. 1105–1113, 2002.
- [24] V. Kabanov, V. Skobeleva, V. Rogacheva, and A. Zezin, "Sorption of Proteins by Slightly Cross-Linked Polyelectrolyte Hydrogels: Kinetics and Mechanism," *J. Phys. Chem. B*, vol. 108, pp. 1485–1490, 2004.

- [25] T. Cedervall, I. Lynch, S. Lindman, T. Berggard, E. Thulin, H. Nilsson, K. Dawson, and S. Linse, “Understanding the Nanoparticle–Protein Corona using Methods to Quantify Exchange Rates and Affinities of Proteins for Nanoparticles,” *Proc. Natl. Acad. Sci.*, vol. 104, pp. 2050–2055, 2007.
- [26] S. Lindman, I. Lynch, E. Thulin, H. Nilsson, K. Dawson, and S. Linse, “Systematic Investigation of the Thermodynamics of HSA Adsorption to N-iso-propylacrylamide/N-tert-butylacrylamide Copolymer Nanoparticles. Effects of Particle Size and Hydrophobicity,” *Nano Lett.*, vol. 7, pp. 914–920, 2007.
- [27] M. De, C. You, S. Srivastava, and V. Rotello, “Biomimetic Interactions of Proteins with Functionalized Nanoparticles: A Thermodynamic Study,” *J. Am. Chem. Soc.*, vol. 129, pp. 10 747–10 753, 2007.
- [28] C. Cai, U. Bakowsky, E. Rytting, A. Schaper, and T. Kissel, “Charged Nanoparticles as Protein Delivery Systems: A Feasibility Study using Lysozyme as Model Protein,” *Eur. J. Pharm. Biopharm.*, vol. 69, pp. 31–42, 2008.
- [29] C. Johansson, P. Hansson, and P. Malmsten, “Interaction between Lysozyme and Poly(acrylic acid) Microgels,” *J. Colloid Interf. Sci.*, vol. 316, pp. 350–359, 2007.
- [30] C. Johansson, J. Gernandt, M. Bradley, B. Vincent, and P. Hansson, “Interaction between Lysozyme and Colloidal Poly(nipam-co-acrylic acid) Microgels,” *J. Colloid Interf. Sci.*, vol. 347, pp. 241–251, 2010.
- [31] Y. Li, R. de Vries, M. Kleijn, T. Slaghek, J. Timmermans, M. Stuart, and W. Norde, “Lysozyme Uptake by Oxidized Starch Polymer Microgels,” *Biomacromolecules*, vol. 11, pp. 1754–1762, 2010.
- [32] G. Longo, M. de la Cruz, and I. Szleifer, “Molecular Theory of Weak Polyelectrolyte Thin Films,” *Soft Matter*, vol. 8, pp. 1344–1354, 2012.
- [33] P. Flory, *Principles of Polymer Chemistry*. Ithaca, NY: Cornell University Press, 1953.
- [34] A. Becker, N. Welsch, C. Schneider, and M. Ballauff, “Adsorption of RNase A on Cationic Polyelectrolyte Brushes: A Study by Isothermal Titration Calorimetry,” *Biomacromolecules*, vol. 12, no. 11, pp. 3936–3944, 2011.
- [35] A. Wittemann, B. Haupt, and M. Ballauff, “Adsorption of Proteins on Spherical Polyelectrolyte Brushes in Aqueous Solution,” *Phys. Chem. Chem. Phys.*, vol. 5, pp. 1671–1677, 2003.
- [36] W. de Vos, F. Leermakers, A. de Keizer, M. Stuart, and J. Kleijn, “Field Theoretical Analysis of Driving Forces for the Uptake of Proteins by Like-Charged Polyelectrolyte

- Brushes: Effects of Charge Regulation and Patchiness,” *Langmuir*, vol. 26, no. 1, pp. 249–259, 2010.
- [37] P. Biesheuvel and A. Wittemann, “A Modified Box Model Including Charge Regulation for Protein Adsorption in a Spherical Polyelectrolyte Brush,” *J. Phys. Chem. B*, vol. 109, no. 9, pp. 4209–4214, 2005.
 - [38] A. Wittemann and M. Ballauff, “Interaction of Proteins with Linear Polyelectrolytes and Spherical Polyelectrolyte Brushes in Aqueous Solution,” *Phys. Chem. Chem. Phys.*, vol. 8, pp. 5269–5275, 2006.
 - [39] P. Biesheuvel, F. Leermakers, and M. Stuart, “Self-Consistent Field Theory of Protein Adsorption in a non-Gaussian Polyelectrolyte Brush,” *Phys. Rev. E*, vol. 73, p. 011802, 2006.
 - [40] F. Leermakers, M. Ballauff, and O. Borisov, “On the Mechanism of Uptake of Globular Proteins by Polyelectrolyte Brushes: A Two-Gradient Self-Consistent Field Analysis,” *Langmuir*, vol. 23, no. 7, pp. 3937–3946, 2007.
 - [41] S. Tenzer, D. Docter, J. Kuharev, A. Musyanovych, V. Fetz, R. Hecht, F. Schlenk, D. Fischer, K. Kiouptsi, C. Reinhardt, K. Landfester, H. Schild, M. Maskos, S. Knauer, and R. Stauber, “Rapid Formation of Plasma Protein Corona Critically Affects Nanoparticle Pathophysiology,” *Nat. Nanotechnol.*, vol. 8, pp. 772–781, 2013.
 - [42] C. Walkey and W. Chan, “Understanding and Controlling the Interaction of Nanomaterials with Proteins in a Physiological Environment,” *Chem. Soc. Rev.*, vol. 41, pp. 2780–2799, 2012.
 - [43] L. Vroman and A. Adams, “Findings with the Recording Ellipsometer Suggesting rapid Exchange of Specific Plasma Proteins at Liquid/Solid Interfaces,” *Surf. Sci.*, vol. 16, no. 0, pp. 438–446, 1969.
 - [44] C. Bamford, S. Cooper, and T. Tsurutta, *The Vroman Effect*. Taylor & Francis, 1992.
 - [45] M. Li, “Pharmacokinetics of Polymeric Nanoparticles at Whole Body, Organ, Cell, and Molecule Levels.” in *Handbook of Research on Nanoscience, Nanotechnology, and Adv. Mater.*, M. Bououdina and J. P. Davim, Eds. IGI Global, 2014.
 - [46] J. Ortega-Vinuesa and R. Hidalgo-Álvarez, “Sequential Adsorption of F(ab’)2 and BSA on Negatively and Positively Charged Polystyrene Latexes,” *Biotechnol. Bioeng.*, vol. 47, no. 6, pp. 633–639, 1995.
 - [47] M. Holmberg and X. Hou, “Competitive Protein Adsorption of Albumin and Immunoglobulin G from Human Serum onto Polymer Surfaces,” *Langmuir*, vol. 26, no. 2, pp. 938–942, 2010.

- [48] B. Lassen and M. Malmsten, "Competitive Protein Adsorption at Plasma Polymer Surfaces," *J. Colloid Interf. Sci.*, vol. 186, no. 1, pp. 9–16, 1997.
- [49] M. Malmsten, D. Muller, and B. Lassen, "Sequential Adsorption of Human Serum Albumin (HSA), Immunoglobulin G (IgG), and Fibrinogen (Fgn) at HMDSO Plasma Polymer Surfaces," *J. Colloid Interf. Sci.*, vol. 193, no. 1, pp. 88–95, 1997.
- [50] Y. Huang, X. Lü, W. Qian, Z. Tang, and Y. Zhong, "Competitive Protein Adsorption on Biomaterial Surface Studied with Reflectometric Interference Spectroscopy," *Acta Biomater.*, vol. 6, no. 6, pp. 2083–2090, 2010.
- [51] D. Dell'Orco, M. Lundqvist, C. Oslakovic, T. Cedervall, and S. Linse, "Modeling the Time Evolution of the Nanoparticle–Protein Corona in a Body Fluid," *PLoS ONE*, vol. 5, p. e10949, 2010.
- [52] J. Park, B. Muhoberac, P. Dubin, and J. Xia, "Effects of Protein Charge Heterogeneity in Protein–Polyelectrolyte Complexation," *Macromolecules*, vol. 25, no. 1, pp. 290–295, 1992.
- [53] L. Ahmed, J. Xia, P. Dubin, and E. Kokufuta, "Stoichiometry and the Mechanism of Complex Formation in Protein–Polyelectrolyte Coacervation," *J. Macromol. Sci. A*, vol. 31, no. 1, pp. 17–29, 1994.
- [54] T. Hattori, R. Hallberg, and P. Dubin, "Roles of Electrostatic Interaction and Polymer Structure in the Binding of β -Lactoglobulin to Anionic Polyelectrolytes: Measurement of Binding Constants by Frontal Analysis Continuous Capillary Electrophoresis," *Langmuir*, vol. 16, no. 25, pp. 9738–9743, 2000.
- [55] E. Seyrek, P. Dubin, C. Tribet, and E. Gamble, "Ionic Strength Dependence of Protein–Polyelectrolyte Interactions," *Biomacromolecules*, vol. 4, no. 2, pp. 273–282, 2003.
- [56] K. Giger, R. Vanam, E. Seyrek, and P. Dubin, "Suppression of Insulin Aggregation by Heparin," *Biomacromolecules*, vol. 9, no. 9, pp. 2338–2344, 2008.
- [57] J. Mounsey, B. O'Kennedy, M. Fenelon, and A. Brodkorb, "The Effect of Heating on β -Lactoglobulin–Chitosan Mixtures as Influenced by pH and Ionic Strength," *Food Hydrocolloids*, vol. 22, no. 1, pp. 65–73, 2008.
- [58] I. Veselova, A. Kireiko, and T. Shekhovtsova, "Catalytic Activity and the Stability of Horseradish Peroxidase Increase as a Result of its Incorporation into a Polyelectrolyte Complex with Chitosan," *Appl. Biochem. Micro+*, vol. 45, no. 2, pp. 125–129, 2009.
- [59] W. Park and K. Na, "Dermatan Sulfate as a Stabilizer for Protein Stability in Poly(lactide-co-glycolide) Depot," *Biotechnol. Bioproc. E.*, vol. 14, no. 5, pp. 668–674, 2009.

- [60] C. Cooper, P. Dubin, A. Kayitmazer, and S. Turksen, "Polyelectrolyte-Protein Complexes," *Curr. Opin. Colloid Interface Sci.*, vol. 10, no. 1-2, pp. 52–78, 2005.
- [61] A. Kayitmazer, D. Seeman, B. Minsky, P. Dubin, and Y. Xu, "Protein-Polyelectrolyte Interactions," *Soft Matter*, vol. 9, pp. 2553–2583, 2013.
- [62] F. Wiegler, "Adsorption of a Macromolecule to a Charged Surface," *J. Phys. A*, vol. 10, no. 2, pp. 299–303, 1977.
- [63] T. Odijk, "Adsorption of a Polymer to a Randomly Interacting Surface," *Macromolecules*, vol. 23, no. 6, pp. 1875–1876, 1990.
- [64] F. von Goeler and M. Muthukumar, "Adsorption of Polyelectrolytes onto Curved Surfaces," *J. Chem. Phys.*, vol. 100, no. 10, pp. 7796–7803, 1994.
- [65] P. Haronska, T. Vilgis, R. Grottenmüller, and M. Schmidt, "Adsorption of Polymer Chains onto Charged Spheres: Experiment and Theory," *Macromol. Theory Simul.*, vol. 7, no. 2, pp. 241–247, 1998.
- [66] R. Netz and J. Joanny, "Complexation between a Semiflexible Polyelectrolyte and an Oppositely Charged Sphere," *Macromolecules*, vol. 32, no. 26, pp. 9026–9040, 1999.
- [67] S. Park, R. Bruinsma, and W. Gelbart, "Spontaneous Overcharging of Macro-Ion Complexes," *Europhys. Lett.*, vol. 46, no. 4, p. 454, 1999.
- [68] T. Nguyen and B. Shklovskii, "Overcharging of a Macroion by an Oppositely Charged Polyelectrolyte," *Physica A: Statistical Mechanics and its Applications*, vol. 293, no. 3-4, pp. 324–338, 2001.
- [69] H. Schiessel, R. Bruinsma, and W. Gelbart, "Electrostatic Complexation of Spheres and Chains under Elastic Stress," *J. Chem. Phys.*, vol. 115, no. 15, pp. 7245–7252, 2001.
- [70] T. Wallin and P. Linse, "Monte Carlo Simulations of Polyelectrolytes at Charged Micelles. 1. Effects of Chain Flexibility," *Langmuir*, vol. 12, no. 2, pp. 305–314, 1996.
- [71] C. Kong and M. Muthukumar, "Monte Carlo Study of Adsorption of a Polyelectrolyte onto Charged Surfaces," *J. Chem. Phys.*, vol. 109, no. 4, pp. 1522–1527, 1998.
- [72] T. Wallin and P. Linse, "Monte Carlo Simulations of Polyelectrolytes at Charged Hard Spheres with Different Numbers of Polyelectrolyte Chains," *J. Chem. Phys.*, vol. 109, no. 12, pp. 5089–5100, 1998.
- [73] F. Carlsson, P. Linse, and M. Malmsten, "Monte Carlo Simulations of Polyelectrolyte-Protein Complexation," *J. Phys. Chem. B*, vol. 105, no. 38, pp. 9040–9049, 2001.

- [74] P. Chodanowski and S. Stoll, “Polyelectrolyte Adsorption on Charged Particles: Ionic Concentration and Particle Size Effects – A Monte Carlo Approach,” *J. Chem. Phys.*, vol. 115, no. 10, pp. 4951–4960, 2001.
- [75] M. Jonsson and P. Linse, “Polyelectrolyte–Macroion Complexation. I. Effect of Linear Charge Density, Chain Length, and Macroion Charge,” *J. Chem. Phys.*, vol. 115, no. 7, pp. 3406–3418, 2001.
- [76] R. Messina, C. Holm, and K. Kremer, “Like-Charge Colloid–Polyelectrolyte Complexation,” *J. Chem. Phys.*, vol. 117, no. 6, pp. 2947–2960, 2002.
- [77] J. Dzubiella, A. Moreira, and P. Pincus, “Polyelectrolyte–Colloid Complexes: Polarizability and Effective Interaction,” *Macromolecules*, vol. 36, no. 5, pp. 1741–1752, 2003.
- [78] R. Messina, C. Holm, and K. Kremer, “Polyelectrolyte Multilayering on a Charged Sphere,” *Langmuir*, vol. 19, no. 10, pp. 4473–4482, 2003.
- [79] R. de Vries, “Monte Carlo Simulations of Flexible Polyanions Complexing with Whey Proteins at their Isoelectric Point,” *J. Chem. Phys.*, vol. 120, no. 7, pp. 3475–3481, 2004.
- [80] F. da Silva, M. Lund, B. Jönsson, and T. Åkesson, “On the Complexation of Proteins and Polyelectrolytes,” *J. Phys. Chem. B*, vol. 110, no. 9, pp. 4459–4464, 2006.
- [81] F. da Silva and B. Jönsson, “Polyelectrolyte–Protein Complexation Driven by Charge Regulation,” *Soft Matter*, vol. 5, pp. 2862–2868, 2009.
- [82] S. de Carvalho, R. Metzler, and A. Cherstvy, “Critical Adsorption of Polyelectrolytes onto Charged Janus Nanospheres,” *Phys. Chem. Chem. Phys.*, vol. 16, pp. 15 539–15 550, 2014.
- [83] G. Luque-Caballero, A. Martín-Molina, and M. Quesada-Pérez, “Polyelectrolyte Adsorption onto Like-Charged Surfaces Mediated by Trivalent Counterions: A Monte Carlo Simulation Study,” *J. Chem. Phys.*, vol. 140, no. 17, 2014.
- [84] E. Bianchi, R. Blaak, and C. Likos, “Patchy Colloids: State of the Art and Perspectives,” *Phys. Chem. Chem. Phys.*, vol. 13, pp. 6397–6410, 2011.
- [85] B. Isralewitz, J. Baudry, J. Gullingsrud, D. Kosztin, and K. Schulten, “Steered Molecular Dynamics Investigations of Protein Function,” *J. Mol. Graphics Modell.*, vol. 19, no. 1, pp. 13–25, 2001.
- [86] G. Torrie and J. Valleau, “Nonphysical Sampling Distributions in Monte Carlo Free-Energy Estimation: Umbrella Sampling,” *J. Comput. Phys.*, vol. 23, no. 2, pp. 187–199, 1977.

- [87] S. Park, F. Khalili-Araghi, E. Tajkhorshid, and K. Schulten, “Free Energy Calculation from Steered Molecular Dynamics Simulations using Jarzynski’s Equality,” *J. Chem. Phys.*, vol. 119, no. 6, pp. 3559–3566, 2003.
- [88] J. Lipfert, S. Doniach, R. Das, and D. Herschlag, “Understanding Nucleic Acid–Ion Interactions,” *Annu. Rev. Biochem.*, vol. 83, no. 1, pp. 813–841, 2014.
- [89] M. Deserno and C. Holm, “Cell model and poisson-boltzmann theory: A brief introduction,” in *Electrostatic Effects in Soft Matter and Biophysics*, ser. NATO Science Series, C. Holm, P. Kékicheff, and R. Podgornik, Eds., 2001, vol. 46, pp. 27–52.
- [90] D. McQuarrie, *Statistical Mechanics*. Sausalito, California: University Science Books, 2000.
- [91] J. Jeferson, L. Yan, and F. Jürgen, “The Mean-Field Theory for Attraction between Like-Charged Macromolecules,” *Physica A*, vol. 283, no. 1–2, pp. 1–5, 2000.
- [92] P. Chaikin and T. Lubensky, *Principles of Condensed Matter Physics*. Cambridge University Press, 2000.
- [93] H. Butt, K. Graf, and M. Kappl, *Physics and Chemistry of Interfaces*. Wiley-VCH, 2006.
- [94] P. Rieger, *Electrochemistry*. Springer Netherlands, 1994.
- [95] T. Wang, Y. Sheng, and H. Tsao, “Effects of Multivalent Salt Addition on Effective Charge of Dilute Colloidal Solutions,” *J. Chem. Phys.*, vol. 125, no. 19, 2006.
- [96] A. Grosberg, T. Nguyen, and B. Shklovskii, “Colloquium: The Physics of Charge inversion in Chemical and Biological Systems,” *Rev. Mod. Phys.*, vol. 74, pp. 329–345, 2002.
- [97] L. Belloni, “Ionic Condensation and Charge Renormalization in Colloidal Suspensions,” *Colloid Surface A*, vol. 140, no. 1–3, pp. 227–243, 1998.
- [98] G. Hartley, “The Application of the Debye–Hückel Theory to Colloidal Electrolytes,” *Trans. Faraday Soc.*, vol. 31, pp. 31–50, 1935.
- [99] A. Dobrynin and M. Rubinstein, “Theory of Polyelectrolytes in Solutions and at Surfaces,” *Prog. Polym. Sci.*, vol. 30, pp. 1049–1118, 2005.
- [100] R. Fuoss, A. Katchalsky, and S. Lifson, “The Potential of an Infinite Rod-Like Molecule and the Distribution of Counterions,” *Proc. Natl. Acad. Sci.*, vol. 37, pp. 579–586, 1951.
- [101] G. Manning, “Limiting Laws and Counterion Condensation in Polyelectrolyte Solutions I. Colligative Properties,” *J. Chem. Phys.*, vol. 51, no. 3, pp. 924–933, 1969.

- [102] F. Oosawa, *Polyelectrolytes*. New York: Marcel Dekker, 1971.
- [103] M. Record, T. Lohman, and P. de Haseth, “Ion Effects on Ligand–Nucleic Acid Interactions,” *J. Mol. Biol.*, vol. 107, pp. 145–158, 1976.
- [104] M. Deserno, C. Holm, and S. May, “Fraction of Condensed Counterions around a Charged Rod: Comparison of Poisson-Boltzmann Theory and Computer Simulations,” *Macromolecules*, vol. 33, pp. 199–206, 2000.
- [105] K. Henzler, B. Haupt, K. Lauterbach, A. Wittemann, O. Borisov, and M. Ballauff, “Adsorption of beta-Lactoglobulin on Spherical Polyelectrolyte Brushes: Direct Proof of Counterion Release by Isothermal Titration Calorimetry,” *J. Am. Chem. Soc.*, vol. 132, no. 9, pp. 3159–3163, 2010.
- [106] R. Buckingham, “The Classical Equation of State of Gaseous Helium, Neon and Argon,” *Proc. R. Soc. Lond. A*, vol. 168, pp. 264–283, 1938.
- [107] G. Mie, “Zur kinetischen Gastheorie der einatomigen Körper,” *Ann. Phys.*, vol. 11, pp. 657–697, 1903.
- [108] V. Papaioannou, T. Lafitte, C. Avendaño, C. Adjiman, G. Jackson, E. Müller, and A. Galindo, “Group Contribution Methodology Based on the Statistical Associating Fluid Theory for Heteronuclear Molecules Formed from Mie Segments,” *J. Chem. Phys.*, vol. 140, no. 5, 2014.
- [109] J. Dickerson and A. Boccaccini, *Electrophoretic Deposition of Nanomaterials*. Springer, 2011.
- [110] V. Schettino and S. Califano, “Lattice Dynamics and Interaction Potentials in Molecular Crystals,” *J. Mol. Struct.*, vol. 100, no. 0, pp. 459–483, 1983.
- [111] W. Wood and F. Parker, “Monte Carlo Equation of State of Molecules Interacting with the Lennard – Jones Potential. I. A Supercritical Isotherm at about Twice the Critical Temperature,” *J. Chem. Phys.*, vol. 27, no. 3, pp. 720–733, 1957.
- [112] B. Derjaguin and L. Landau, *Acta Physicochim. URSS*, vol. 14, p. 633, 1941.
- [113] “B. Derjaguin and L. Landau,” *Sov. Phys. JETP*, vol. 15, p. 633, 1945.
- [114] E. Verwey and J. Overbeek, *Theory of the Stability of Lyophobic Colloids*. Elsevier, Amsterdam, 1948.
- [115] G. Phillies, “Excess Chemical Potential of Dilute Solutions of Spherical Polyelectrolytes,” *J. Chem. Phys.*, vol. 60, p. 2721, 1974.

- [116] D. Bratko, A. Striolo, J. Wu, H. Blanch, and J. Prausnitz, "Orientation-Averaged Pair Potentials between Dipolar Proteins or Colloids," *J. Phys. Chem. B*, vol. 106, no. 10, pp. 2714–2720, 2002.
- [117] J. Dhont, *An Introduction to Dynamics of Colloids*. Elsevier Science, 1996.
- [118] D. Lemons and A. Gythiel, "Paul Langevin's 1908 Paper "On the Theory of Brownian Motion" ["Sur la Théorie du Mouvement Brownien," c. r. acad. sci. (paris) 146, 530–533 (1908)]," *Am. J. Phys.*, vol. 65, no. 11, pp. 1079–1081, 1997.
- [119] D. Frenkel and B. Smit, *Understanding Molecular Simulation: From Algorithms to Applications*. Academic Press, 2002.
- [120] R. Masel, *Principles of Adsorption and Reaction on Solid Surfaces*. New York: Wiley Interscience, 1996.
- [121] D. Ruthven, *Principles of Adsorption and Adsorption Processes*. Wiley, 1984.
- [122] M. Volmer and P. Mahnert, "Solution of Solid Substances in Liquid Surfaces and the Characteristics of Layers," *Z. Physik. Chem.*, vol. 115, pp. 239–252, 1925.
- [123] P. Hiemenz and R. Rajagopalan, *Principles of Colloid and Surface Chemistry, Third Edition, Revised and Expanded*. Taylor & Francis, 1997.
- [124] H. Zhou and M. Gilson, "Theory of Free Energy and Entropy in Noncovalent Binding," *Chem. Rev.*, vol. 109, pp. 4092–4107, 2009.
- [125] M. Pierce, C. Raman, and B. Nall, "Isothermal Titration Calorimetry of Protein–Protein Interactions," *Methods*, vol. 19, no. 2, pp. 213–221, 1999.
- [126] E. Freire, O. Mayorga, and M. Straume, "Isothermal Titration Calorimetry," *Anal. Chem.*, vol. 62, no. 18, pp. 950A–959A, 1990.
- [127] B. Berne and R. Pecora, *Dynamic Light Scattering: With Applications to Chemistry, Biology, and Physics*. Dover Publications, 2000.
- [128] P. Heitjans and J. Kärger, *Diffusion in Condensed Matter: Methods, Materials, Models*. Springer, 2006.
- [129] L. Onsager, "Reciprocal Relations in Irreversible Processes. II." *Phys. Rev.*, vol. 38, pp. 2265–2279, 1931.
- [130] M. Kuno, *Introductory Nanoscience*. Garland Science, 2011.
- [131] R. Kimmich, *Principles of Soft Matter Dynamics: Basic Theories, Non-Invasive Methods, Mesoscopic Aspects*. Springer, 2012.

- [132] J. Hansen and I. McDonald, *Theory of Simple Liquids: With Applications to Soft Matter*. Elsevier Science, 2013.
- [133] G. Guilbault, *Practical Fluorescence, Second Edition*. Taylor & Francis, 1990.
- [134] J. Robinson, E. Frame, and G. Frame, *Undergraduate Instrumental Analysis, Seventh Edition*. CRC Press, 2015.
- [135] S. Seelenmeyer, I. Deike, S. Rosenfeldt, C. Norhausen, N. Dingenouts, M. Ballauff, T. Narayanan, and P. Lindner, “Small-Angle X-Ray and Neutron Scattering Studies of the Volume Phase Transition in Thermosensitive Core-Shell Colloids,” *J. Chem. Phys.*, vol. 114, pp. 10 471–10 478, 2001.
- [136] D. Devore and G. Manning, “Application of Polyelectrolyte Limiting Laws to Virial and Asymptotic Expansions for Donnan Equilibrium,” *Biophys. Chem.*, vol. 2, pp. 42–48, 1974.
- [137] M. Buschmann and A. Grodzinsky, “A Molecular-Model of Proteoglycan-Associated Electrostatic Forces in Cartilage Mechanics,” *J. Biomechanical Eng.*, vol. 117, pp. 179–192, 1995.
- [138] K. Zeldovich and A. Khokhlov, “Osmotically Active and Passive Counterions in Inhomogeneous Polymer Gels,” *Macromolecules*, vol. 32, pp. 3488–3494, 1999.
- [139] P. Retailleau, M. Riés-Kautt, and A. Ducruix, “No Salting-In of Lysozyme Chloride Observed at low Ionic Strength over a Large Range of pH,” *Biophys. J.*, vol. 73, pp. 2156–2163, 1997.
- [140] R. Marcus, “Calculation of Thermodynamic Properties of Polyelectrolytes,” *J. Chem. Phys.*, vol. 23, pp. 1057–1068, 1955.
- [141] G. Gunnarsson, B. Jönsson, and H. Wennerström, “Surfactant Association into Micelles - An Electrostatic Approach,” *J. Phys. Chem. B*, vol. 84, pp. 3114–3121, 1980.
- [142] S. Alexander, P. Chaikin, P. Grant, G. Morales, and P. Pincus, “Charge Renormalization, Osmotic-Pressure, and Bulk Modulus of Colloidal Crystals – Theory,” *J. Chem. Phys.*, vol. 80, pp. 5776–5781, 1984.
- [143] B. Jönsson and H. Wennerström, “Phase Equilibria in a Three-Component Water-Soap-Alcohol System. A Thermodynamic Model,” *J. Phys. Chem. B*, vol. 91, pp. 338–352, 1987.
- [144] M. Tamashiro, Y. Levin, and M. Barbosa, “Donnan Equilibrium and the Osmotic Pressure of Charged Colloidal Lattices,” *Eur. Phys. J. B*, vol. 1, pp. 337–343, 1998.

- [145] M. Deserno and H. von Grünberg, “Osmotic Pressure of Charged Colloidal Suspensions: A Unified Approach to Linearized Poisson-Boltzmann Theory,” *Phys. Rev. E*, vol. 66, p. 011401, 2002.
- [146] R. Allen and P. Warren, “Complexation and Phase Behavior of Oppositely Charged Polyelectrolyte/Macroion Systems,” *Langmuir*, vol. 20, pp. 1997–2009, 2004.
- [147] P. Hansson, “Phase Behavior of Aqueous Polyion–Surfactant Ion Complex Salts: A Theoretical Analysis,” *J. Colloid Interf. Sci.*, vol. 332, pp. 183–193, 2009.
- [148] A. Denton, “Poisson-Boltzmann Theory of Charged Colloids: Limits of the Cell Model for Salty Suspensions,” *J. Phys. Condens. Matter*, vol. 22, no. 36, p. 364108, 2010.
- [149] J. Overbeek, “The Donnan Equilibrium,” *Prog. Biophys. Biophys. Chem.*, vol. 6, pp. 58–84, 1956.
- [150] F. Horkay and M. Zrinyi, “Studies on Mechanical and Swelling Behavior of Polymer Networks on the Basis of the Scaling Concept. 4. Extension of the Scaling Approach to Gels Swollen to Equilibrium in a Diluent of Arbitrary Activity,” *Macromolecules*, vol. 15, pp. 1306–1310, 1982.
- [151] M. Rubinstein, R. Colby, A. Dobrynin, and J. Joanny, “Elastic Modulus and Equilibrium Swelling of Polyelectrolyte Gels,” *Macromolecules*, vol. 29, pp. 398–406, 1996.
- [152] S. Dubrovskii, G. Rakova, M. Lagutina, and K. Kazanskii, “Osmotic Properties of Poly(ethylene oxide) Gels with Localized Charged Units,” *Polymer*, vol. 42, pp. 8075–8083, 2001.
- [153] P. de Gennes, *Scaling Concepts in Polymer Physics*. Cornell University Press.
- [154] Z. Hu, C. Li, and Y. Li, “The Scaling Exponents of Polyacrylamide and Acrylamide-sodium Acrylate Copolymer Gels,” *J. Chem. Phys.*, vol. 99, pp. 7108–7114, 1993.
- [155] R. Skouri, F. Schosseler, J. Munch, and S. Candau, “Swelling and Elastic Properties of Polyelectrolyte Gels,” *Macromolecules*, vol. 28, pp. 197–210, 1995.
- [156] G. Nisato, R. Skouri, F. Schosseler, J. Munch, and S. Candau, “Elastic Behaviour of Salt-Free Polyelectrolyte Gels,” *Faraday. Discuss.*, vol. 101, pp. 133–146, 1995.
- [157] S. Dubrovskii and G. Rakova, “Elastic and Osmotic Behavior and Network Imperfections of Nonionic and Weakly Ionized Acrylamide-Based Hydrogels,” *Macromolecules*, vol. 30, pp. 7478–7486, 1997.
- [158] W. de Vos, P. Biesheuvel, A. de Keizer, J. Kleijn, and M. Stuart, “Adsorption of the Protein Bovine Serum Albumin in a Planar Poly(acrylic acid) Brush Layer as Measured by Optical Reflectometry,” *Langmuir*, vol. 24, pp. 6575–6584, 2008.

- [159] R. Borrega, C. Tribet, and R. Audebert, “Reversible Gelation in Hydrophobic Polyelectrolyte/Protein Mixtures: An Example of Cross-Links between Soft and Hard Colloids,” *Macromolecules*, vol. 32, pp. 7798–7806, 1999.
- [160] T. Wiseman, S. Williston, J. Brandts, and L. Lin, “Rapid Measurement of Binding Constants and Heats of Binding using a New Titration Calorimeter,” *Anal. Biochem.*, vol. 179, pp. 131–137, 1989.
- [161] Y. Li, M. Kleijn, T. Slaghek, J. Timmermans, M. Stuart, and W. Norde, “Mobility of Lysozyme Inside Oxidized Starch Polymer Microgels,” *Soft Matter*, vol. 7, pp. 1926–1935, 2011.
- [162] R. Aveyard and R. Haydon, *Introduction to the Principles of Surface Chemistry*. Cambridge University Press, 1973.
- [163] S. McLaughlin, “The Electrostatic Properties of Membranes,” *Annu. Rev. Biophys. Biophys. Chem.*, vol. 18, pp. 113–136, 1989.
- [164] J. Seelig, “Thermodynamics of Lipid–Peptide Interactions,” *BBA Biomembranes*, vol. 1666, pp. 40–50, 2004.
- [165] K. Henzler, S. Rosenfeldt, A. Wittemann, L. Harnau, S. Finet, T. Narayanan, and M. Ballauff, “Directed Motion of Proteins Along Tethered Polyelectrolytes,” *Phys. Rev. Lett.*, vol. 100, p. 158301, 2008.
- [166] A. Santos, S. Yuste, and M. De Haro, “Equation of State of a Multicomponent d-Dimensional Hard-Sphere Fluid,” *Mol. Phys.*, vol. 96, no. 1, pp. 1–5, 1999.
- [167] S. Finet, F. Skouri-Panet, M. Casselyn, F. Bonneté, and A. Tardieu, “The Hofmeister Effect as seen by SAXS in Protein Solutions,” *Curr. Opin. Colloid Interface Sci.*, vol. 9, no. 1-2, pp. 112–116, 2004.
- [168] D. Cheng and Q. Xu, “Separation Distance Dependent Fluorescence Enhancement of Fluorescein Isothiocyanate by Silver Nanoparticles,” *Chem. Commun.*, pp. 248–250, 2007.
- [169] Y. Li, Z. Hu, and C. Li, “New Method for Measuring Poisson’s Ratio in Polymer Gels,” *J. Appl. Pol. Sci.*, vol. 50, pp. 1107–1111, 1993.
- [170] J. Yoon, S. Cai, Z. Suo, and R. Hayward, “Poroelastic Swelling Kinetics of Thin Hydrogel Layers: Comparison of Theory and Experiment,” *Soft Matter*, vol. 6, pp. 6004–6012, 2012.
- [171] A. Burmistrova, M. Richter, C. Uzun, and R. von Klitzing, “Effect of Cross-Linker Density of P(NIPAM-co-AAc) Microgels at Solid Surfaces on the Swelling/Shrinking Behaviour and the Young’s Modulus,” *Coll. Pol. Sci.*, vol. 289, pp. 613–624, 2011.

- [172] S. Gordon, J. Todd, and Z. Cohn, "In Vitro Synthesis and Secretion of Lysozyme by Mononuclear Phagocytes," *J. Exp. Med.*, vol. 139, no. 5, pp. 1228–1248, 1974.
- [173] S. Venkataramani, J. Truntzer, and D. Coleman, "Thermal Stability of High Concentration Lysozyme Across Varying pH: A Fourier Transform Infrared Study," *J. Pharm. Bioall. Sci.*, vol. 5, no. 2, pp. 148–153, 2013.
- [174] K. Dill and S. Bromberg, *Statistical Thermodynamics in Chemistry and Biology*. Garland Science, 2003.
- [175] D. Wilkins, S. Grimshaw, V. Receveur, C. Dobson, J. Jones, and L. Smith, "Hydrodynamic Radii of Native and Denatured Proteins Measured by Pulse Field Gradient NMR Techniques," *Biochemistry*, vol. 38, no. 50, pp. 16 424–16 431, 1999.
- [176] A. Oleinikova, P. Sasisanker, and H. Weingärtner, "What can Really be Learned from Dielectric Spectroscopy of Protein Solutions? A Case Study of Ribonuclease A," *J. Phys. Chem. B*, vol. 108, no. 24, pp. 8467–8474, 2004.
- [177] A. Hamill, S. Wang, and C. Lee Jr., "Probing Lysozyme Conformation with Light Reveals a New Folding Intermediate," *Biochemistry*, vol. 44, pp. 15 139–15 149, 2005.
- [178] L. Filatova, Y. Oxenoyt, K. Yakovleva, N. Ivanova, and N. Klyachko, "Investigation of the Activity and Stability of Papain in Different Micellar Systems," *Mosc. Univ. Chem. Bull.*, vol. 65, no. 2, pp. 80–86, 2010.
- [179] J. Gordon, J. Myers, T. Folta, V. Shoja, L. Heath, and A. Onufriev, "H++: A Server for Estimating pKas and Adding Missing Hydrogens to Macromolecules," *Nucleic Acids Res.*, vol. 33, no. 2, pp. W368–W371, 2005.
- [180] R. McClurg and C. Zukoski, "The Electrostatic Interaction of Rigid, Globular Proteins with Arbitrary Charge Distributions," *J. Colloid Interf. Sci.*, vol. 208, no. 2, pp. 529–542, 1998.
- [181] E. Casals, T. Pfaller, A. Duschl, G. Oostingh, and V. Puntès, "Time Evolution of the Nanoparticle Protein Corona," *ACS Nano*, vol. 4, pp. 3623–3632, 2010.
- [182] V. Uversky, "Use of Fast Protein Size-Exclusion Liquid Chromatography to Study the Unfolding of Proteins which Denature through the Molten Globule," *Biochemistry*, vol. 32, no. 48, pp. 13 288–13 298, 1993.
- [183] H. Berman, J. Westbrook, Z. Feng, G. Gilliland, T. Bhat, H. Weissig, I. Shindyalov, and P. Bourne, "The Protein Data Bank," *Nucl. Acid. Res.*, vol. 28, pp. 235–242, 2000.
- [184] J. Ferry and J. Oncley, "Studies of the Dielectric Properties of Protein Solutions. III. Lactoglobulin," *J. Am. Chem. Soc.*, vol. 63, no. 1, pp. 272–278, 1941.

- [185] E. Pezron, L. Leibler, and F. Lafuma, “Complex Formation in Polymer–Ion Solutions. 2. Polyelectrolyte Effects,” *Macromolecules*, vol. 22, no. 6, pp. 2656–2662, 1989.
- [186] J. Popot, E. Berry, D. Charvolin, C. Creuzenet, C. Ebel, D. Engelman, M. Flötenmeyer, F. Giusti, Y. Gohon, P. Hervé, Q. Hong, J. Lakey, K. Leonard, H. Shuman, P. Timmins, D. Warschawski, F. Zito, M. Zoonens, B. Pucci, and C. Tribet, “Amphipols: Polymeric Surfactants for Membrane Biology Research,” *Cell. Mol. Life Sci.*, vol. 60, no. 8, pp. 1559–1574, 2003.
- [187] F. Wiesbrock, R. Hoogenboom, M. Leenen, M. Meier, and U. Schubert, “Investigation of the Living Cationic Ring-Opening Polymerization of 2-Methyl-, 2-Ethyl-, 2-Nonyl-, and 2-Phenyl-2-oxazoline in a Single-Mode Microwave Reactor,” *Macromolecules*, vol. 38, no. 12, pp. 5025–5034, 2005.
- [188] B. Hess, C. Kutzner, D. van der Spoel, and E. Lindahl, “GROMACS 4: Algorithms for Highly Efficient, Load-Balanced, and Scalable Molecular Simulation,” *J. Chem. Theory Comput.*, vol. 4, no. 3, pp. 435–447, 2008.
- [189] U. Essmann, L. Perera, M. Berkowitz, T. Darden, H. Lee, and L. Pedersen, “A Smooth Particle Mesh Ewald Method,” *J. Chem. Phys.*, vol. 103, no. 19, pp. 8577–8593, 1995.
- [190] I. Yeh and M. Berkowitz, “Ewald Summation for Systems with Slab Geometry,” *J. Chem. Phys.*, vol. 111, no. 7, pp. 3155–3162, 1999.
- [191] B. Qiao, J. Cerdà, and C. Holm, “Atomistic Study of Surface Effects on Polyelectrolyte Adsorption: Case Study of a Poly(styrenesulfonate) Monolayer,” *Macromolecules*, vol. 44, no. 6, pp. 1707–1718, 2011.
- [192] R. Neumann, “Entropic Approach to Brownian Movement,” *Am. J. Phys.*, vol. 48, no. 5, pp. 354–357, 1980.
- [193] B. Hess, C. Holm, and N. van der Vegt, “Osmotic Coefficients of Atomistic NaCl (aq) Force Fields,” *J. Chem. Phys.*, vol. 124, no. 16, p. 164509, 2006.
- [194] I. Kalcher and J. Dzubiella, “Structure-Thermodynamics Relation of Electrolyte Solutions,” *J. Chem. Phys.*, vol. 130, no. 13, p. 134507, 2009.
- [195] R. Netz and H. Orland, “Variational Charge Renormalization in Charged Systems,” *Eur. Phys. J. E*, vol. 11, p. 301, 2003.
- [196] G. Manning, “Counterion Condensation on Charged Spheres, Cylinders, and Planes,” *J. Phys. Chem. B*, vol. 111, pp. 8554–8559, 2007.
- [197] E. Zhulina and O. Borisov, “Structure and Interaction of Weakly Charged Polyelectrolyte Brushes: Self-Consistent Field Theory,” *J. Chem. Phys.*, vol. 107, no. 15, pp. 5952–5967, 1997.

- [198] W. de Vos, F. Leermakers, A. de Keizer, J. Kleijn, and M. Stuart, “Interaction of Particles with a Polydisperse Brush: A Self-Consistent Field Analysis,” *Macromolecules*, vol. 42, no. 15, pp. 5881–5891, 2009.
- [199] I. Levental, P. Georges, and P. Janmey, “Soft Biological Materials and their Impact on Cell Function,” *Soft Matter*, vol. 3, pp. 299–306, 2007.
- [200] R. Piazza, “Interactions in Protein Solutions near Crystallisation: A Colloid Physics Approach,” *J. Cryst. Growth*, vol. 196, no. 2-4, pp. 415–423, 1999.
- [201] D. Leckband and S. Sivasankar, “Forces Controlling Protein Interactions: Theory and Experiment,” *Colloid Surface B*, vol. 14, no. 1-4, pp. 83–97, 1999.
- [202] W. Poon, S. Egelhaaf, P. Beales, A. Salonen, and L. Sawyer, “Protein Crystallization: Scaling of Charge and Salt Concentration in Lysozyme Solutions,” *J. Phys. Condens. Matter*, vol. 12, no. 35, pp. L569–L574, 2000.
- [203] G. Pellicane, D. Costa, and C. Caccamo, “Theory and Simulation of Short-Range Models of Globular Protein Solutions,” *J. Phys. Condens. Matter*, vol. 16, no. 42, p. S4923, 2004.
- [204] P. Deuffhard, *Newton Methods for Nonlinear Problems. Affine Invariance and Adaptive Algorithms*. Springer-Verlag, 2004.
- [205] W. Nolting, *Grundkurs Theoretische Physik 3: Grundkurs Theoretische Physik*. Springer, 2004.

Acknowledgments

First and foremost, I would like to thank my supervisor *Professor Joachim Dzubiella* for working on a challenging and interesting topic, for his endless guidance, encouragement, and fruitful discussions throughout the years of my graduate studies. I have truly learned a lot.

I owe a special thank to my co-supervisor *Professor Matthias Ballauff* for the experimental cooperation, discussions and his constant interest in my studies.

I am very grateful to the reviewers *Professor Jürgen P. Rabe* and *Professor Martin Schoen* as well as to *Professor Igor Sokolov* and *Professor Beate Röder* for being further members of the committee.

Many thanks to *Jan Heyda, Ph.D.*, and *Stefano Angioletti-Uberti, Ph.D.*, for their tireless support and patient answering of all my questions. Special thanks to *Dr. Nicole Welsch*, *Michael Oberle*, and *Qidi Ran* for sharing their experimental data with me and useful discussions on protein adsorption onto microgels.

I would like to thank my office colleagues *Karol Palczynski*, *Nils Heptner* and *Xiao Xu* for a joyful time during these past years and the discussions on everything imaginable. Furthermore, I thank all the other colleagues at the Institute Soft Matter and Functional Materials for a nice working environment.

I gratefully acknowledge the financial support from Helmholtz-Zentrum Berlin.

I express my sincere thanks to my best friend *Dr. Gregor Hartmann* for his unconditional support in all situations since studying physics.

I would certainly like to thank *Dorothea Okonek*, *Dr. Gregor Hartmann*, *Dr. Isabel von Bülow*, *Dr. Miriam Siebenbürger*, *Nils Heptner*, and *Karol Palczynski* for their comments and proof-reading.

My deepest gratitude goes to my family in Cologne for the endless support and encouragement it has given me all these years. *Evet anne, bana yaptığın her şey için sana burada çok büyük bir teşekkür borçluyum.*

My last words are devoted to my wife *Astrid* and to my lovely children *Laila* and *Ismail-Emin*. Without your sacrifices and patient love during all these years, this thesis would never been possible. I am eternally grateful to you.

Selbständigkeitserklärung

Hiermit versichere ich, dass ich die vorliegende Dissertation selbständig verfasst und keine anderen als die angegebenen Quellen und Hilfsmittel verwendet habe.

Ferner erkläre ich, dass ich nicht anderweitig mit oder ohne Erfolg versucht habe, eine Dissertation einzureichen oder mich einer Doktorprüfung zu unterziehen.

Berlin, den 26. März 2015

.....

Cemil Yigit

